Studying the effect of the tail on the dynamics of a flapping-wing MAV

Frank G.J. Rijks

TU Delft

Faculty of Aerospace Engineering

Studying the effect of the tail on the dynamics of a flapping-wing MAV

Master of Science Thesis

For the degree of Master of Science in Aerospace Engineering at Delft University of Technology

Frank G.J. Rijks

May 3, 2017

Faculty of Aerospace Engineering · Delft University of Technology

Delft University of Technology
Department of
Control & Simulation

The undersigned hereby certify that they have read and recommend to the Faculty of Aerospace Engineering for acceptance a thesis entitled

Studying the effect of the tail on the dynamics of a flapping-wing MAV

by

Frank G.J. Rijks

in partial fulfillment of the requirements for the degree of

Master of Science Aerospace Engineering

Dated: May 3, 2017

Supervisor(s):

Dr. Ir. C.C. de Visser

Dr. Ir. M. Karásek

Ir. S.F. Armanini

Reader(s):

Dr. Ir. Q.P. Chu

Dr. Ir. B.W. van Oudheusden

Abstract

The effects of horizontal tail geometry and position on longitudinal flapping-wing micro aerial vehicle dynamics were studied using wind tunnel and free-flight experiments. Linearised models were used to analyse the effect on the dynamic properties of the ornithopter. Results show higher steady-state velocity and increased pitch damping for increased tail surface area and aspect ratio. The maximum span width of the tail surface is also found to play an important role in determining dynamic behaviour, in particular when the distance between the tail surface and the flapping wings is large. Steady-state conditions can be predicted accurately using linear functions of tail geometry for this ornithopter. Predicting dynamic behaviour is more complicated and requires further study. However, the observed trends in some of the model parameters suggest that future models explicitly including the tail geometry may be used to design flapping-wing robots with desirable dynamic properties.

Preface

This thesis, entitled "Studying the effect of the tail on the dynamics of a flapping-wing MAV", is the final chapter in completing my Master of Science in Aerospace Engineering at TU Delft. During my internship I developed an interest in system identification and this, combined with my desire to do research with a practical component, led me towards the DelFly. This thesis has been demanding but leaves me with a satisfied feeling about what we have accomplished.

I would like to thank my supervisors, Dr.ir. C.C. de Visser, Dr.ir. M. Karásek and Ir. S.F. Armanini, for giving me the opportunity to carry out this research and for the advice along the way. I especially thank Matéj for all the help with building and testing my own DelFly. Also, a special thanks to Sophie for providing me with the state and model estimation algorithms that were absolutely essential to complete this work in a decent amount of time.

I would also like to thank Laurien and my parents for always supporting me, during my entire studies and in particular during my thesis. Laurien, thank you also for helping me find motivation to keep going, especially in the last month. Finally, thank you to everybody in the C&S upper house for the welcome distractions during working hours.

I hope you enjoy reading.

Frank Rijks

Delft, May 3, 2017

Table of Contents

Part I

Scientific Paper

Studying the Effect of the Tail on the Dynamics of a Flapping-Wing MAV using Free-Flight Data

F.G.J. Rijks[1], M. Karásek [2], S.F. Armanini [3] and C.C. de Visser [4]

Delft University of Technology, 2629HS Delft, The Netherlands.

The effects of the horizontal tail surface on the longitudinal dynamics of an ornithopter were studied by systematically varying its surface area, aspect ratio and its longitudinal position. The objective is to improve the understanding of the tail effect on the behaviour of the ornithopter and to assess if simple models based on tail geometry can predict steady-state conditions and dynamic behaviour. A data-driven approach was adopted since no suitable theoretical models for ornithopter tail aerodynamics are available. Data was obtained through wind tunnel and free-flight experiments. Fourteen tail geometries were tested, at four positions with respect to the flapping wings. Linearised models were used to study the effects of the tail on dynamic behaviour. The data shows that, within the tested ranges, increasing surface area or aspect ratio increases the steady-state velocity of the platform and improves pitch damping. Results also suggest that the maximum span width of the tail significantly influences the damping properties, especially when the distance between the tail and the flapping wings is large, which likely relates to the induced velocity profile of the flapping wings. Steady-state conditions can be predicted accurately based on tail geometry even when extrapolated slightly outside the original measurement range. Some trends were identified between model parameters and tail geometry, but more research is required before these trends can be applied as a design tool.

Nomenclature

AR	Aspect ratio $(-)$
b	Horizontal tail maximum span width (mm)
b_{LE}	Horizontal tail surface leading edge span width (mm)
c_r	Horizontal tail surface root chord (mm)
c_t	Horizontal tail surface tip chord (mm)
g	Gravitational acceleration $(g = 9.81 ms^{-2})$
I_{yy}	Body moment of inertia $(kg \cdot m^2)$
m	Mass (kg)
P	Parameter covariance matrix
p, q, r	Angular rates in body-fixed reference frame $(rad \cdot s^{-1})$
S	Surface area (cm^2)

[1] MSc Graduate Student, Department of Control & Simulation, Faculty of Aerospace Engineering, Kluyverweg 1, 2629HS Delft, The Netherlands.

[2] Postdoctoral Researcher, Department of Control & Simulation, Faculty of Aerospace Engineering, Kluyverweg 1, 2629HS Delft, The Netherlands.

[3] PhD Student, Department of Control & Simulation, Faculty of Aerospace Engineering, Kluyverweg 1, 2629HS Delft, The Netherlands, AIAA Student Member.

[4] Assistant Professor, Department of Control & Simulation, Faculty of Aerospace Engineering, Kluyverweg 1, 2629HS Delft, The Netherlands, AIAA Member.

u, v, w	Velocities in body-fixed reference frame (ms^{-1})
x_e	Longitudinal position of battery and electronics (mm)
x_h	Tail longitudinal position (mm)
X_i, Z_i, M_i	Stability and control derivatives in standard notation
Δ	Perturbation from steady-state
δ_e	Elevator deflection (deg)
δ_f	Flapping frequency (Hz)
$\hat{\theta}$	Estimated parameter vector
ϕ, θ, ψ	Euler angles (deg)
σ	Standard deviation

I. Introduction

Researchers have been inspired by flying insects and vertebrates for many years due to their enormous aerodynamic capabilities. Their manoeuvrability and flexibility in flight envelope are unparalleled. Insects can quickly transition from hover to fast forward flight and even fly backwards [1]. Flapping-wing flight is a very active field of research and studies involving robotic insect wings have yielded particularly valuable insights into the highly nonlinear and unsteady aerodynamics involved with flapping-wing flight [2–6]. Recent years have seen a significant increase in research into robotic flapping-wing micro aerial vehicles (FWMAVs) in an attempt to exploit the advantages of flapping wings [7–15]. However, due to a still limited understanding of flapping-wing aerodynamics these man-made ornithopters currently cannot match the performance encountered in nature. There is a particular need for simple, yet more complete, dynamic models to design control algorithms and to predict flight performance across a wide range of flight conditions.

Most robotic flappers feature a tail surface for passive stability and to provide easier control through conventional aerodynamic surfaces [16]. This comes at the cost of increased size, higher gust sensitivity and reduced manoeuvrability. For these reasons active wing control, which is needed to achieve tailless FWMAV designs, is a particularly active research field today [10, 11, 17]. However, a tail surface can be beneficial in particular mission scenarios. During fast forward flight, for example, exploiting passive stability may prove to be more energy-efficient than active wing control. Some birds also manipulate their tail geometry for flight control, a feat which may be interesting for future FWMAVs [18]. Even though a tail surface has many potential advantages, the effects of a tail surface on dynamic behaviour have not been studied thoroughly [3, 19]. Numerical methods struggle to capture the complexity of the unsteady, time-varying aerodynamics and its interaction with a tail surface [20]. Theoretical models developed to estimate the aerodynamics of birds' tails have been found to be inaccurate when compared to experimental measurements [18, 21]. Most FWMAV models do not explicitly account for the tail surface [12, 13]. Those models explicitly accounting for the tail are platform-specific and omit the interaction with the flapping wings [8]. A potentially accurate tail aerodynamic model was developed in a recent study, based on the time-varying wake of the flapping wings which was measured using particle image velocimetry (PIV) data, but the resulting aerodynamic tail model remains to be validated [22]. Improving the understanding of the effect of a tail surface and its interaction with the flapping-wing wake could lead to more complete FWMAV models and should benefit the development of robotic ornithopters with improved performance.

System identification is an attractive approach to study the effect of the tail because of the highly complex, nonlinear aerodynamics involved with flapping flight and the current lack of suitable theoretical models of tail aerodynamics. Data can be obtained either from wind tunnel measurements or through free-flight. Free-flight data is the most ideal since the data is acquired in the most realistic setting. Recent developments in on-board data acquisition, in combination with optical tracking data, have opened the door for obtaining high quality data suitable for system identification from free-flight [13, 23–26].

This paper presents the results of a systematic study into the effect of the horizontal tail surface on the flight dynamics of an ornithopter, the DelFly II ([19]), using free-flight and wind tunnel

experiments. Specifically, this study focuses on longitudinal, time-averaged dynamics and stability characteristics. The aim is to apply simple, physically meaningful models to achieve new insights into the influence of the tail. The complete design space of tail geometries is vast. Therefore the scope is limited to three parameters: surface area, aspect ratio and longitudinal position. A modified version of the DelFly II is designed, featuring a modular tail which can be detached in its entirety from the body and which facilitates easy adjustment of the horizontal tail surface and the longitudinal position of the tail.

Wind tunnel experiments were used to obtain measurements both with and without tail surface, attempting estimate the contribution of the tail surface to the total forces and moments. Measurements were also performed in several flight conditions surrounding the steady-state resulting in estimations of stability derivatives with respect to free-stream velocity. Free-flight system identification experiments were conducted using pre-programmed elevator doublet manoeuvres. The free-flight data was used to estimate longitudinal, decoupled linear time-invariant (LTI) models. This model structure is relatively simple and has proven to be effective in predicting time-averaged dynamics of ornithopters [12, 27]. An analysis of the LTI model eigenvalues and parameters was performed to gain insight into the effect of the horizontal tail on the dynamics of an ornithopter. The feasibility of using trends found in the models to predict dynamic properties when using other tail configurations was assessed as well.

The structure of this paper is as follows. Section II discusses the experimental approach taken in this study, including a detailed description of the test platform and a discussion on experiment execution and data processing. This is followed by a discussion of the modelling approach in Section III, presenting the model structure, the methods of parameter estimation and the model validation approach. Results of the experiments are presented and discussed in Section IV. Finally, Section V summarises the most important findings and offers recommendations for future work.

II. Experimental set-up

A. Test platform

The DelFly II is a four-winged flapping-wing micro aerial vehicle (FWMAV) developed at Delft University of Technology, see Figure 1. Development of this FWMAV started in 2005 and one of its main purposes is to study the aerodynamics of flapping wings through experimental methods. The DelFly II is also used extensively for research into autonomous flight capabilities of small MAVs [7]. The wings are arranged in an X-configuration and have a total span width of $280mm$. For a more complete description of the DelFly II, please refer to de Croon et al. [19].

The DelFly II comes in many forms with varying on-board equipment. The platform used in this study is equipped with a Lisa/S autopilot containing an Inertial Measurement Unit (IMU) for data acquisition. The platform is equipped with active LED markers, indicated by red circles in Figure 1(b), for optical tracking purposes. The ornithopter used in this study ranges in mass from $22.8 - 24.3g$, depending on the test configuration.

Some changes were made to the standard design to facilitate an efficient study of the effect of tail geometry. Most importantly, the tail has been redesigned as a modular part of the system which can be detached from the fuselage in its entirety. This allows intermediate fuselage segments to be added or removed to control the longitudinal position of the tail.

The horizontal tail surface consists of a so-called base tail onto which tail geometries of desired size and shape can be attached. This is illustrated in Figure 1. The base tail and elevator surface can be seen in Figure 1(a), the standard tail has been attached to the base tail in Figure 1(b). Due to this design the platform features a smaller elevator surface than the standard DelFly II. This proved to be no problem in terms of excitation during free-flight experiments.

Since the test geometries should fit around the horizontal base piece the minimum size of the tail geometries is constrained by the size of the horizontal base tail. Through flight experience it was found that the base tail alone is too small for stable flight, thus this limitation has little influence on the final results. The base tail and elevator have a total chord length of $48mm$ and a span width of $80mm$, see Figure 2. This was found to provide suitable support for the vertical tail whilst limiting constraints imposed on the horizontal tail designs.

The fuselage is split into a front section and a tail section. A middle segment can be added to adjust the longitudinal position of the tail. Fuselage segments are connected using a guiding pin

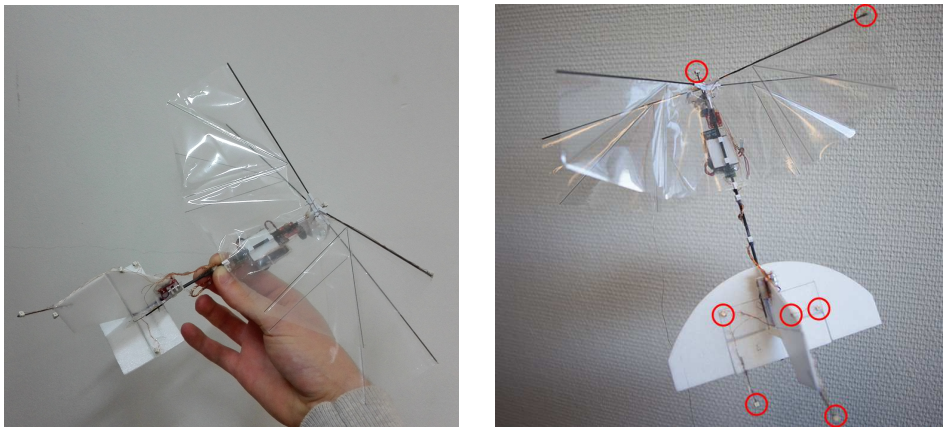

(a) Base tail only. (b) With standard tail.

Fig. 1 Pictures of the FWMAV used in this study, illustrating the modular tail concept.

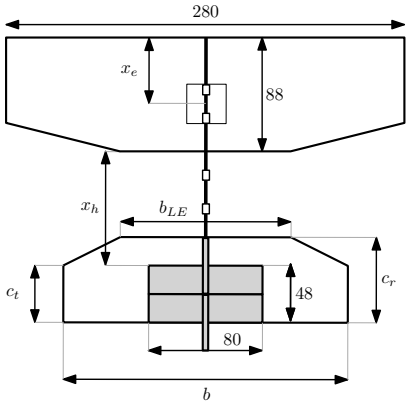

Fig. 2 Geometrical parameters to manipulate tail geometry and position. Figure not to scale.

which slides inside the hollow cross-section of the fuselage, while a bracket prevents the segments from rotating with respect to each other.

B. Test configurations

The number of conceivable tail geometries is enormous. To limit the scope of the study the focus will be on three parameters.

The force generated by an aerodynamic surface scales with its total surface area. In steady aerodynamics this relationship is linear [28]. It is interesting to see if this is also valid for an aerodynamic surface in the wake of flapping wings. Therefore the surface area (S) of the horizontal stabiliser shall be studied.

The second variable is tail aspect ratio (AR). This parameter provides a measure of the aerodynamic efficiency of a wing, for example, in steady aerodynamics. The aspect ratio is defined by Equation (1) [28].

$$AR = \frac{b^2}{S} \tag{1}$$

Finally, it is clear from previous studies that the interaction between flapping wings and tail surface is very complex [18, 20]. PIV experiments show that the wake structure of the DelFly is highly nonlinear and unsteady. Its strength and direction vary with span- and chord-wise position behind the flapping wings [29]. This affects the magnitude of the induced velocity and thus the

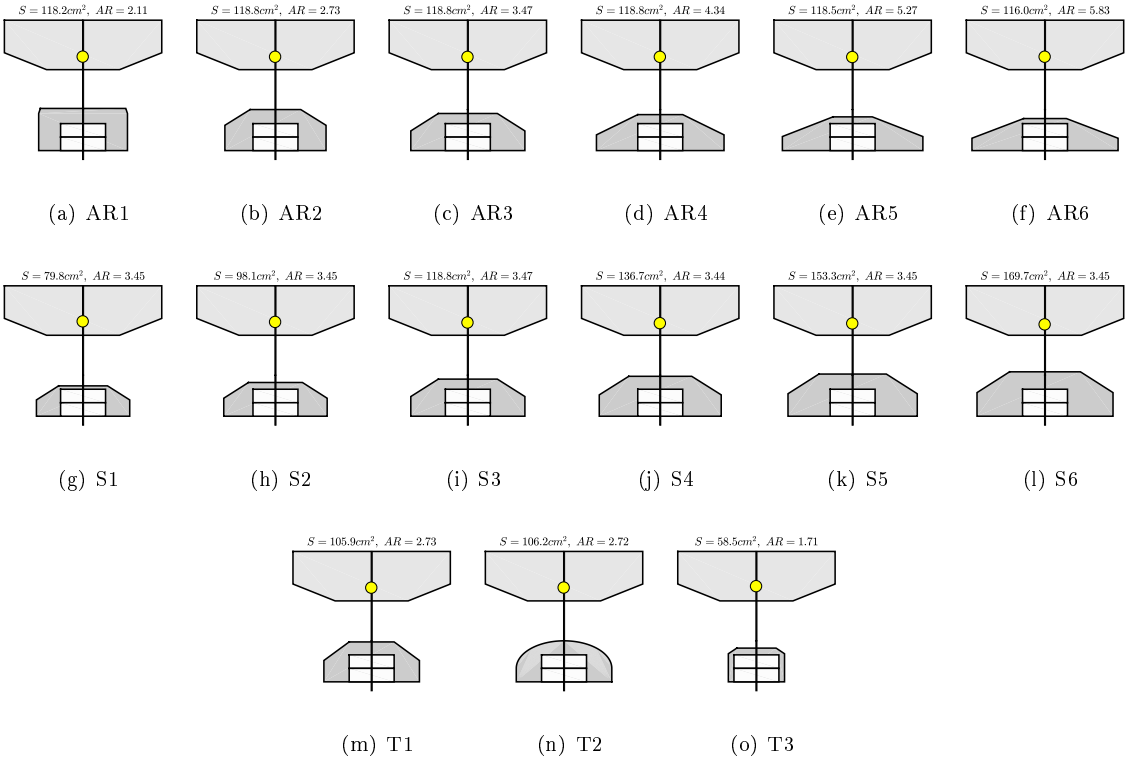

(a) AR1 (b) AR2 (c) AR3 (d) AR4 (e) AR5 (f) AR6

(g) S1 (h) S2 (i) S3 (j) S4 (k) S5 (l) S6

(m) T1 (n) T2 (o) T3

Fig. 3 Tail geometries used in this study. Dot represents the estimated CG position.

Table 1 Fuselage configurations used in the experiments.

Fuselage identifier	a	b	c	d
$x_h(mm)$	57	98	126	114

flow conditions at the tail surface [22]. This warrants an investigation into the effect of longitudinal position on the dynamic behaviour of the FWMAV.

The aforementioned variables are varied systematically to study their effect on the system dynamics. To study surface area and aspect ratio each variable is manipulated whilst keeping the other constant. Figure 2 shows the physical parameters to be manipulated to control the AR, surface area and longitudinal position of the tail surface. x_e denotes the position of the electronics assembly containing the battery and the Lisa/S autopilot. This assembly can slide along the fuselage to provide additional control over the longitudinal position of the centre of gravity (CG).

Figure 3 shows schematics of the tail geometries used in this study. Note that AR3 and S3 in fact share the same geometry, fitting in both test series. The exact physical dimensions are provided in Table A.1, in the appendix. The tail configurations used to test the effect of surface area have a fixed aspect ratio $AR \approx 3.45$, which was found to provide a good range in surface areas that could be covered given the limitations imposed by the base tail. S6 has slightly more than twice the surface area of S1, see Figure 3(g)-3(l). The aspect ratio tails all have a surface area $S \approx 118.2cm^2$. Again this provided the possibility of testing a large range in aspect ratios whilst maintaining the same surface area. The tested aspect ratios range from 2.11 (AR1) to 5.83 (AR6), see Figure 3(a)-3(f).

Figure 3(m), Figure 3(n) and Figure 3(o) show three additional tail surfaces that were tested. T2, in Figure 3(n), is the standard tail surface used for this FWMAV. T1 has practically the same aspect ratio and surface area and was used to assess the effect of changing the leading edge shape to non-elliptical. Within the accuracy of the experimental methods used in this study the response of these two tail configurations was found to be almost identical. Finally, T3 (Figure 3(o)) was used to assess at which point the ornithopter started to show unstable behaviour.

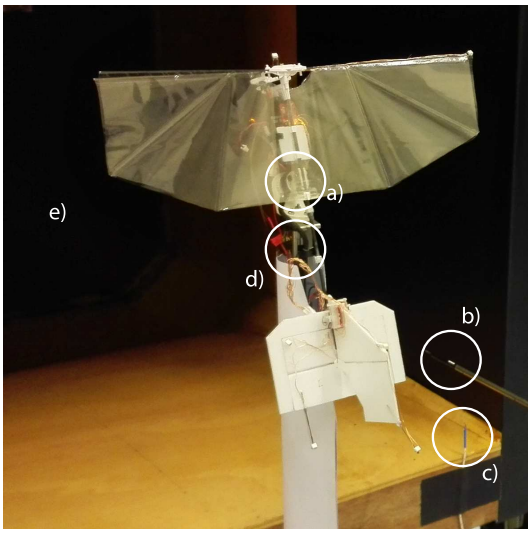

Fig. 4 Picture of the DelFly in the wind tunnel. a) ATI Nano-17 force transducer; b) hot-wire anemometer; c) thermocouple; d) actuated strut; e) open section wind tunnel

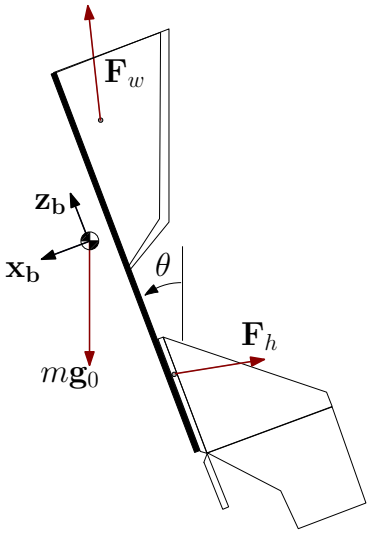

Fig. 5 Free-body diagram of the DelFly in slow forward flight, showing the body-fixed reference frame. $\mathbf{y}_b$ is positive towards the left-hand wing.

A total of four different longitudinal tail positions were tested. Table 1 gives an overview of the fuselage lengths that were used and the corresponding tail positions x_h, defined as the distance from the flapping-wing trailing edge to the leading edge of the base tail, see Figure 2. Throughout the remainder of this paper configurations are denoted by a tail and fuselage identifier, e.g., configuration S3c represents tail S3 at a longitudinal position $x_h = 126mm$.

C. Wind tunnel experiments

Wind tunnel experiments can be used to obtain accurate, high frequency force and moment measurements under pre-defined and well-known conditions. The main reason to conduct wind tunnel experiments is the opportunity to remove the tail without having issues with instability and thereby measure the contribution of the tail to the total forces and moments, i.e., to estimate F_h in Figure 5, by subtracting F_w from the total. Note that the forces in Figure 5 are not to scale. The depicted direction of F_h is loosely based on results by Armanini et al. [22].

Wind tunnel experiments were conducted in the W-tunnel at the TU Delft Faculty of Aerospace Engineering. The W-tunnel is a relatively small wind tunnel designed for low speeds and low turbulence ($\approx 1\%$). For the experiments a $0.6 \times 0.6m$ test section was used. This is large enough to avoid boundary layer effects caused by the walls of the test section to influence the measurements [30]. Figure 4 shows a picture of the ornithopter in the test set-up.

A drawback of wind tunnel experiments is the fact that the MAV is clamped to the force balance, see Figure 4. This has an effect especially on the body x_b force (see Figure 5) due to the absence of oscillations in the pitch attitude which cause aerodynamic damping effects during free-flight [31].

Forces and moments were measured using an *ATI Nano-17* force transducer which measures forces and moments in 6 degrees of freedom (DOF) with a 0.149gram-force resolution. Data is logged with a frequency of $10kHz$ over a duration of two seconds. This corresponds to $24 - 26$ flapping cycles. Flapping cycles are distinguished by use of a Hall-sensor and a magnet attached to the flapping mechanism. This provides the measurement of flapping frequency. The motor RPM is also logged. This can be translated to flapping frequency through the gear ratio ($= 21.33$), providing a redundant measurement. A calibration table is provided at the W-tunnel, correlating wind tunnel RPM to free-stream velocity. In addition, velocity was measured using a hot-wire anemometer. This provides a redundant measurement and the hot-wire system can also detect variations in velocity at high frequency. The pitch angle of the ornithopter was set using an actuated mechanism inside the strut, see Figure 4, and is assumed fixed during a measurement.

For each configuration measurements were performed in the steady state both with tail attached and without the tail. The purpose of these measurements was to obtain an estimate of the contribution of the tail surface to the total forces and moments. Since the steady-state conditions in fact fluctuate during free-flight, the test conditions were also varied, independently, about the steady-state. The pitch angle was varied with $\theta_0 \pm 5$ degrees, the velocity with $V_0 \pm \approx 0.25 m/s$ and the flapping frequency with $\delta_{f,0} \pm \approx 1.4 Hz$. These measurements were performed with the tail attached and allowed estimates of stability derivatives with free-stream velocity, see Section IV B. The steady-state conditions for each configuration were obtained from free-flight prior to the wind tunnel experiments.

D. Free-flight experiments

As mentioned, wind tunnel experiments have some limitations and cannot be used to assess dynamic stability characteristics of a particular configuration [31, 32]. Free-flight experiments are therefore required to thoroughly study the effect of the tail. Only very recently has it become possible to obtain data suitable for system identification from free-flight [12, 25, 27].

Free-flight experiments were conducted in the *CyberZoo* at the Faculty of Aerospace Engineering. The *CyberZoo* is equipped with an optical motion tracking system (henceforth, OptiTrack) consisting of 24 infrared OptiTrack Flex13 cameras. The OptiTrack system tracks the position of active or passive markers within a $10 \times 10 \times 7m$ volume at 120 frames per second. Marker locations on the ornithoper are indicated by the red circles in Figure 1(b). The markers are positioned to give an estimate of the body attitude, the wing angle and control surface deflections [25].

1. Flight test execution

During free-flight experiments the FWMAV was flown manually, though the system identification manoeuvres were pre-programmed and performed automatically. This ensured consistent excitation of the longitudinal dynamics and increased the likelihood of repeatable results. The operator could trigger a manoeuvre using a switch on the transmitter.

The dynamics were excited using doublet pulses on the elevator, which was found to provide the most suitable excitation. The main reason to choose a doublet manoeuvre is its symmetry, which makes it more likely that the ornithopter remains close to its steady-state. This allows the application of linearised models (see Section III). Due to the limited size of the *CyberZoo* it is also an advantage to use the relatively short doublet manoeuvres instead of, for example, 3211 sequences [13].

Through flight testing with the more extreme tail geometries it was found that a 65% elevator deflection with 0.33 second pulses provides sufficient excitation for larger tail geometries whilst not destabilising most of the smaller ones. Experiments for configuration T3 were performed with a 30% deflection doublet since this was the only configuration that was destabilised by larger inputs. For each configuration a single flight was performed with an average flight time of approximately 5-6 minutes, resulting in an average of 21 manoeuvres per flight. It is assumed that each manoeuvre can be treated as an independent experiment.

Before conducting free-flight experiments a calibration between the OptiTrack attitude and the on-board IMU is performed to cope with possible misalignments of the IMU with respect to the body-fixed reference frame [25]. Then an OptiTrack recording and on-board logging can be started. An experiment consists of three steps: (1) trimming the FWMAV to achieve approximately steady, level flight; (2) initiating a manoeuvre; (3) allowing the response to dampen out, during which time no stick input should be given. After some time the ornithopter must be turned to stay inside the tracking volume and the steps are repeated. It is important that sufficient time is allowed for the response to damp out since this provides the most accurate data on the system dynamics.

After each flight the on-board log was downloaded whilst the battery was charging. During the experiments the electronics assembly and battery were fixed in position to minimise the changes made to the ornithopter. Thus, $x_e \approx 52mm$ for all system identification experiments.

For part of the configurations flights were performed with throttle doublet inputs. The input was varied to $\pm 13\%$ of the throttle value at initialisation of the manoeuvre. Pulse duration and experiment execution were the same as for the other system identification experiments. Ultimately

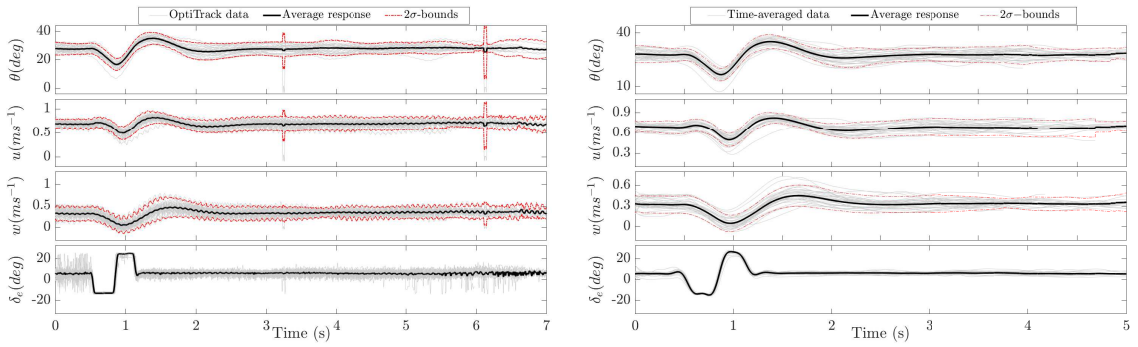

(a) Raw OptiTrack data.

(b) Processed and filtered data.

Fig. 6 Example of raw and processed data for configuration S5b. Overlay of all 23 manoeuvres performed during the flight.

the throttle input provided less efficient excitation of the dynamics. Elevator doublets are a better choice of input since the direct disturbance of the pitching moment gives the most relevant excitation for a study of the tail effect.

2. Data processing

Some processing is required before the data from free-flight experiments can be used for model estimation. This section will briefly discuss the most important elements of data processing. For a more complete description refer to Armanini et al. [26] or Karásek et al. [25].

Data needs to be synchronised in the time-domain since the OptiTrack recording and the on-board IMU data are two individual data-sets. LED markers on the vertical tail and on the rudder, see Figure 1(b), only turn on when on-board data is being logged. This allows the beginning and ending of an on-board log to be observed in the optical tracking data [25]. The OptiTrack data is then interpolated using spline interpolation, from $120Hz$ to $512Hz$, to match the IMU data rate. Euler angles and body-fixed velocities are then estimated using an extended Kalman filter (EKF). The EKF fuses the high frequency data of the IMU and the lower frequency OptiTrack data, which is less prone to drift. For a full description of the Kalman filter see Armanini et al. [26].

Due to the placement of the markers, tracking quality of the elevator angle was sometimes poor. To cope with this, unrealistic elevator angles ($\text{abs}\,(\Delta\delta_e) \geq 25deg$) were removed from the OptiTrack data and the resulting missing values replaced by interpolating between the remaining data points.

Manoeuvres were then automatically isolated using the elevator servo command signal which is logged on-board. A data segment is started 0.5 seconds prior to the beginning of a manoeuvre, to have some run-in time, and lasts until a rudder deflection (i.e., a turn) is detected. The detected manoeuvres were all checked manually to see if the algorithm worked correctly and manually terminated early in case of OptiTrack tracking problems. These sometimes occur when the ornithopter is flown near the edges of the tracking volume.

Finally, the data is filtered using a fourth order low-pass Butterworth filter. The cut-off frequency is chosen at $5Hz$. This was found to be a suitable cut-off frequency to separate the time-averaged signal content from the flapping-related data in previous system identification work performed for this particular ornithopter [27]. Filtering at this cut-off frequency does however cause some rounding of the elevator input data, which may have an effect on the estimated control effectiveness parameters.

An example of the data obtained from free-flight is given in Figure 6. The raw OptiTrack data is shown in Figure 6(a), perfectly illustrating the drastic effect of a tracking problem, showing large spikes in the 2σ bounds. Figure 6(b) shows the same data after processing and filtering. This data is ready to be used for model identification.

III. Modelling

A. Model structure

The model structure used in this study is given in Equation (2). It is a decoupled, longitudinal LTI model. Previous work has shown that the time-averaged dynamics, in a limited domain around steady flight conditions, can be approximated well using LTI models even though flapping-wing MAVs are highly non-linear in nature [12, 13, 33]. This approach is considered valid for ornithopters which have a high enough flapping frequency such that time-scale separation applies [27]. Figure 5 specifies the body-fixed reference frame, which is different from the aerospace convention. Armanini et al. switched to a different reference frame definition in previous work to avoid singularity problems due to the typically large pitch angles assumed by this ornithopter [26].

$$\begin{bmatrix} \Delta\dot{q} \\ \Delta\dot{u} \\ \Delta\dot{w} \\ \Delta\dot{\theta} \end{bmatrix} = \begin{bmatrix} \frac{M_q}{I_{yy}} & \frac{M_u}{I_{yy}} & \frac{M_w}{I_{yy}} & 0 \\ \frac{X_q}{m} - w_0 & \frac{X_u}{m} & \frac{X_w}{m} & -g\cos\theta_0 \\ \frac{Z_q}{m} + u_0 & \frac{Z_u}{m} & \frac{Z_w}{m} & -g\sin\theta_0 \\ 1 & 0 & 0 & 0 \end{bmatrix} \begin{bmatrix} \Delta q \\ \Delta u \\ \Delta w \\ \Delta\theta \end{bmatrix} + \begin{bmatrix} \frac{M_{\delta_e}}{I_{yy}} \\ \frac{X_{\delta_e}}{m} \\ \frac{Z_{\delta_e}}{m} \\ 0 \end{bmatrix} \begin{bmatrix} \Delta\delta_e \end{bmatrix} \tag{2}$$

Initially, flapping frequency, $\Delta\delta_f$, was considered as a second input to the model. However, this did not yield any significant improvement in model accuracy and provided little additional insight into the effect of the tail because responses to throttle input varied only very little between configurations. Also, as discussed before, elevator manoeuvres were found to provide more suitable excitation to study the effect of the tail since it is a direct pitching moment disturbance. For simplicity, flapping frequency was omitted in the final model structure.

The advantage of using the LTI model structure is its simplicity as opposed to, for example, quasi-steady models [4, 34]. LTI models are easier to use for obtaining new insights into the effect of the tail. The model structure is partly physical in nature, i.e., changes in parameter values can be linked to physical changes of the system, but is still relatively easy to interpret.

A drawback of LTI models is their limited validity about a steady-state condition. Moving away from this steady state makes the model less accurate and eventually unusable. It should be kept in mind that the assumption of linearity may be violated during real flight. The LTI model also contains no explicit terms modelling the tail geometry. Thus, it will not always be trivial that changes in parameters are a result of a change in tail geometry. However, for an initial study of the tail effect on the dynamics the LTI model structure is expected to be sufficient.

B. Parameter estimation

Parameters of the LTI model were estimated using a combination of ordinary least squares (OLS) estimation and a maximum likelihood (ML) optimisation step. The OLS estimation is a linear regression problem which always converges to the global optimum but rests on the assumption of error-free regressor measurements. ML estimation on the other hand allows for noise in the measurements but is a nonlinear optimisation problem which is prone to divergence or convergence to local optima. In previous work a combination of these estimation techniques proved to be successful [33]. For a more detailed outline of the parameter estimation approach, see Armanini et al. [27].

Parameters are first estimated using the OLS approach. These estimated parameters are subsequently used as the initial guess for the ML optimisation step. According to a comparison by Armanini et al. the ML optimisation leads to more accurate results if successful, though there is always a risk of divergence [33].

This approach was found to give satisfactory results. Models were estimated for each experiment in a data set, e.g., for each manoeuvre instance, and ML divergence typically occurred for less than two data sets per configuration.

C. Obtaining average models

To compare the dynamic behaviour of the tail geometries it is more convenient to estimate a single, representative model for each configuration. Three approaches to estimate such an average model were attempted.

1. Mean parameter model

The most straightforward approach to estimate an average model for a configuration is to simply take the mean of the parameters estimated in individual models. Since the input used to excite the dynamics is pre-programmed, the excitation of the system is very consistent (see the overlay in Figure 6). This leads to a similar response for each excitation and thus should yield consistent models. Analysing the mean of the model parameters is considered a reasonable first step in determining a representative model. Of course, small disturbances experienced in-flight will lead to variation in the models. The standard deviation of the parameters over the individual models is thus a good measure of the reliability of a certain parameter. The mean and standard deviations of the parameters can also give an indication of the relative importance of that particular parameter on the system dynamics.

2. Weighted mean (WM) model

Taking a simple mean of all the parameters may not be the most accurate method to estimate a representative model, since it assumes that all parameter estimates were equally successful. Due to the nature of the ML optimisation step in the parameter estimation process, this is not necessarily true. Ljung proposes a method which computes a weighted mean (WM) of the parameters by taking into account the covariance matrix of the estimation [35].

Given multiple parameter estimates, obtained from independent sets of data, Equation (3) provides an average parameter set weighted according to the estimated covariance matrices. $\hat{\theta}^i$ represents the parameter estimate for data set i.

$$\hat{\theta} = P \cdot \sum_{i=1}^{n} \left(\left[P^{(i)} \right]^{-1} \cdot \hat{\theta}^i \right), \text{ with } P = \left[\sum_{i=1}^{n} \left[P^{(i)} \right]^{-1} \right]^{-1} \tag{3}$$

This method takes into account that not all estimations are equally good. According to Ljung, the parameter estimate resulting from Equation (3) should be the minimum covariance parameter estimate [35].

3. Averaged time-response (TA) model

Finally, an average model is computed by overlaying the data sets which are to be used for estimation and computing the mean response. A model can then be estimated based on this average response. This approach is assumed valid since the flapping-related content of the data is not taken into account. From Figure 6, the response to the input is very consistent. This is also in line with previous system identification work for the DelFly [13].

Due to the high consistency of the individual manoeuvres performed during an experiment it is considered justified to estimate a model based on the average response as a representative model. Throughout this paper this model shall be indicated as the time-averaged (TA) model.

D. Model validation

1. Approach

Model validation is performed on two levels. First the quality of each individual model is assessed by simulating its response to the measured input. Comparing the model-predicted states to the measured states gives a measure of accuracy for the particular model. Then, the aforementioned averaged models are estimated, using a selection of the accepted data sets, and tested against validation data which was not used to estimate the averaged models.

Three metrics were used to evaluate the quality of individual models: (1) the root mean squared (RMS) error between measured and model-predicted states; (2) the Pearson's correlation coefficient (PCC), see Equation (4), where $\hat{y}$ represents an arbitrary model output state and y_m the respective measured state. The PCC varies from 0 (no correlation) to 1 (full correlation); and (3) the covariance of the parameter estimates.

Table 2 Model validation metrics.

Metric	Threshold
RMS	$RMS \geq 80$ %tile
PCC	$\text{mean}(PCC) \leq 0.70$
Covariance	$\lvert\frac{\text{cov}(\hat{\theta})}{\hat{\theta}}\rvert > 1$

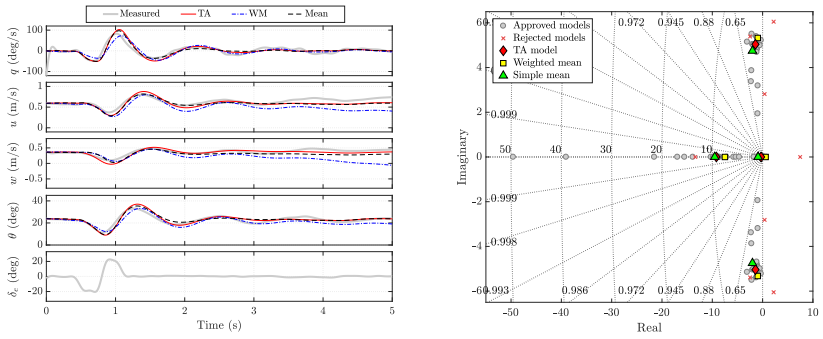

(a) Time response (b) Eigenvalues

Fig. 7 Example of validation results for configuration S1b

$$PCC = \frac{\text{cov}\left(\hat{y}, y_m\right)}{\sigma_{\hat{y}} \cdot \sigma_{y_m}} \tag{4}$$

Suitable thresholds for each validation metric were determined experimentally. The resulting values are given in Table 2. For each model, these metrics are evaluated and each state or parameter exceeding a threshold is flagged. To check if the RMS value of a particular output state is too high it is compared to the RMS values of all individual models. The highest 20% of the RMS values are flagged. The RMS flags are divided by the number of output states (4). The covariance flags are normalised by the total number of parameters. This results in a summed flag value for each model. If the flag value of a model exceeds 1, it is rejected and will not be used to estimate average models for the configuration.

After evaluating the individual models based on the criteria in Table 2, a random selection is made from the accepted models. 70% of the data is selected for identification of averaged models, whilst the remaining 30% of the data is kept for validation.

The averaged models are tested on the remaining validation data to find the most representative one. To evaluate the averaged models, two metrics are used: the mean RMS and the mean PCC values. These results are summed over the total number of validation data sets. The model scoring best on the highest number of data sets is considered to be the most representative model for that particular configuration. The highest fitness models are then used to compare the dynamic characteristics of different tail geometries.

2. Results

Models for all configurations were validated using the aforementioned approach. Figure 7 shows an example of the results for configuration S1b. These results are representative for the bulk of the configurations. In the appendix, Table A.2 gives an overview of the validation results for all configurations.

Figure 7(a) shows the model-predicted time responses versus the measured states for a single validation data set. It is observed that all three models predict the measured states with a reasonable accuracy. There is however a slight instability in the weighted mean (WM) model, caused by a positive real eigenvalue.

Figure 7(b) shows the system eigenvalues on a pole plot. A good clustering of the eigenvalues can be observed, particularly in the complex conjugate eigenvalues. The averaged models show high consistency in the complex conjugate pair of eigenvalues, which are also located around the cluster of the individual models. This gives a measure of confidence into the methods used to obtain the average models. The real eigenvalues are less consistent and show more spread. This was also the case in previous system identification work for this ornithopter and is most likely caused by a lack of excitation in the body z_b-axis [13].

Figure 7(b) also shows the poles of rejected models, which were not used for estimation or validation of the averaged models. In this case the rejected models with unstable complex conjugate pole pairs are a result of ML optimisation divergence. In most cases model rejection was a result of the ML optimisation converging to a local minimum, yielding sub optimal results. Typically less than four individual models are rejected, leaving an average of 12 independent data sets to estimate average models, suggesting that the experiment execution and the estimation process were generally successful.

The three averaged models all perform quite well for the given example. The weighted mean model, however, has a tendency to be drawn towards unstable real poles if these are present in any of the models used to estimate the WM model. Apparently the model parameters of models with an unstable real pole have a very low covariance giving them a high weighting in the computation of the WM model. As a result the WM model shows a slight instability, visible in the time response in Figure 7(a).

Table A.2 shows the validation metrics for configuration S1b. For this configuration, all three average models perform quite well, with a mean $PCC > 0.80$, and mean $RMS = 0.11$ for the TA and mean model. However, the slight instability in the WM model clearly results in higher RMS (0.16) and lower PCC (0.64) values. The TA model scores best and is therefore the most representative model for configuration S1b.

For some configurations the weighted mean model is drawn quite far towards an unstable pole due to more than one model with a positive real eigenvalue in the estimation data. In some cases this leads to poor validation results for the weighted mean model, see Table A.2 for an overview. The simple mean model and the TA model are much less sensitive to models which feature a positive real eigenvalue.

Overall the TA model scored best for a majority of the configurations that were tested. This confirms the consistency of the dynamic excitation and provides additional confidence into proper experiment execution.

IV. Results & discussion

A. Wind tunnel

Figure 8 shows results of the force balance measurements performed in the wind tunnel, in steady-state conditions, as a function of tail geometry. Error bars indicate two times the standard deviation of the forces and moments over a total of 24-26 flapping cycles per measurement. Each steady-state measurement was repeated three times.

It was not possible to identify clear trends consistent with a variable tail geometry from the results in Figure 8 or from force balance results for other longitudinal positions x_h. This made it very difficult to accurately estimate the tail contribution, i.e., F_h in Figure 5, as a function of tail geometry.

This is most likely caused by a combination of the test-setup and the resolution of the sensor that was used. Apparently the force and moment differences are so small that even this high resolution (0.149g-force) sensor has trouble to accurately measure the differences between tails. However, on the small scales involved with this ornithopter these small differences still make a significant difference in dynamic behaviour, as was observed during free-flight (see Section IV B). Furthermore, it is expected that the force balance strut affects the airflow upstream of the tail surface to some extent and thereby influences the measurements. An attempt was made to streamline the strut, see Figure 4, but this is still a drawback and, more importantly, an unknown factor in the measurement.

The difference between tailed and tailless measurements shows opposite trends in Figure 8(a) and Figure 8(b). This also suggests an influence of the force balance strut. With varying x_h the distance between the strut and the tail surface changes which may result in different influences of

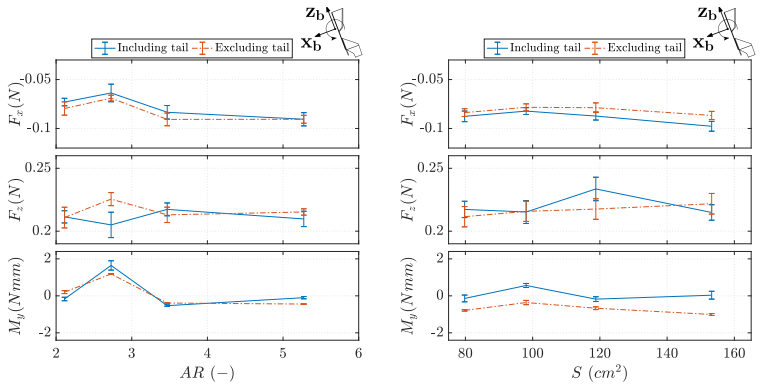

(a) With aspect ratio, $x_h = 98mm$. (b) With surface area, $x_h = 126mm$.

Fig. 8 Wind tunnel results as function of tail geometry. 2σ error-bars.

the strut on the final results. However, the opposite trend may also be caused by a change in tail effectiveness at increased longitudinal distance from the flapping wings. It is currently not possible to differentiate between these two causes since the effect of the strut is unknown.

Previous studies, comparing wind tunnel measurements to free-flight data, pointed out that the force measured in the body x_b-axis is especially influenced by clamping effects [24]. An aerodynamic tail model developed by Armanini et al., using PIV data to model the tail-wake interactions for the DelFly in hover conditions, suggests that the tail is actually generating force almost exclusively in x_b direction, in the range of $0.01 - 0.03N$ [22], which corresponds to the order of magnitude of the results in Figure 8. With the total contribution of the tail in this range it is not unlikely that differences between tail geometries are much smaller and are too small to be measured reliably with the sensor that was available. It can thus be concluded that a change in wind tunnel setup or a more sensitive force balance would be required to accurately estimate the force generated by the tail.

However, it was possible to obtain some estimates of stability derivatives from the wind tunnel results. Figure 18 in Section IV B shows results for X_u, both from the models estimated from free-flight data and derivatives estimated from wind tunnel data. X_u could be estimated from measurements that were performed for free-stream velocities fluctuating about the steady-state ($V_0 \pm \approx 0.25ms^{-1}$). The estimates from wind tunnel data and free-flight are in the same order of magnitude, though the actual values are different. Nevertheless, this provides some measure of confidence in estimates derived both from wind tunnel data and free-flight. More importantly it shows that simple stability derivatives may actually be derived from wind tunnel experiments. However, it also calls for some additional study with regard to the accuracy of both experimental methods.

Figure 18 shows that aspect ratio seems to have no significant effect on X_u. However, a minimal trend is observed with surface area in Figure 18(b), showing a slight increase in magnitude for X_u when the tail surface area is increased. This is as expected, since X_u can be interpreted as the drag force as a function of forward velocity, which is usually influenced by the surface area of the translating body.

B. Free-flight

1. Effect on steady-state

Despite no significant trends to be observed in the wind tunnel results, the tail geometry is still expected to affect the magnitude of the tail force F_h. Assuming that the force generated by the flapping wings (F_w) initially remains unchanged, this would result in a different moment equilibrium and therefore different steady-state conditions, see Figure 5. The effect of the horizontal tail aspect ratio on the steady-state conditions is shown in Figure 9. Linear fits were estimated using three of the configurations, leaving one configuration to validate if steady-state conditions may be predicted based on tail geometry.

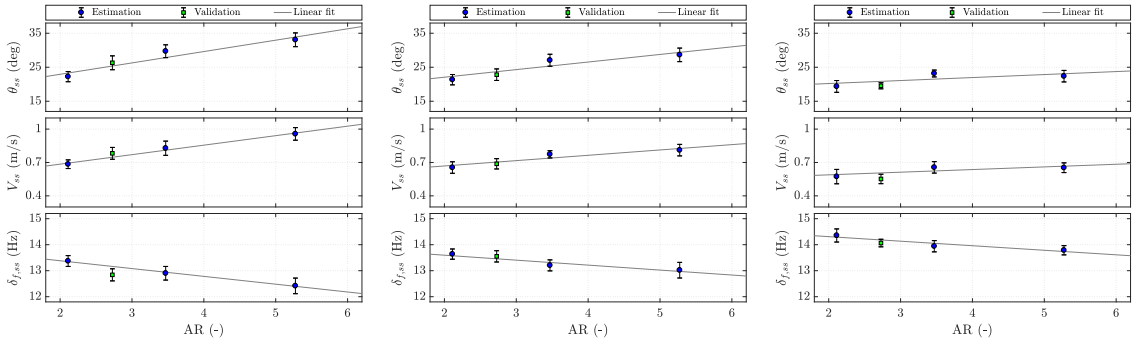

(a) $x_h = 57mm$ (b) $x_h = 98mm$ (c) $x_h = 126mm$

Fig. 9 Steady-state as a function of tail aspect ratio, from free-flight data. 1σ **error-bars.**

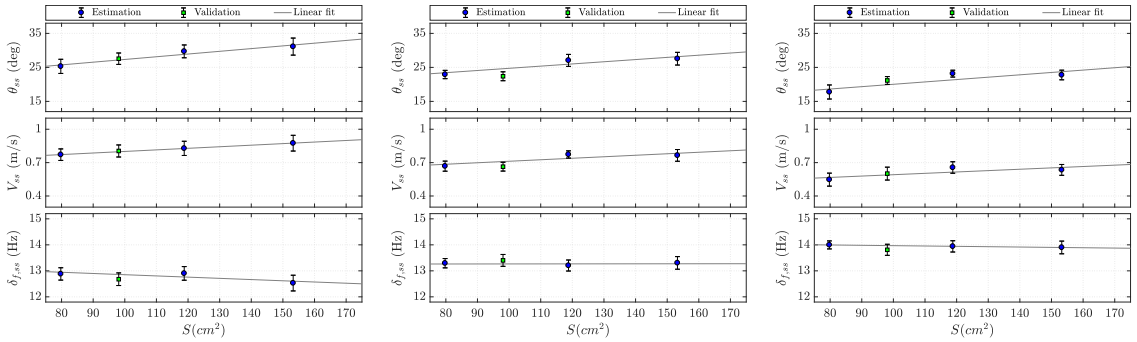

(a) $x_h = 57mm$ (b) $x_h = 98mm$ (c) $x_h = 126mm$

Fig. 10 Steady-state as a function of tail surface area, from free-flight data. 1σ **error-bars.**

Increasing the aspect ratio apparently increases the force generated by the tail and thus causes a larger pitch angle. This in turn tilts the wing force F_w (see Figure 5) and leads to a higher steady-state velocity. It is observed that the effect becomes less pronounced when the tail is moved farther away from the flapping wings, indicated by the less steep slope in the trend in Figure 9(c) in comparison to Figure 9(a).

Increasing the surface area has the same effect on the steady-state as aspect ratio, see Figure 10. However, surface area seems to have a smaller effect on the steady-state conditions than tail AR. Also, the slopes of the linear fits in Figure 10(a) and Figure 10(c) are very similar. This implies that the overall effect of surface area on the steady-state conditions does not vary with longitudinal position.

The steady-state conditions are plotted as a function of the longitudinal position in Figure 11. Increasing the separation from the main wing decreases the steady-state velocity and pitch angle. This is not fully in line with expectations. Moving the tail farther away from the main wing increases the moment arm of the tail force with respect to the CG (see Figure 5), suggesting that the tail would generate more nose-down moment and thus would yield a faster steady-state configuration.

The reason for this result is probably related to the CG shift. Changing the longitudinal position from $x_h = 57mm$ to $x_h = 126mm$ produces an average CG shift of $15.1mm$, depending on the used tail surface, causing a mean increase of the tail moment arm of approximately 74%. However, assuming F_w acting at the wing quarter chord point, the wing moment arm also increases by roughly 40%. According to earlier wind tunnel results the wings actually produce a small, negative contribution in x_b force, thus generating a nose up pitching moment [14, 30]. The steady-state trends observed in Figure 11 imply that the wing contribution is dominant in establishing the moment equilibrium. This can be confirmed by the wind tunnel data in Figure 8, showing that the magnitude of F_x excluding the tail typically reduces by less than 20%. Comparing Figure 11 to Figure 9 and Figure 10 also shows that, overall, the tail geometry has less impact on the steady-state conditions than the longitudinal position of the tail.

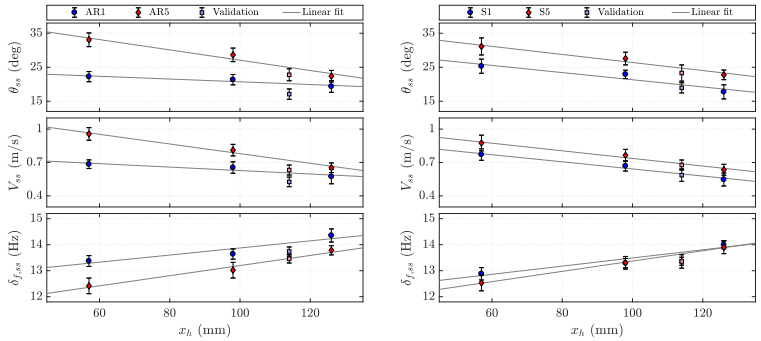

(a) For varying AR (b) For varying S

Fig. 11 Influence of longitudinal position on steady-state conditions. 1σ **error-bars.**

As mentioned before effect of tail position on the steady-state appears the same for configurations S1 and S5, indicated by the near-parallel linear fits in Figure 11(b), but Figure 11(a) shows that the difference in steady-state condition between AR1 and AR5 decreases when x_h increases. It appears that, close to the flapping wings, increasing the AR has more aerodynamic advantage than increasing tail surface area. However, this aerodynamic advantage seems to diminish when moving away from the flapping wings.

At increased x_h the free-stream component is expected to become more dominant over the flapping-wing induced velocity. Since the steady-state attitude is likely determined in part by the total drag of the system this result implies that, for large x_h, the tail is mainly producing a drag force determined mostly by its surface area. Since AR1 and AR5 in Figure 11(a) have the same surface area these ultimately converge to almost the same steady-state conditions when the longitudinal position of the tail increases.

The experiments for configurations AR1d, AR5d, S1d and S5d, e.g., the validation points in Figure 11, were conducted at a later time than the original experiments. Inevitably small changes in the system have taken place during this time, due to the large number of experiments performed. Since the ornithopter is very lightweight and vibrates continuously during flight such changes are inherent to the system and can have a significant impact on the steady-state conditions. This means that an accurate comparison of the steady-state conditions is difficult when measurements are not taken consecutively.

Additional data points were desired to validate if steady-state conditions may be predicted based on tail geometrical parameters. Thus, four additional tail configurations (AR4, AR6, S4, S6) were constructed after the initial experiments. To minimise effects of changes in the system, which can affect steady-state conditions as observed in Figure 11(b), steady-state experiments for $x_h = 57mm$ were repeated in a single day. The results of these experiments are shown in Figure 12. On-board data was not logged during these flights to reduce the required time to do the experiments. This does however mean that motor RPM data is lacking, leading to higher standard deviations in the flapping frequency estimate since it had to be determined solely from OptiTrack data.

Comparing the steady-state conditions in Figure 12(a) to the older ones in Figure 9 confirms that the steady-state conditions can actually vary significantly over time. Especially the results for configuration AR5a ($AR = 5.27$) have significantly changed. However, given that experiments are performed in succession, with minimal changes made to the system in between, it is in fact possible to accurately predict steady-state conditions as a simple, linear function of tail aspect ratio or surface area. The trends in Figure 12 are also the same as those found during earlier experiments (Figure 9 and Figure 10), and thus the observed effects of the tail geometry on the steady-state conditions are considered valid.

The prediction errors are summarised in Table 3, showing that the predictions are less than one standard deviation from the measurements. It is even possible to extrapolate the trends a little beyond the original estimation range and still predict the steady-state conditions with good accuracy. This provides interesting opportunities for future design tools.

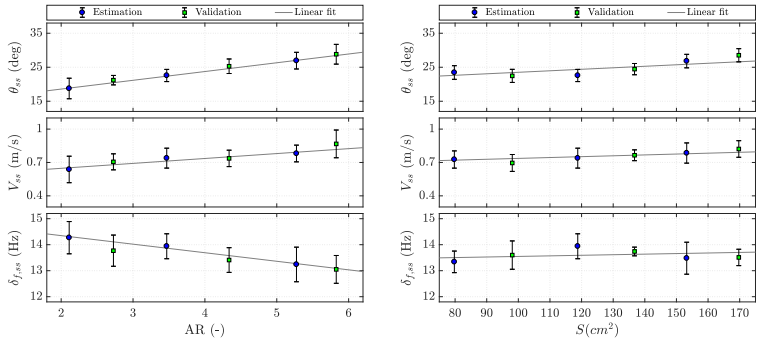

(a) Function of tail AR. (b) Function of tail S.

Fig. 12 New steady-state experiments performed to validate if steady-state conditions can be accurately predicted based on tail geometry. $\mathbf{x_h = 57mm}$. 1σ error-bars.

Table 3 Result of predicting steady-state conditions, for results in Figure 12, using linear fits.

	$\theta_{ss}(deg)$				$V_{ss}(ms^{-1})$				$\delta_{f,ss}(Hz)$			
Tail	x_m	$\hat{x}$	$\lvert x_m - \hat{x}\rvert$	$\lvert\frac{x_m-\hat{x}}{\sigma(x)}\rvert$	x_m	$\hat{x}$	$\lvert x_m - \hat{x}\rvert$	$\lvert\frac{x_m-\hat{x}}{\sigma(x)}\rvert$	x_m	$\hat{x}$	$\lvert x_m - \hat{x}\rvert$	$\lvert\frac{x_m-\hat{x}}{\sigma(x)}\rvert$
AR2a	21.20	20.48	0.74	0.54	0.71	0.67	0.03	0.36	13.77	14.11	0.34	0.57
AR4a	25.30	24.61	0.69	0.32	0.74	0.75	0.01	0.19	13.41	13.58	0.17	0.36
AR6a	28.83	28.45	0.37	0.13	0.87	0.82	0.05	0.40	13.05	13.09	0.04	0.07
S2a	22.46	23.43	0.97	0.50	0.70	0.74	0.04	0.21	13.60	13.54	0.06	0.10
S4a	24.45	25.14	0.69	0.42	0.76	0.77	0.01	0.29	13.74	13.63	0.11	0.66
S6a	28.53	26.60	1.93	1.00	0.82	0.79	0.03	0.06	13.51	13.70	0.19	0.61

2. Effect on dynamic behaviour

During free-flight experiments, differences in response were clearly visible for the different configurations. Analysing the time response of each configuration should thus provide valuable insights into the effect of the tail.

Figure 13 shows average time responses for varying AR. The average response is computed over all the manoeuvres performed during an experiment. The results show that an increased aspect ratio has a positive effect on damping capabilities and also slightly reduces the natural frequency of the oscillation. This might be partially caused by the increased span width of AR3 and AR5. This gives these configurations effective tail area in a span-wise region which experiences a high induced velocity wake, according to PIV measurements and numerical studies performed for this ornithopter (cf. Fig. 9 in [22] or Fig. 14 in [20]). Note that apparent differences in input in Figure 13 and other time response figures are caused by tracking problems of the elevator marker and subsequent averaging over multiple data segments.

The results in Figure 13 also show that the responses vary greatly with changing longitudinal position of the tail. When the distance to the flapping wings is small, Figure 13(a), increasing the aspect ratio seems to have a little more effect on the natural frequency of the oscillation but the responses are in fact quite similar. In Figure 13(b) the differences in average response are far more evident and clearly show increased damping for configurations AR3d and AR5d. Though the initial responses are almost identical, the peak at $t \approx 1.4s$ decreases considerably in magnitude for high AR configurations. These differences in damping are also apparent in Figure 13(c). In fact, increasing x_h beyond $114mm$ appears to drastically reduce the damping capabilities of configuration AR1c, and to lesser extent for AR2c, but it does not for AR3c and AR5c.

Figure 14 shows the average time responses for tails of different surface area. Differences in damping again become more apparent for increased longitudinal position of the tail, see Figure 14(c). From Figure 14(a) it seems that increasing the surface area beyond $S = 153.3cm^2$, i.e., from S5a to S6a, does not produce any significant change in dynamic response.

Increased surface area seems to have some effect on the natural frequency of the oscillation when the tail is close to the flapping wings, based on the time responses of in Figure 14(a), though

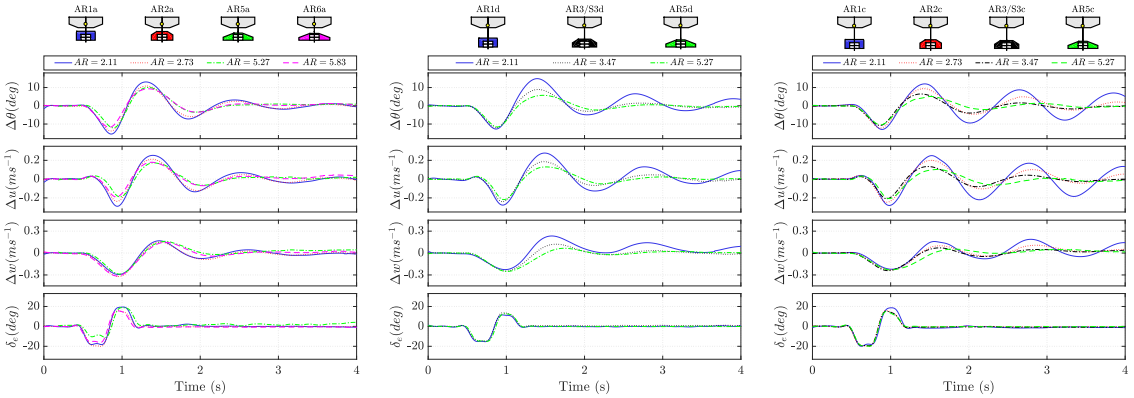

(a) $x_h = 57mm$ (b) $x_h = 114mm$ (c) $x_h = 126mm$

Fig. 13 Influence of tail aspect ratio on average time response to elevator doublet.

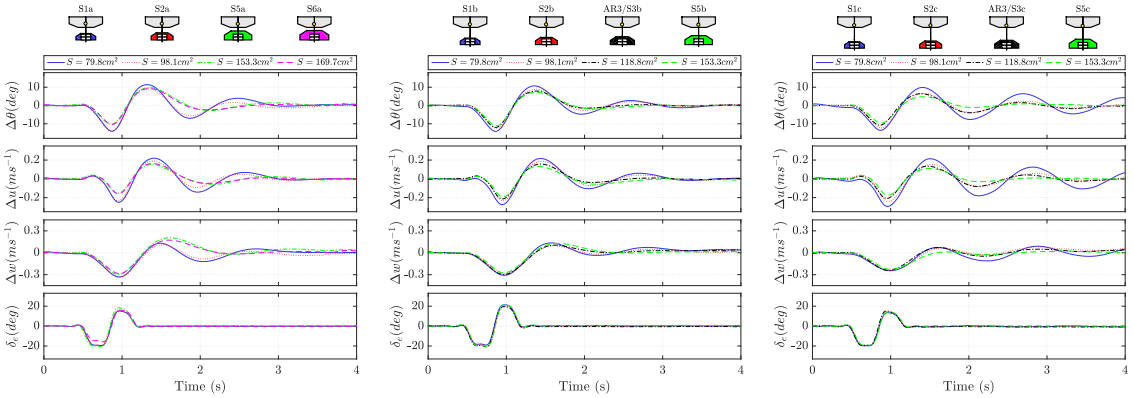

(a) $x_h = 57mm$ (b) $x_h = 98mm$ (c) $x_h = 126mm$

Fig. 14 Influence of tail surface area on average time response to elevator doublet.

the oscillations in Figure 14(c) are almost perfectly in-phase, showing only differences in damping. Damping is reduced for S1c in comparison to S1b. This is unexpected, since the tail moment arm increases from $x_h = 98mm$ to $x_h = 126mm$. Similar to the results for the steady-state conditions in Figure 11, this may be a result of the wing force also generating a larger, destabilising moment when the CG is moved further aft.

From Figure 13 and Figure 14 it is apparent that the longitudinal position of the tail has significant impact on the dynamic behaviour of the ornithopter for a given tail geometry. This is visualised more clearly in Figure 15, which shows results for tail configurations at varying longitudinal position.

Figure 15(c) shows that damping increases up to $x_h = 98mm$ but decreases significantly when the tail position is increased beyond that for configuration AR1. The same is observed for configuration S1, Figure 15(a), though the difference is smaller than for AR1. In contrast, Figure 15(b) shows that damping of the oscillation remains high even up to $x_h = 126mm$ for configuration AR3/S3. Increasing the distance between the tail and the flapping wings is actually expected to improve damping, as the moment arm of the tail force increases (see Figure 5). Given that configuration S3/AR3 matches the aspect ratio of configuration S1 and the surface area of configuration AR1, the decrease in damping at high x_h, for configurations AR1c and S1c, cannot be linked directly to either surface area or aspect ratio of the tail surface.

It is expected that the maximum span width of the tails plays a role in the explanation of this result. Configurations S1 and AR1 feature relatively small span widths of 158 and $166mm$ respectively. Configuration S3 has a larger span width of $203mm$. The results observed in Figure 15 could be explained by the typical induced velocity profile of flapping wings, which experiences peaks at $60 - 70\%$ of the flapping wing span [22, 36]. Energy in the wake of the flapping wings dissipates

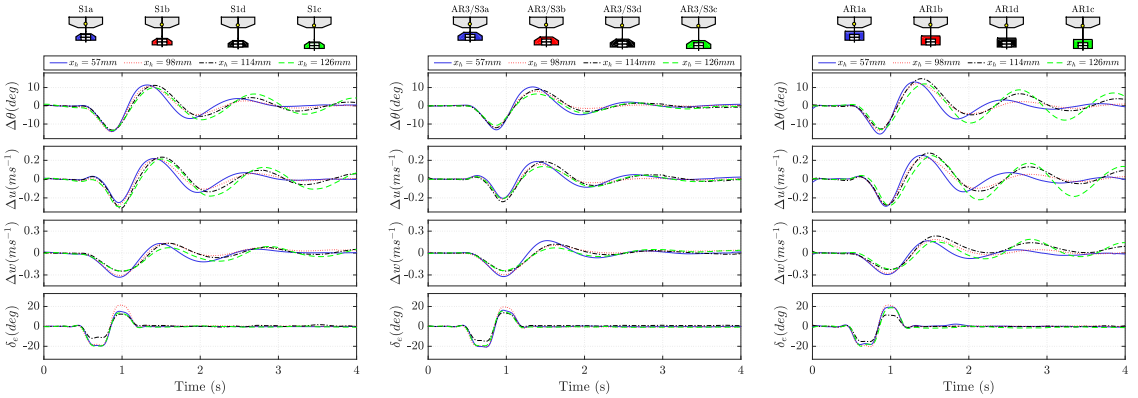

(a) S1 ($S = 79.8cm^2,\ AR = 3.45$)

(b) AR3/S3 ($S = 118.8cm^2,\ AR = 3.47$)

(c) AR1 ($S = 118.2cm^2,\ AR = 2.11$)

Fig. 15 Influence of longitudinal position on average time response to elevator doublet.

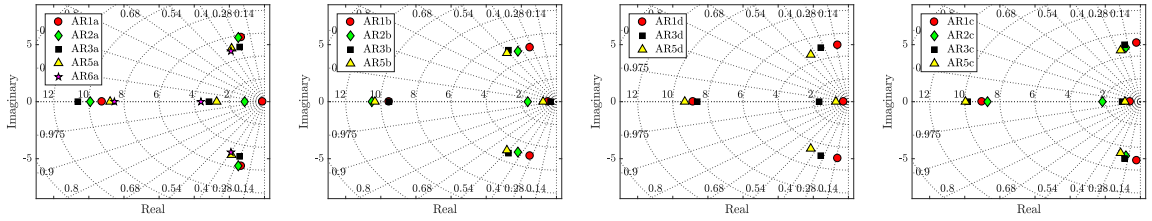

(a) $x_h = 57mm$

(b) $x_h = 98mm$

(c) $x_h = 114mm$

(d) $x_h = 126mm$

Fig. 16 Pole plots illustrating effect of tail aspect ratio on the system eigenvalues.

when moving downstream in chord-wise direction, decreasing the magnitude of the induced velocity. The region of high induced velocity is also found to decrease in span-wise direction when moving further away from the flapping wings, resembling a bell shape (cf. Fig. 8 in [22]). In light of this, tails with a smaller span width are likely not seeing this high induced velocity field anymore when x_h is large, thus drastically reducing their effectiveness when the longitudinal position exceeds $98mm$.

The time responses indicate changes in damping and natural frequency of the oscillatory eigenmode of the ornithopter, which can be further studied by analysing the eigenvalues of the estimated models. Figure 16 shows the results for varying tail aspect ratio. The plots illustrate the eigenvalues of the most representative averaged model for each configuration, based on the validation results (see Table A.2). There is a clear trend in the complex conjugate pair of eigenvalues but the real eigenvalues show less consistent trends. As mentioned earlier, the real eigenvalues for individual models generally are less consistent than the complex conjugate eigenvalues (see Figure 7(b)), though it is clear that the ornithopter has two aperiodic eigenmodes with eigenvalues at approximately -1 and -10. The inconsistency in the aperiodic eigenvalues was also encountered in previous system identification work and is likely caused by insufficient excitation of the dynamics associated with these eigenvalues, i.e., the dynamics in the body z_b-axis [13].

In line with the time response results in Figure 13, increasing the tail AR slightly reduces the natural frequency of the response and has some positive effect on damping for $x_h = 57mm$, Figure 16(a). For $x_h = 114mm$ and higher, Figure 16(c) and Figure 16(d), increasing the AR leads to significant improvements in damping of the oscillation but hardly has an effect on the natural frequency.

Figure 17 shows the pole-zero plots for varying tail surface area. The results are similar to those seen for changing the AR and are again in line with what is observed in the average time responses in Figure 14. The complex conjugate eigenvalues for the two largest tail configurations, S5a and S6a in Figure 17(a) are in fact very similar which corresponds to the marginal difference in time response observed in Figure 14(a).

Figure 17(b) shows that for $x_h = 98mm$ an increase in surface area already mostly has an

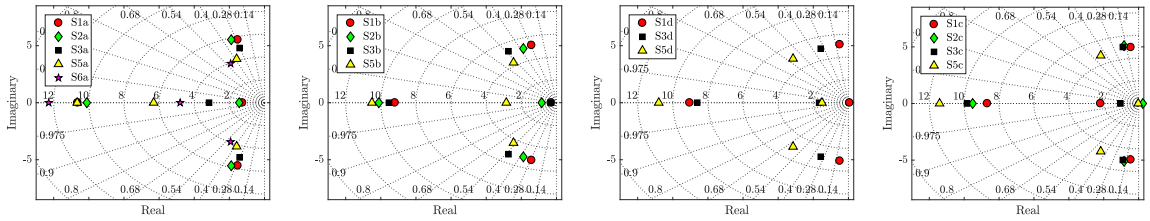

(a) $x_h = 57mm$ (b) $x_h = 98mm$ (c) $x_h = 114mm$ (d) $x_h = 126mm$

Fig. 17 Pole plots illustrating effect of tail surface area on the system eigenvalues.

Table 4 Estimated stability derivatives and standard deviations for varying S, $x_h = 98mm$.

	S1b		S2b		S3b		S5b	
	$\hat{\theta}$	$100\lvert\hat{\sigma}/\hat{\theta}\rvert$	$\hat{\theta}$	$100\lvert\hat{\sigma}/\hat{\theta}\rvert$	$\hat{\theta}$	$100\lvert\hat{\sigma}/\hat{\theta}\rvert$	$\hat{\theta}$	$100\lvert\hat{\sigma}/\hat{\theta}\rvert$
M_q	-4.41e-04	0.48	-6.46e-04	0.57	-7.30e-04	0.49	-9.03e-04	0.54
M_u	-1.90e-03	0.45	-1.79e-03	0.64	-2.06e-03	0.67	-1.70e-03	0.66
M_w	-3.76e-05	23.30	-7.91e-04	2.05	-6.59e-04	1.56	-1.27e-03	0.82
X_q	1.89e-02	0.77	1.85e-02	1.05	2.93e-02	0.47	3.15e-02	0.50
X_u	-1.30e-01	0.56	-1.26e-01	0.45	-1.34e-01	0.34	-1.43e-01	0.23
X_w	-1.13e-02	6.06	-4.13e-02	1.57	-2.12e-02	1.56	-3.06e-02	0.98
Z_q	-1.26e-03	19.63	1.79e-03	24.20	1.36e-03	29.17	-2.22e-03	11.04
Z_u	1.84e-02	4.56	1.78e-02	5.96	-7.86e-04	123.50	1.58e-02	3.67
Z_w	-1.07e-02	4.16	-9.43e-03	8.10	2.05e-03	23.80	-1.79e-02	2.71

effect on damping, while there is quite a significant effect on the natural frequency of the response for $x_h = 57mm$ in Figure 17(a). For $x_h = 126mm$, in Figure 17(d), increasing the surface area mostly results in an increase in damping. The results imply that the behaviour of the system changes significantly for longitudinal tail positions between $98 - 114mm$. Configurations S1 and S3 lose considerable damping capabilities between these two fuselage lengths, as can be seen from Figure 17(b) and Figure 17(c). This is most likely related to the strength of the wake induced by the flapping wings and may be related to the free-stream velocity becoming dominant over flapping-wing induced velocity at increased distance from the flapping wings. In that case the horizontal tail most likely acts as a flat plate translating at high angle of attack, causing significant decreases in aerodynamic force generation [28].

Wake modelling for this ornithopter, in hover conditions, in a recent study by Armanini et al. ([22]) confirms that the induced velocity indeed decreases significantly with increased distance from the flapping wings. In this study the flow conditions at the tail are modelled by simple addition of the induced flow in hover to free-stream velocities encountered in free-flight. Future work should perform wake modelling in real slow forward flight conditions, using a wind tunnel for example, to investigate the actual interaction between free-stream flow and flapping-wing induced flow. This should help determine at which distance from the flapping wings the free-stream component in fact starts to become dominant.

The ability to design configurations with specific dynamic properties based on tail geometry, using simple models, would be a great benefit for FWMAV development. As an example, Table 4 shows the estimated stability derivatives for varying surface area and the estimated standard deviations. These are the model parameters of the most representative average models, which for all of these configurations was the TA model. The parameter values in Table 4 are in the same order of magnitude as those found in previous system identification efforts performed for this FWMAV [27]. From the estimated standard deviations in Table 4 it is clear that most parameters are estimated quite successfully. Parameters coupled to the body z_b-axis do show high estimated standard deviations, which is likely caused by a lack of excitation in this direction and seems to correspond to the less consistent real eigenvalues seen in Figure 17. The same lack of excitation is suspected to cause the high estimated standard deviations for M_w, X_w and Z_w.

Table 4 does not immediately reveal very clear trends in the model parameters with changing

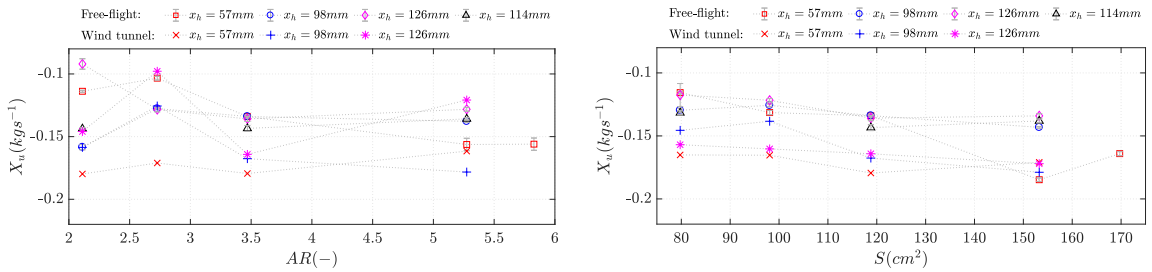

(a) As function of AR.

(b) As function of surface area.

Fig. 18 Effect of tail geometry on X_u, estimated from free-flight and wind tunnel data.

surface area. In general, identifying trends in the model parameters based on tail geometry proved to be very difficult using the current modelling efforts. The results for two parameters which are important in determining dynamic stability, X_u and M_q, are shown in Figure 18 and Figure 19. Only the parameter values of the most representative model for each configuration are presented here.

X_u is a measure of the drag force as a result of changes in forward velocity. It is expected that the drag is influenced by the geometry of the tail, in particular surface area. Based on the results in Figure 18, X_u indeed shows a stronger trend with surface area than with aspect ratio. X_u seems fairly constant with differing aspect ratio according to the data in Figure 18(a). Figure 18(b) shows a slightly more distinct trend, with an increasing magnitude of X_u for higher surface area. This is in line with expectations, since a higher surface area translating through air generally leads to a higher drag force. The wind tunnel results also show a slight trend with tail surface area, Figure 18(b), but vary quite a bit from the free-flight results in magnitude. Actually comparing these stability derivatives would require more study into the accuracy of both experimental methods (see also Caetano et al. [31]). Ultimately, the results in Figure 18(b) do not show very conclusive trends and it was not considered feasible to develop a model for X_u as a function of tail surface area.

M_q is an important stability parameter determining the corrective moment generated in case of a pitch disturbance. For dynamic stability its sign should be negative. Figure 19 shows the results as a function of tail geometry. Again, surface area appears to have more effect, though a trend is also visible for increasing aspect ratio, Figure 19(a). Increasing AR or surface area leads to an increase in magnitude of M_q. This is in line with the observations that increasing tail surface area or AR has a positive effect on damping (see Figure 16 and Figure 17). Also in line with previous observations, surface area has more effect on the damping capabilities of the tail surface than aspect ratio, illustrated by the larger increase in magnitude of M_q in Figure 18(b), especially for configuration S5 ($S = 153.3cm^2$).

From Figure 19 it is also observed that M_q is not significantly influenced by the longitudinal position of the tail. This suggests that changes in damping for a specific tail at different longitudinal positions x_h may result more from an increase in inertia (I_{yy}) than due to changes in the aerodynamic effect of the tail. Increasing the longitudinal position of the tail from $x_h = 57mm$ to $x_h = 126mm$ actually increases I_{yy} by an average 150%, due to mass moving further away from the CG. The results in Figure 19 indicate that the aerodynamic damping capabilities of most tail geometries increases up to $x_h = 98mm$. When the distance between the tail and the flapping wings is increased even further, inertia effects become dominant.

The results in Figure 19 do suggest that increasing AR and/or surface area increases F_h, which in turn leads to a larger stabilising moment generated by the tail (also refer back to Figure 5). On top of that, the added mass force may also play a role here. As the ornithopter experiences acceleration it is subjected to a reaction force of the accelerated fluid surrounding it. This is often modelled using a quasi-steady approach with a time-invariant added mass coefficient [5]. During manoeuvres the FWMAV experiences very high angular accelerations about the body y_b axis. Armanini et al. model the added mass of the wing as that of a flat plate, being a quadratic function of local chord length (c^2) integrated along the span-wise direction [14]. Assuming the same relation for the tail surface could help explain the larger variation in M_q for increasing surface area, as these tails feature larger variation in chord length (refer to Table A.1).

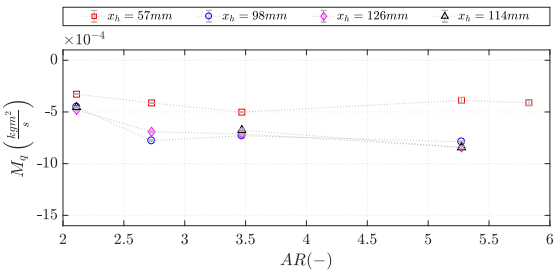

(a) As function of AR.

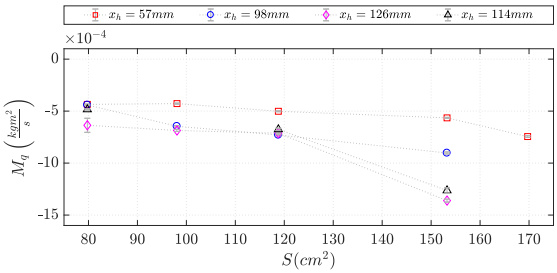

(b) As function of S.

Fig. 19 Effect of tail geometry on M_q, from free-flight data.

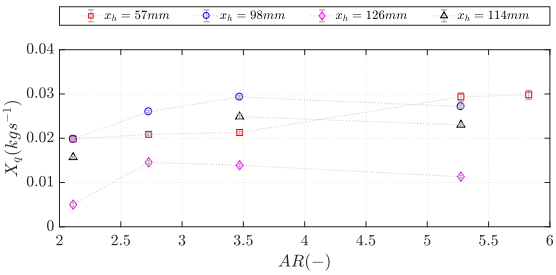

(a) As function of AR.

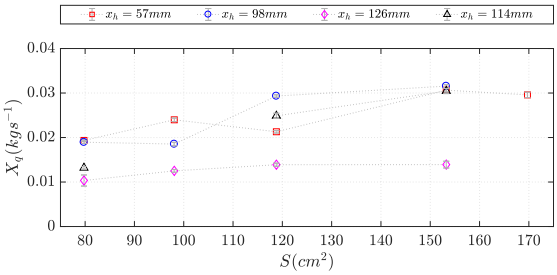

(b) As function of S.

Fig. 20 Effect of tail geometry on X_q, from free-flight data.

The cross-coupling terms M_u and X_q are also important parameters in terms of the oscillatory response of the system. Results from free-flight are given in Figure 20 and Figure 21. Increasing the tail aspect ratio or the surface area leads to a slight increase in X_q. This corresponds to an improvement of the damping capabilities. Figure 20 also shows an influence of the longitudinal position on the magnitude of X_q, though there is no clear trend. It appears that X_q increases in magnitude with increasing longitudinal position at first (up to $x_h = 98mm$) and then decreases again for $x_h = 114mm$ and higher, especially clear in the results for $AR = 3.47$ in Figure 20(a).

The results in Figure 21 do not show any significant effects of the tail geometry on the magnitude of M_u. There is however a rather clear trend with the longitudinal position of the tail. The results indicate that coupling between the velocity in body x_b-axis and the pitching moment increases when the tail is moved further away from the flapping wings. This is as would be expected since increasing x_h increases the moment arms of both the wings and the tail surface. The negative sign of M_u indicates that an increase in body velocity u leads to a negative, i.e., pitch up, moment change. This, and the fact that M_u does not change significantly with tail geometry, according to the results in Figure 21, implies that the wing force is dominant in contributing to M_u.

In general the averaged models, for a given configuration, showed quite large variations in model

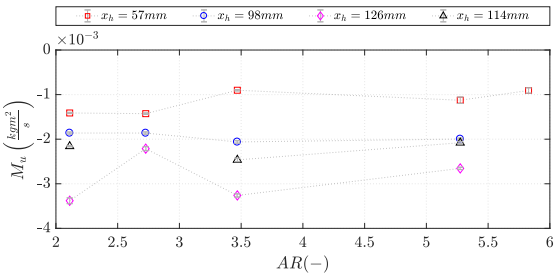

(a) As function of AR.

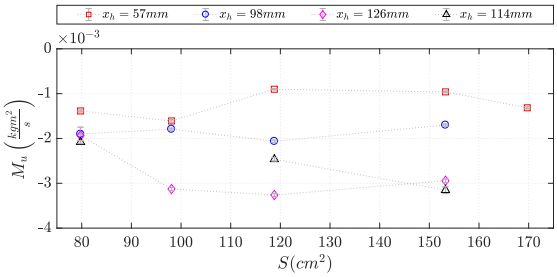

(b) As function of S.

Fig. 21 Effect of tail geometry on M_u, from free-flight data.

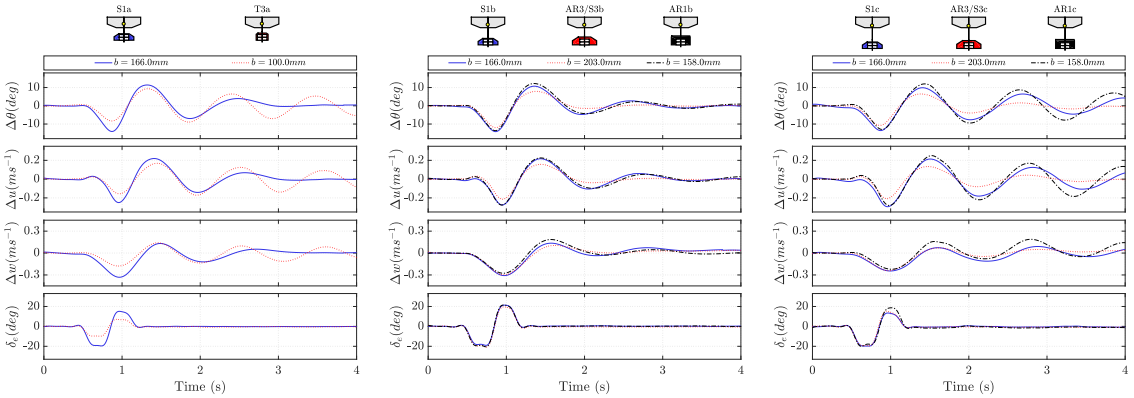

(a) $x_h = 57mm$ (b) $x_h = 98mm$ (c) $x_h = 126mm$

Fig. 22 Effect of tail span width on average time response.

parameters even though the resulting predicted behaviour was similar, especially for the oscillatory component. This suggests that some model parameters, such as Z_u and X_w, have little effect on the pitch dynamics. The results in Table 4 confirm this, as the relatively high standard deviations of these parameters seemingly do not have a significant impact on the performance of the models. For a better understanding of the model parameters and their specific effect on the final model performance it is suggested to perform a systematic sensitivity analysis of the LTI model parameters in future work. Fixing some of the less important parameters might improve the accuracy of the overall model and decrease the variability of the important parameters such as M_q.

3. Effect of tail span width

From the results in Figure 15 the hypothesis arose that the maximum span width of the horizontal tail plays a role in the dynamic behaviour of the ornithopter. The behaviour of tail configurations with the same AR and surface area seems to vary significantly when the distance between the tail and the flapping wings is large. To illustrate, Figure 22 shows time response results for several tails as a function of their maximum span width.

Most notable is the large difference in response between configurations T3a and S1a in Figure 22(a). Configuration T3a starts oscillating heavily about its steady-state even with a smaller elevator input, while tail S1a is damped fairly well. Configurations T3b and T3c even tended to be destabilised by 30% elevator deflections, making it impossible to accurately estimate LTI models for these configurations. The difference in behaviour seen in Figure 22(a) is more extreme than expected from the difference in surface area and aspect ratio alone, based on the results in Figure 13 and Figure 14. It is expected that the increased span width of configuration S1a may contribute to this significant increase in damping capabilities, since the induced velocity in the in-board region, close to the root of the flapping wings, decreases significantly [20, 22, 36].

The results in Figure 22(b) and Figure 22(c) support this hypothesis. These figures show results for two configurations with similar maximum span width (S1 and AR1) and one configuration with a larger span width (AR3/S3), at two different longitudinal positions x_h. Despite differences of 63.6% and 48.2% in AR and surface area, respectively, between configurations S1 and AR1, the responses of these configurations are very similar, especially in terms of damping. Configuration AR3c, Figure 22(c), which has a larger maximum span width, shows much better damping capabilities even though it has the same aspect ratio as configuration S1 and the same surface area as configuration AR1. The aerodynamic importance of maximum span width has previously been noted by Thomas in his study of bird tail aerodynamics [18]. The results in Figure 22 seem to support this.

Since AR, surface area and span width are all related through the relation for aspect ratio (Equation (1)) it is impossible to isolate the contribution of one of these parameters to the dynamic behaviour without changing at least one of the other variables. Therefore additional research is needed to give definitive conclusions about the relevance of the maximum span width. It is recommended to extend previous studies, modelling the wake of the flapping wings of this ornithopter

in hover conditions by means of PIV measurements ([22]), to slow forward flight conditions. This should give more insight into the flow conditions at the tail, especially in span-wise direction, and may help to quantify the effect of the span width of the tail surface on its total effectiveness.

V. Conclusion

This paper presented the results of a systematic study into the effect of the horizontal tail on the time-averaged dynamics of a flapping-wing micro aerial vehicle, the DelFly II. Three parameters were varied to investigate their effect: surface area, aspect ratio and longitudinal position.

It was found that increased surface area and aspect ratio provides a larger pitch down moment, tipping the moment equilibrium and thus increasing steady-state velocity. It can be concluded that the tail force increases in magnitude with increased S and AR. Using additional test configurations it was shown that prediction of the steady-state conditions based on tail geometry is possible with simple linear relations. This provides interesting opportunities for future FWMAV platform design tools.

Increasing the longitudinal position of the tail decreases the steady-state velocity. This is most likely caused by the shift in CG position. Based on the results, forces generated by the wing are dominant in determining the moment equilibrium and therefore the increased moment arm of the wing results in slower flight. Results also suggest that the effectiveness of the tail decreases with increased distance to the flapping wings, possibly due to less energy being available in the wake.

Increasing aspect ratio and surface area generally increases damping of the periodic, oscillatory eigenmode and slightly decreases natural frequency. For increased distance to the flapping wings the effect on natural frequency becomes less but significant changes in damping were observed. Some tail geometries experienced a significant decrease in damping capabilities at longitudinal positions exceeding $98mm$. This appears connected to the maximum span width of the tail surface rather than just its surface area or aspect ratio. More research into the effect of maximum tail span width is recommended.

Trends were identified in some stability derivatives, mainly M_q, X_q, M_u and X_u. However, the current models did not reveal trends with enough confidence to predict dynamic behaviour based on tail geometry. Future studies may focus more on the system identification cycle to improve model accuracy, for example with a thorough sensitivity study of the model parameters. It is also recommended to further investigate the possibility of increasing model accuracy using throttle input data, as this provides better excitation in the body z_b axis than elevator inputs.

In the context of novel FWMAV platform designs, it is suggested to systematically study the effect of a non-zero angle of the horizontal tail with respect to the fuselage. Some birds tilt their tails for flight control purposes and it should be interesting to study the potential benefits of such a feature for robotic flappers. Future research may also focus on the vertical tail surface and its effects on the lateral dynamics of the ornithopter.

Appendix

Table A.1 Physical dimensions of the tail geometries used in the experiments.

	Tail identifier													
Parameter	S1	S2	S3/AR3	S4	S5	S6	AR1	AR2	AR4	AR5	AR6	T1	T2	T3
b (mm)	166	184	203	217	230	242	158	180	227	250	260	170	170	100
b_{LE} (mm)	87	96	105	112	120	126	152	90	80	70	76	80	-	70
c_r (mm)	54	60	66	71	75	79	75	73	64	60	57	71	73	60
c_t (mm)	29	32	35	38	40	42	66	45	28	25	22	38	24	50
AR $(-)$	3.45	3.45	3.47	3.44	3.45	3.45	2.11	2.73	4.34	5.27	5.83	2.73	2.72	1.71
S (cm^2)	79.8	98.1	118.8	136.7	153.3	169.7	118.2	118.8	118.82	118.5	116.0	105.9	106.2	58.5

Table A.2 Mean validation scores, standard deviation in brackets. Not all configurations were tested. For T3b and T3c, modelling was unsuccessful.

		Fuselage configuration							
		a ($x_h = 57mm$)		b ($x_h = 98mm$)		c ($x_h = 126mm$)		d ($x_h = 114mm$)	
Tail	Model	RMS	PCC	RMS	PCC	RMS	PCC	RMS	PCC
S1	TA	0.12 (0.02)	0.88 (0.03)	0.11 (0.01)	0.87 (0.05)	0.10 (0.01)	0.86 (0.02)	0.11 (0.02)	0.84 (0.05)
	WM	0.12 (0.02)	0.87 (0.02)	0.16 (0.02)	0.64 (0.11)	0.11 (0.01)	0.85 (0.05)	0.13 (0.01)	0.84 (0.04)
	Mean	0.12 (0.01)	0.86 (0.05)	0.11 (0.01)	0.83 (0.06)	0.09 (0.01)	0.88 (0.05)	0.13 (0.03)	0.77 (0.11)
S2	TA	0.10 (0.02)	0.84 (0.09)	0.11 (0.02)	0.86 (0.05)	0.10 (0.01)	0.83 (0.09)	-	-
	WM	0.12 (0.02)	0.72 (0.12)	0.14 (0.01)	0.78 (0.05)	0.20 (0.03)	0.63 (0.13)	-	-
	Mean	0.10 (0.02)	0.81 (0.11)	0.12 (0.01)	0.80 (0.05)	0.10 (0.02)	0.79 (0.04)	-	-
S3/AR3	TA	0.12 (0.02)	0.78 (0.08)	0.09 (0.01)	0.87 (0.03)	0.10 (0.01)	0.80 (0.06)	0.09 (0.01)	0.90 (0.06)
	WM	0.17 (0.02)	0.62 (0.14)	0.10 (0.02)	0.81 (0.07)	0.11 (0.01)	0.75 (0.06)	0.13 (0.02)	0.73 (0.12)
	Mean	0.12 (0.02)	0.75 (0.07)	0.10 (0.01)	0.86 (0.03)	0.10 (0.01)	0.79 (0.05)	0.09 (0.01)	0.90 (0.05)
S5	TA	0.09 (0.04)	0.86 (0.07)	0.08 (0.02)	0.88 (0.03)	0.09 (0.02)	0.79 (0.04)	0.11 (0.03)	0.80 (0.08)
	WM	0.11 (0.04)	0.82 (0.06)	0.11 (0.01)	0.76 (0.05)	0.12 (0.02)	0.59 (0.07)	0.16 (0.02)	0.48 (0.09)
	Mean	0.09 (0.04)	0.85 (0.07)	0.09 (0.02)	0.84 (0.04)	0.10 (0.02)	0.71 (0.07)	0.12 (0.02)	0.76 (0.11)
S6	TA	0.09 (0.03)	0.89 (0.05)	-	-	-	-	-	-
	WM	0.11 (0.02)	0.85 (0.05)	-	-	-	-	-	-
	Mean	0.09 (0.03)	0.89 (0.05)	-	-	-	-	-	-
AR1	TA	0.14 (0.05)	0.78 (0.27)	0.12 (0.02)	0.86 (0.01)	0.13 (0.01)	0.86 (0.04)	0.14 (0.02)	0.84 (0.06)
	WM	0.15 (0.04)	0.73 (0.24)	0.18 (0.01)	0.59 (0.06)	0.16 (0.05)	0.78 (0.13)	0.13 (0.04)	0.84 (0.07)
	Mean	0.14 (0.05)	0.75 (0.29)	0.12 (0.02)	0.83 (0.03)	0.18 (0.02)	0.75 (0.07)	0.14 (0.03)	0.81 (0.11)
AR2	TA	0.10 (0.04)	0.89 (0.05)	0.11 (0.03)	0.87 (0.07)	0.08 (0.02)	0.89 (0.04)	-	-
	WM	0.13 (0.03)	0.80 (0.06)	0.12 (0.03)	0.82 (0.09)	0.09 (0.02)	0.85 (0.05)	-	-
	Mean	0.10 (0.03)	0.87 (0.05)	0.11 (0.03)	0.85 (0.06)	0.08 (0.02)	0.88 (0.04)	-	-
AR5	TA	0.12 (0.03)	0.85 (0.05)	0.10 (0.02)	0.83 (0.08)	0.11 (0.01)	0.70 (0.15)	0.12 (0.03)	0.82 (0.02)
	WM	0.18 (0.03)	0.72 (0.07)	0.12 (0.01)	0.75 (0.07)	0.13 (0.01)	0.53 (0.07)	0.13 (0.03)	0.76 (0.08)
	Mean	0.10 (0.03)	0.86 (0.06)	0.10 (0.03)	0.78 (0.09)	0.11 (0.01)	0.65 (0.19)	0.13 (0.04)	0.73 (0.11)
AR6	TA	0.11 (0.02)	0.85 (0.05)	-	-	-	-	-	-
	WM	0.12 (0.02)	0.80 (0.07)	-	-	-	-	-	-
	Mean	0.10 (0.02)	0.87 (0.06)	-	-	-	-	-	-
T1	TA	0.11 (0.03)	0.88 (0.06)	0.10 (0.03)	0.88 (0.05)	0.14 (0.03)	0.76 (0.07)	-	-
	WM	0.75 (0.65)	0.44 (0.23)	0.15 (0.04)	0.74 (0.10)	0.29 (0.09)	0.32 (0.28)	-	-
	Mean	0.11 (0.03)	0.87 (0.04)	0.10 (0.03)	0.87 (0.06)	0.13 (0.04)	0.76 (0.10)	-	-
T2	TA	0.10 (0.01)	0.86 (0.03)	0.11 (0.05)	0.90 (0.06)	0.67 (0.61)	0.47 (0.30)	-	-
	WM	0.17 (0.03)	0.75 (0.07)	0.15 (0.03)	0.75 (0.11)	0.19 (0.03)	0.68 (0.18)	-	-
	Mean	0.12 (0.01)	0.83 (0.04)	0.13 (0.05)	0.82 (0.08)	0.17 (0.03)	0.67 (0.16)	-	-
T3	TA	0.29 (0.13)	0.87 (0.12)	-	-	-	-	-	-
	WM	1.16 (0.85)	0.44 (0.21)	-	-	-	-	-	-
	Mean	0.34 (0.10)	0.67 (0.09)	-	-	-	-	-	-

References

[1] Dickinson, M., Lehmann, F., and Sane, S., "Wing Rotation and the Aerodynamic Basis of Insect Flight," *Science*, Vol. 284, 1999, pp. 1954–1960.

[2] Ellington, C., "The Aerodynamics of Hovering Insect Flight. I. The Quasi-Steady Analysis," *Philosophical Transactions of the Royal Society of London, Series B: Biological Sciences*, Vol. 305, 1984, pp. 1–15.

[3] Chin, D. and Lentink, D., "Flapping wing aerodynamics: from insect to vertebrates," *Journal of Experimental Biology*, Vol. 219, 2016, pp. 920–932.

[4] Sane, S. and Dickinson, M., "The aerodynamic effects of wing rotation and a revised quasi-steady model of flapping flight," *Journal of Experimental Biology*, Vol. 205, 2002, pp. 1087–1096.

[5] Sane, S. P., "The aerodynamics of insect flight," *Journal of Experimental Biology*, Vol. 206, 2003, pp. 4191–4208.

[6] Birch, J. and Dickinson, M., "The influence of wing-wake interactions on the production of aerodynamic force in flapping flight," *Journal of Experimental Biology*, Vol. 206, 2003, pp. 2257–2272.

[7] de Croon, G., Groen, M., de Wagter, C., Remes, B., Ruijsink, R., and van Oudheusden, B., "Design, aerodynamics and autonomy of the DelFly," *Bioinspiration & Biomimetics*, Vol. 7, No. 2, 2012, pp. 1–16.

[8] Grauer, J., Ulrich, E., Hubbard, J., Pines, D., and Humbert, J., "Testing and System Identification of an Ornithopter in Longitudinal Flight," *Journal of Aircraft*, Vol. 48, No. 2, 2011, pp. 660–667.

[9] Rosen, M., le Pivain, G., Sahai, R., Jafferis, N., and Wood, R., "Development of a 3.2g Untethered Flapping-Wing Platform for Flight Energetics and Control Experiments," in "2016 IEEE International Conference on Robotics and Automation (ICRA)," Stockholm, Sweden, 2016, pp. 3227–3233.

[10] Ma, K., Chirarattananon, P., Fuller, S., and Wood, R., "Controlled Flight of a Biologically Inspired, Insect-Scale Robot," *Science*, Vol. 340, 2013, pp. 603–607.

[11] Keennon, M., Klingebiel, K., Won, H., and Andriukov, A., "Development of the Nano Hummingbird: A Tailless Flapping Wing Micro Air Vehicle," in "50th AIAA Aerospace Sciences Meeting including the New Horizons Forum and Aerospace Exposition," Nashville, Tennessee, 2012.

[12] Caetano, J., de Visser, C., de Croon, G., Remes, B., de Wagter, C., Verboom, J., and Mulder, M., "Linear Aerodynamic Model Identification of a Flapping Wing MAV Based on Flight Test Data," *International Journal of Micro Air Vehicles*, Vol. 5, 2013, pp. 273–286.

[13] Armanini, S., Karásek, M., de Visser, C., de Croon, G., and Mulder, M., "Flight testing and preliminary analysis for global system identification of ornithopter dynamics using on-board and off-board data," in "AIAA Atmospheric Flight Mechanics Conference," Grapevine, Texas, 2017.

[14] Armanini, S., Caetano, J., de Croon, G., de Visser, C., and Mulder, M., "Quasi-Steady Aerodynamic Model of Clap-and-Fling Flapping MAV and Validation using Free-Flight Data," *Bioinspiration & Biomimetics*, Vol. 11, No. 4.

[15] Groen, M., Bruggeman, B., Remes, B., Ruijsink, R., van Oudheusden, B., and Bijl, H., "Improving flight performance of the flapping wing MAV DelFly II," in "International Micro Air Vehicle conference and competitions (IMAV 2010)," , 2010.

[16] de Croon, G., de Clerq, K., Ruijsink, R., Remes, B., and de Wagter, C., "Design, aerodynamics, and vision-based control of the DelFly," *International Journal of Micro Air Vehicles*, Vol. 1, No. 2, 2009, pp. 71–97.

[17] Wood, R., "The First Takeoff of a Biologically Inspired At-Scale Robotic Insect," *IEEE Transactions on Robotics*, Vol. 24, No. 2, 2008, pp. 341–347.

[18] Thomas, A., "On the aerodynamics of birds' tails," *Philos. Trans. R. Soc. London, Ser. B*, Vol. 340, 1993, pp. 361–380.

[19] de Croon, G., Percin, M., Remes, B., Ruijsink, R., and de Wagter, C., *The DelFly: Design, Aerodynamics, and Artificial Intelligence of a flapping Wing Robot*, Springer, 2016.

[20] Tay, W., Bijl, H., and van Oudheusden, B., "Biplane and Tail Effects in Flapping Flight," in "42nd AIAA Fluid Dynamics Conference and Exhibit," New Orleans, 2012.

[21] Maybury, W., Rayner, J., and Couldrick, L., "Lift generation by the avian tail," *Philosophical Transactions of the Royal Society of London, Series B: Biological Sciences*, Vol. 268, 2001, pp. 1443–1448.

[22] Armanini, S., Caetano, J., de Visser, C., and de Croon, G., "Modelling wing wake and tail-wake interaction of a clap-and-peel flapping-wing MAV," in "AIAA Modeling and Simulation Technologies Conference," Grapevine, Texas, 2017.

[23] Caetano, J., de Visser, C., Remes, B., de Wagter, C., and Mulder, M., "Modeling a Flapping Wing MAV: Flight Path Reconstruction of the Delfly II," in "AIAA Modeling and Simulation Technologies (MST) Conference, Boston, MA.", , 2013.

[24] Caetano, J., de Visser, C., Remes, B., de Wagter, C., van Kampen, E.-J., and Mulder, M., "Controlled Flight Maneuvers of a Flapping Wing Micro Air Vehicle: a Step Towards the Delfly II Identification," in "2013 AIAA Atmospheric Flight Mechanics Conference," , 2013.

[25] Karásek, M., Koopmans, A., Armanini, S., Remes, B., and de Croon, G., "Free flight force estimation of a 23.5g flapping wing MAV using an on-board IMU," in "IEEE International Conference on Intelligent Robots and Systems (IROS)," Daejeon, Korea, 2016.

[26] Armanini, S., Karásek, M., de Croon, G., and de Visser, C., "Onboard/Offboard Sensor Fusion for High-Fidelity Flapping-Wing Robot Flight Data (in press)," *Journal of Guidance, Control, and Dynamics*.
[27] Armanini, S., de Visser, C., de Croon, G., and Mulder, M., "Time-Varying Model Identification of Flapping-Wing Vehicle Dynamics Using Flight Data," *Journal of Guidance, Control, and Dynamics*, Vol. 39, No. 3, 2016, pp. 526–541.
[28] Anderson, J. D., *Fundamentals of Aerodynamics*, McGraw Hill, 5th SI units ed., 2011.
[29] Percin, M., Eisma, H., van Oudheusden, B., Remes, B., Ruijsink, R., and de Wagter, C., "Flow visualization in the wake of flapping-wing MAV 'DelFly II' in forward flight," in "30th AIAA Applied Aerodynamics Conference," New Orleans, Louisiana, 2012.
[30] Caetano, J., Armanini, S., de Visser, C., de Croon, G., and Mulder, M., "Data-Informed Quasi-Steady Aerodynamic Model of a Clap-and-Fling Flapping Wing MAV," in "International Conference on Intelligent Unmanned Systems," Bali, Indonesia, 2015.
[31] Caetano, J., Percin, M., de Visser, C., van Oudheusden, B., de Croon, G., de Wagter, C., Remes, B., and Mulder, M., "Tethered vs. Free Flight Force Determination of the DelFly II Flapping Wing Micro Air Vehicle," in "2014 International Conference on Unmanned Aircraft Systems (ICUAS), Orlando, FL, USA," , 2014, pp. 942–948.
[32] Rose, C. and Fearing, R., "Comparison of Ornithopter Wind Tunnel Force Measurements with Free Flight," in "2014 IEEE International Conference on Robotics & Automation (ICRA)," Hong Kong, China, 2014.
[33] Armanini, S., de Visser, C., and de Croon, G., "Black-box LTI modeling of flapping-wing micro aerial vehicle dynamics," in "AIAA Atmospheric Flight Mechanics Conference," Kissimmee, Florida, 2015.
[34] Armanini, S., Caetano, J., de Visser, C., de Croon, G., and Mulder, M., "Aerodynamic Model Identification of a Clap-and-Fling Flapping-Wing MAV: a Comparison between Quasi-Steady and Black-Box Approaches," in "AIAA Atmospheric Flight Mechanics Conference," San Diego, California, USA, 2016.
[35] Ljung, L., *System Identification: Theory for the User*, Pearson Education (US), 2nd ed., 1998.
[36] Muijres, F., Spedding, G., Winter, Y., and Hedenström, A., "Actuator disk model and span efficiency of flapping flight in bats based on time-resolved PIV measurements," *Experiments in Fluids*, Vol. 51, 2011, pp. 511–525.

Part II

Preliminary Thesis Report

Glossary

List of Acronyms

AoA	Angle of Attack
AR	Aspect Ratio
CFD	Computational Fluid Dynamics
CG	Center of Gravity
DARPA	Defense Advanced Research Projects Agency
DOF	Degrees of Freedom
EKF	Extended Kalman Filter
FBD	Free Body Diagram
FWMAV	Flapping-Wing Micro Aerial Vehicles
IMU	Inertial Measurement Unit
LEV	Leading Edge Vortex
LTI	Linear Time-Invariant
MLE	Maximum Likelihood Estimator
OLS	Ordinary Least Squares
PCC	Pearsons' Correlation Coefficient
PIV	Particle Image Velocimetry
TU Delft	Delft University of Technology

List of Symbols

Greek Symbols

α	Angle of attack (deg)
β	Sideslip angle (deg)
δ_e	Elevator deflection (deg)
δ_f	Flapping frequency (Hz)
Γ	Circulation $(m^2 s^{-1})$
ω	Base frequency for Fourier series model $(rad\ s^{-1})$
ρ	Density (kgm^{-3})
θ	Pitch angle (deg)

Latin Symbols

A_d	Actuator disk area (m^2)
b	Wing thickness (m)
b_w	Span width of the flapping wings (m)
c	Chord length (m)
C_{D_t}	Translational drag coefficient (-)
c_{eff}	Peeled chord length (m)
C_F	Fling coefficient (-)
C_{L_t}	Translational lift coeffcient (-)
C_r	Rotational force coefficient (-)
g	Gravitational acceleration (ms^{-2})
L	Lift force (N)
m	Mass (kg)
M_{wing}	Mass of a single wing (kg)
R	Wing span of a single wing (m)
r	Span-wise position (m)
T	Flapping period (s)
t	Time (s)
t^*	Dimensionless time
V	Velocity (m/s)
V_∞	Free-stream velocity (ms^{-1})
V_i	Induced velocity (ms^{-1})

Subscripts

$_b$	Body-fixed reference frame
$_h$	Horizontal stabiliser
$_r$	Rotational coefficient
$_w$	Wing

Chapter 1

Introduction

For many years researchers have been fascinated by the aerodynamic performance of insects. Insects show extremely high manoeuvrability and agility that cannot be explained by classical aerodynamic theory [1]. Ellington thoroughly studied the aerodynamics of insect flight on a theoretical basis [2]. More recently valuable insight into insect aerodynamics has been gained by force measurements on dynamically scaled robotic wings, establishing empirical relationships for lift and drag [3, 4]. The unsteady effects that lie at the root of flapping flight are still an active field of research today, see reviews by Taha et al. [5] and Chin and Lentink [6], though the focus shifts more and more towards studies involving full-scale robotic flappers [7, 8, 9].

Due to the high aerodynamic performance and wide range of flight envelopes insects have been an inspiration for Flapping-Wing Micro Aerial Vehicles (FWMAV) for over a decade [10, 1]. FWMAVs have matured to a technological level which enables the study of flapping-wing aerodynamics using in-flight measurements. However, there are still many gaps to be filled in the understanding of the unsteady aerodynamic mechanisms associated with flapping flight in both insects and vertebrates.

Chin and Lentink shows a clear overview of the mechanisms in flapping flight and to what extent they have been studied, see Figure 1-1. Especially the effect of tails and the effect of wing-wake interactions lack proper study. Such gaps in understanding slow down development of truly miniature FWMAVs, especially in the framework of predicting dynamic behaviour over the full flight envelope and applying this to on-board control strategies [11].

The aim for many FWMAVs is to achieve fly-sized robots, inspired by nature, capable of autonomously exploring environments too small or dangerous for humans to enter [12, 13]. De Croon et al. describe two main approaches in the development of ever smaller FWMAVS: bottom-up and top-down [13].

The bottom-up approach focuses on developing the tiny individual components which, when assembled, form a miniature robotic insect [13]. Examples of the bottom-up approach are the Harvard RoboBee, see Figure 1-2c, a 60mg robotic insect which can take off vertically but is powered externally [12, 9] and the Nano Hummingbird, a flapping-wing MAV inspired by

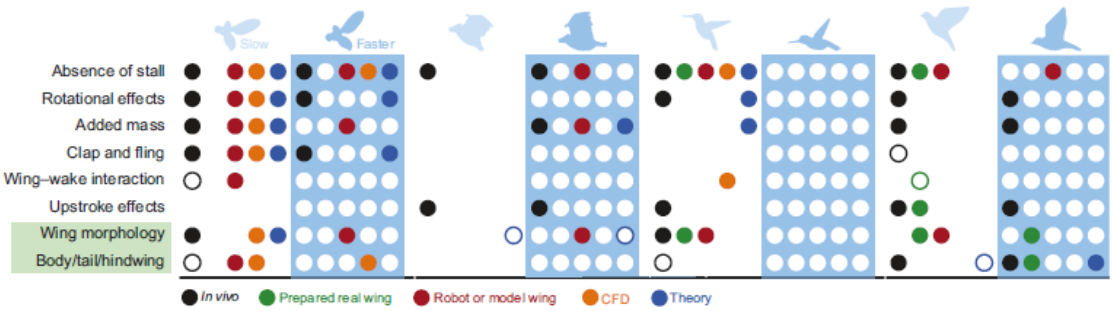

Figure 1-1: Gaps in the understanding of aerodynamic mechanisms across insects and vertebrates, according to Chin and Lentink. Rows indicate seven aerodynamic mechanisms associated with animal flapping flight. Columns indicate categories of flying animals: insects, bats, hummingbirds and other birds; white columns indicate slow flight while blue columns indicate faster flight. Open circles are qualitative studies, filled circles are quantitative. Figure taken from Chin and Lentink [6].

its biological namesake, developed by AeroVironment as part of a research program by the Defense Advanced Research Projects Agency (DARPA), see Figure 1-2d [14].

In the top-down approach, applied at Delft University of Technology (TU Delft), the starting point is a larger but functional MAV [10, 13]. A fully operational platform can help to gain insight into physical phenomena from actual flight data. This knowledge in turn contributes to the development of smaller FWMAVs [13].

1-1 Motivation for the research

For this study the DelFly II is the available FWMAV platform, see Figure 1-2a. Development of the DelFly started as a student project at the faculty of Aerospace Engineering at TU Delft. The current version, the DelFly II, has a wing span of 28cm and can be equipped with an on-board camera and an autopilot containing an Inertial Measurement Unit (IMU). For a full report on the development of the DelFly platform refer to [7].

The DelFly II features a tail for passive stability and to provide conventional control surfaces. The tail design is based on experience with piloted free-flight and trial and error; a thorough study of the effect of the tail or of the wing-tail interactions has not been performed [7]. The result is that the effect of the tail on the dynamics is not well understood.

Currently most FWMAV designs use a tail to ensure passive stability [7], see Figure 1-2a and Figure 1-2b, and to provide an easy means of control. A tail removes the need for complicated active wing control such that development can focus on higher level tasks such as autonomous navigation [13, 16]. However, active wing control for the DelFly is an active field of research at the TU Delft in order to achieve truly miniature MAVs in the future. The Harvard RoboBee [12, 9], Figure 1-2c, and the Nano Hummingbird [14], Figure 1-2d, are one of the few FWMAVs in which controlled, tailless flight has been achieved. The Harvard RoboBee is not yet capable of carrying an on-board power supply and relies on a tether though [12].

(a) TU Delft DelFly II

(b) Ornithopter used by Grauer et al. [15]

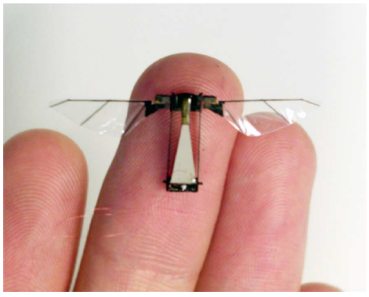

(c) Harvard RoboBee [12]

(d) AeroVironment Nano Hummingbird [14]

Figure 1-2: Examples of FWMAV designs being used today.

A tailless DelFly platform, which can be stabilised using feedback loops, has very recently been developed. However, a better understanding of the tail still provides valuable insights that can be used to support the development of a tailless variation of the DelFly. Having models explicitly including the tail could also allow the design of DelFly configurations for specific missions in which having a tail is beneficial. An example could be a long-range flight in which passive stability helps to reduce energy consumption.

Current FWMAV models found in literature often do not account for tail effects explicitly due to the extremely complicated interactions between the flapping wings and the tail. These interactions are most often neglected (see Grauer [17]) or, as is the case for the DelFly II, modelled implicitly [16, 18].

The three main categories of models currently applied to MAVs are unsteady, quasi-steady or linearised models [8, 16]. One can distinguish between time-resolved models, looking at the force development within a single flapping cycle, or time-averaged models, averaging the forces over each flapping cycle and analysing the dynamics of the whole system.

System identification can be a solution to model the complicated unsteady aerodynamic interaction between the flapping wings and the tail. System identification can be used to model any dynamic system by observing the response of that system to a known input; the designer has great freedom in the choice of model structure and is not required to have a priori knowledge of the system [19]. A big advantage of system identification for FWMAVs is that models are obtained with data acquired from the real system and can be validated using actual flight data.

The application of system identification to full-scale FWMAVs is an active field of study and the quality of the data that can be obtained from free-flight has drastically improved during the last few years [16, 20, 15, 8].

1-2 Research objective

The aim of the proposed research is to increase the understanding of the effect of the tail on the overall dynamics of the DelFly II FWMAV. Furthermore, modelling the effect of the tail may lead to valuable analysis tools which can help to design DelFly configurations tailored to specific mission requirements.

The aim is to model the tail effects using models that are both physically insightful as well as able to predict dynamic stability characteristics. To be useful for design purposes, and ultimately on-board control applications, the models should thus be relatively simple.

Since the issue of dynamic stability is relevant for the full MAV system, on a larger time-scale, this calls for a study of the time-averaged dynamics. Studying only time-averaged dynamics does come at the cost of less insight into any possible effects of the tail on the complex aerodynamics occurring within a single flapping cycle.

The previously described context leads to the formulation of the research objective:

To improve the understanding of the effect of tail geometry and position on the time-averaged dynamics of the DelFly II by applying system identification techniques.

The following research questions further specify the scope of the work and should be answered in order to achieve the research objective:

1. How does the **(x)** of the horizontal (vertical) stabiliser affect the longitudinal (lateral) dynamics of the DelFly II?
   (a) Surface area (S);
   (b) Aspect ratio (AR), defined as b^2/S with b the maximum span width of the tail;
   (c) Longitudinal position with respect to the flapping wings
2. To what extent can the models identified in this study be extrapolated to other tail geometries in order to be used for configuration design?

The scope of the thesis will thus be limited to the three parameters specified in the first three research questions.

This study focuses on the horizontal stabiliser of the tail and its effect on longitudinal dynamics; thereby assuming no coupling between longitudinal and lateral motion. The effect of the vertical stabiliser will be studied only if time permits and after the horizontal stabiliser has been studied.

1-3 Thesis outline

The work of this thesis is split into two phases: the preliminary phase and the main thesis phase. A roadmap of the thesis work is illustrated in Figure 1-3.

During the preliminary phase, a thorough literature review is performed and candidate model structures to model the tail are determined. The literature review will thus focus on modelling of flapping-wing flight to find potentially suitable approaches for the current study.

Initial tail configuration design also takes place during the preliminary phase of the thesis. Solutions are suggested to efficiently construct multiple tail geometries for testing.

An experimental approach is taken during this thesis because of the highly complicated nature of the interactions between the main wing and the tail and the currently limited knowledge of tail effects. Thus suitable experiments will be identified and prepared during the preliminary phase of this thesis.

Testing and data analysis shall be the bulk of the main thesis phase. Both wind tunnel and free-flight tests shall be carried out in order to assess the individual tail contribution to the generation of forces and moments and to study the effect of the tail on the total dynamic behaviour of the platform, respectively. Results from these tests will likely lead to iterations in tail configurations, experiment design or even in model structure; testing is expected to provide new insights.

Model identification and validation shall be performed in the final part of the thesis, once enough data is available, using the modelling approach determined in the preliminary thesis phase. Analysis and validation of the identified models could potentially call for additional study into different model structures or even require a different approach.

1-4 Report structure

This report describes the work achieved during the preliminary phase of the thesis. Its main goal is to present the literature review and to communicate the methodology of the research. The literature review is discussed first in Chapter 2, concluding with a synthesis which discusses the connection between the found literature and the current work. The report continues with an analysis of the involved forces and moments and the proposed approach to model the DelFly tail in Chapter 3. Following that, Chapter 4 discusses the proposed research methodology. This includes the intended experiments and a description of the platform used to conduct the experiments. Chapter 4 concludes with hypotheses of the expected findings. Finally, conclusions and recommendations are discussed in Chapter 5.

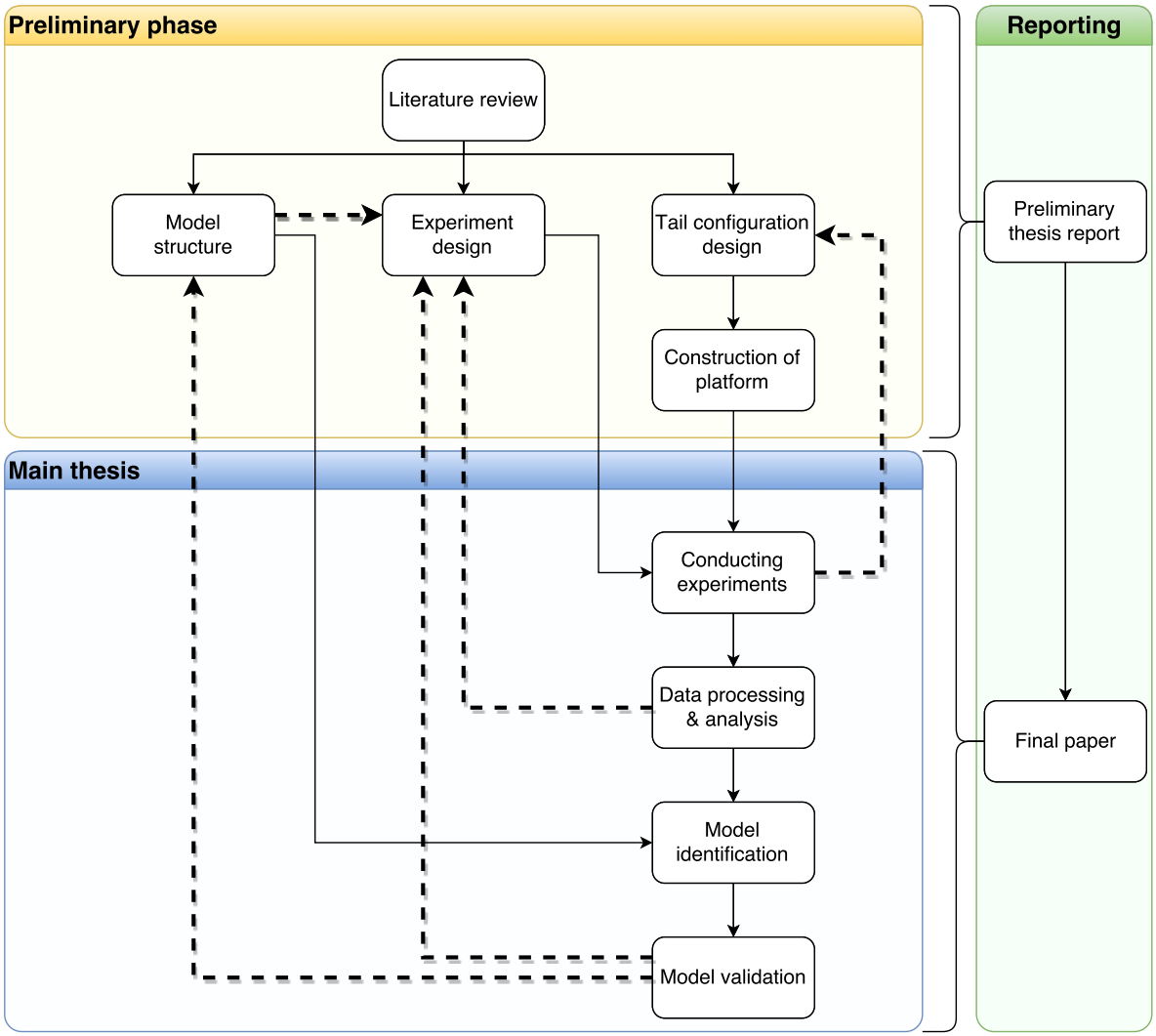

Figure 1-3: Flow diagram indicating the activities taken during the thesis. Arrows indicate how the different activities relate. Dashed arrows represent potential iterations in the research.

Chapter 2

Literature review

This chapter presents a review of the state-of-the-art in the field of flapping-wing aerodynamics and in particular modelling of such flight. The aerodynamic phenomena are discussed in Section 2-1, followed by a review on modelling approaches in Section 2-2. Section 2-3 is dedicated to literature on tail effects and models. The current status of system identification applied to FWMAVs is discussed in Section 2-4. The chapter is concluded by a brief synthesis of the discussed literature in Section 2-5.

2-1 Aerodynamics of flapping flight

Development of FWMAVs is greatly inspired by insect flight. Subjected to millions of years of evolution, insects demonstrate impressive aerodynamic performance that is unsurpassed by any man-made device. Their flight capabilities cannot be readily explained by classical aerodynamic theory [1]. This section aims to introduce the most important aspects of insect flight or, more generally, flapping-wing flight. The important force generation mechanisms are discussed.

The wing motion of insects is characterized by a translational and a rotational phase. The terminology is visualised in Figure 2-1. The translational phases are termed upstroke and downstroke. Rotation occurs during the transitions between up- and downstroke. The rotation during transition from down- to upstroke is termed supination. The rotation which occurs during the transition from up- to downstroke is called pronation [1].

As the aerodynamic performance of insects and many birds cannot be explained by steady aerodynamic theory many studies are devoted to explaining the unsteady mechanisms leading to the enhancement of lift. Five key aerodynamic force generation mechanisms have been identified in the literature: (1) Delayed stall (or absence of stall); (2) clap-and-fling; (3) wing-wake interactions; (4) rotational circulation (Kramer effect) and (5) added mass effects [1, 6]. Another mechanism described in the review by Sane is the Wagner effect [1]. These phenomena will be briefly discussed in this section.

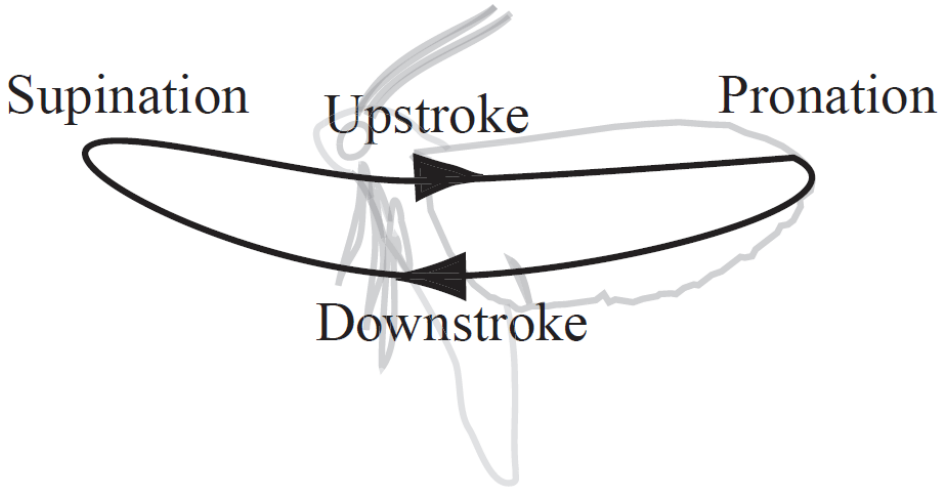

Figure 2-1: Conventions and terminology used to characterise insect wing motion. Figure adapted from Sane [1].

Wagner effect

One of the unsteady effects observed in flapping flight is the so-called Wagner effect. Sane describes the Wagner effect as a latency in the build up of circulation; meaning that some finite time is required before the Kutta condition is established [1]. The Kutta condition is the condition in which the flow over both the top and the bottom of an airfoil leave the trailing edge smoothly; refer to Anderson for a detailed explanation [21]. Unlike the other unsteady mechanisms the Wagner effect actually attenuates lift forces [1]. However, a study by Dickinson and Götz has shown that the Wagner effect is quite small for the Reynolds numbers typical in insect flight [22]. Therefore the Wagner effect is neglected in most aerodynamic models of insect flight [1].

Delayed stall (Leading Edge Vortex)

Insects and birds often translate their wings at very high Angle of Attack (AoA), leading to flow separation at the leading edge. Normally the flow reattaches before the trailing edge; the flow rolled up between the leading edge and the reattachment point is called the Leading Edge Vortex (LEV) [6].

In a purely translating wing the LEV keeps growing until the separation point is driven behind the trailing edge and flow reattachment is no longer possible. At this moment the lift production of the wing decreases drastically; the wing is said to have stalled [1].

The flapping motion of insect or bird wings stabilises the LEV by generation of a span-wise flow from wing root to approximately three quarters of the span, see Figure 2-2, keeping the LEV attached to the wing [1, 3]. The axial flow is generated by centripetal and Coriolis accelerations [6]. Insects are thus able to translate their wings at very high AoA without ever stalling, leading to a substantial increase in lift production during the translational phase of the wing stroke.

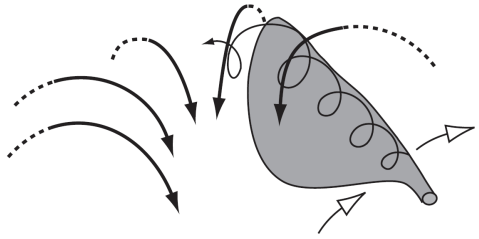

Figure 2-2: Stable attachment of the LEV. Axial flow spirals towards the tip due to a span-wise velocity gradient interacting with the LEV. The axial flow keeps the LEV attached by transporting momentum out of the vortex. Thick black arrows indicate downwash generated due to the vortex system. Figure taken from Sane [1].

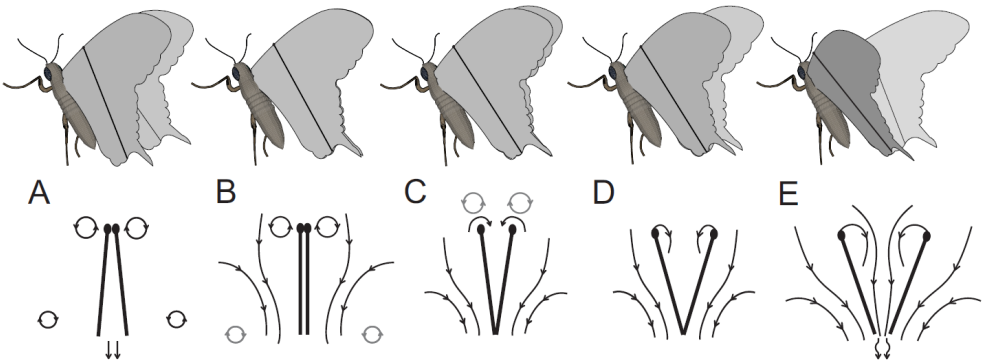

Figure 2-3: Schematic of the clap-and-fling mechanism. Arrows represent direction of flow; circular shapes indicate vortices, detached lines show the flow streamlines. Gray lines indicate vorticity of the previous subfigure. Figure taken from Armanini et al. [24].

Clap-and-fling

Some insects clap their wings together at the end of the upstroke, Figure 2-3 (A). During the clap air is pushed out from between the wings which provides thrust to the insect [1]. The wings start touching at the leading edge and then clap together in (B). The wings will then pronate and rotate about the trailing edge, 'flinging' apart. During this phase, air rushes into a low pressure area between the wings, Figure 2-3 (C, D). The air rushing in assists the build-up of circulation or attached vorticity [1]. This was observed as an augmented LEV by Percin et al. [23]. As the flap continues the augmented LEV continues to grow and a starting trailing vortex forms and interacts with the flow leaving the cleft (E) [24].

Clap-and-fling increases lift and thrust production but the mechanism is not observed in all insects; some researchers believe that clap-and-fling is actually a result of the insect trying to increase lift by maximising stroke amplitude [1].

Due to the X-wing design clap-and-fling also occurs in the DelFly II FWMAV; this leads to an increase in thrust of roughly 8% [13]. Percin et al. have performed a study on the effects of wing flexibility on clap-and-fling, using the wing planform of the DelFly, concluding that lift generation benefits from increased wing flexibility [23].

Rotational circulation (Kramer effect)

Insects rapidly rotate their wings at the end of the translational phase. Rotation ensures a positive AoA during both up- and downstroke, maintaining lift generation [1]. A study into the most energy efficient kinematics of insect wings by Berman and Wang showed that insects rotate their wings to such extent that one edge of the wing leads the motion in both up- and downstroke [25].

Due to wing rotation occurring simultaneously with translation the flow around the wing does not adhere to the Kutta condition anymore. The wing then generates additional circulation in order to re-establish smooth flow conditions at the trailing edge. The generated circulation is proportional to the angular velocity of the wing rotation [1].

The effect of the additional circulation on lift production depends on the timing of the rotation. Advanced rotation, rotation before stroke reversal, increases lift. Delayed rotation, wing rotation after stroke reversal, has the opposite effect. Symmetric rotation, when the wing rotates during stroke reversal, yields a positive lift peak right before stroke reversal and a negative peak right after stroke reversal [3].

Dickinson et al. determined that rotational effects are quite significant and contribute up to 35% of the lift in robotic model fruit flies during hover [3]. It is assumed that these results apply to low-speed forward flight as long as the mean wing tip velocity is far greater than the forward velocity [26].

Wing-wake interaction (wake capture)

Insect wings possibly interact with the vorticity of previous strokes during flapping [1]. This phenomenon, often called *wake capture*, was studied in detail by Birch and Dickinson [27]. They find differences in force production at the beginning of a stroke for a wing starting from rest compared to a wing which has already flapped a few cycles. These differences are attributed to wing-wake interaction [27]. A hypothesis for wing-wake interaction is illustrated in Figure 2-4.

As the wing starts stroke reversal, both the LEV and the trailing edge vortex are shed. Upon changing the translational direction the wing will encounter strong velocity and acceleration fields caused by the shed vortices. This results in higher aerodynamic forces immediately after stroke reversal [1]. See also sub-figures D and E in Figure 2-4.

Birch and Dickinson describe wake capture as a truly unsteady phenomenon which is inherently time-variant [27]. At the moment, physical models of flapping flight do not account for wing-wake interaction due to its complexity [4, 24].

Added mass

Added mass forces, also called added inertia, arise from wing accelerations when starting motion from rest and during stroke reversal. Added mass force stems from the reaction force of the fluid surrounding the wing during acceleration. This effect is difficult to isolate in measurements because it occurs during the same phase of the motion as the Kramer effect and wake capture [1].

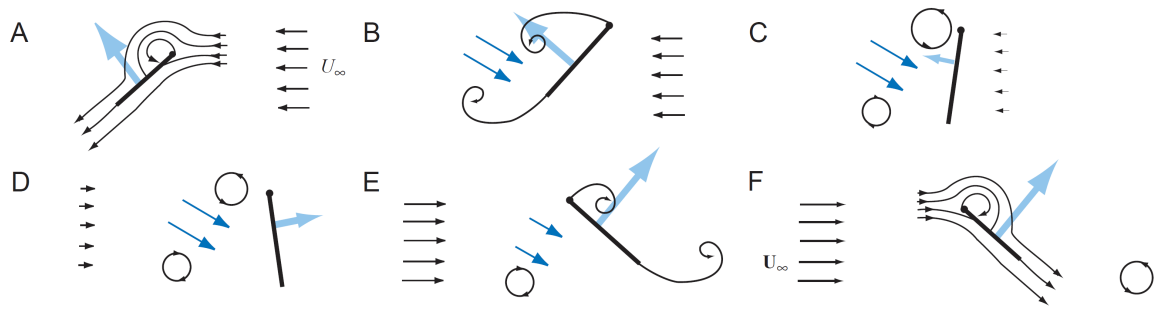

Figure 2-4: Wing wake-interaction. Parts A-F illustrate cross-section of a wing during stroke reversal. Vorticity is generated when rotation starts in (B), resulting in a strong velocity field (dark blue arrows) in the intervening region (C, D). Upon stroke reversal (D, E) the wing encounters this velocity field, increasing lift. Light blue arrows indicate aerodynamic force. Figure adapted from Sane [1].

2-2 Modelling flapping flight

Aerodynamic models used for dynamics and control can be classified as either unsteady or quasi-steady, according to Taha et al. [5]. Most unsteady models are black-box, mathematical models; quasi-steady models are based on aerodynamic principles but rely on empirical data to determine model parameters [6]. More recently linearised models were used to identify platform-specific FWMAV models [16, 15, 20]. To lesser extent, actuator disk theory has also been applied to predict the lift of birds, insects and bats [28, 29].

Models of insect wings have also been developed using Computational Fluid Dynamics (CFD), see for example Sun and Wu [30]. Due to the high computation load CFD models are not suitable for dynamics and control applications; as such these are not discussed in this literature study. The other modelling approaches will be described in more detail in this section.

2-2-1 Unsteady models

Unsteady models are often based on Fourier series [5]. In principle the unsteady forces within a flapping cycle can be approximated perfectly by a Fourier series given the inclusion of a sufficient number of harmonics. Any force can then be described by the relation in Equation (2-1) [5],

$$P_{ref}(t) = \sum_{n=1}^{N} \left(a_n \cos\left(n\omega t\right) + b_n \sin\left(n\omega t\right)\right) \tag{2-1}$$

where N denotes the total number of harmonics which are accounted for by the model. ω is a base frequency chosen by the designer of the model; often the flapping frequency is used.

Fourier series models can approximate observed forces extremely accurately since it is a true nonlinear periodic approximation [5]. The lack of assumptions regarding the physics of the system enables capturing all the unsteady phenomena [11]. However, a model identified using this structure cannot be generalised to other wing shapes, kinematics and platforms or even to other flight conditions [5, 11]. Another drawback is that the model parameters ($a_{0,\ldots,N}$ and $b_{0,\ldots,N}$) are purely mathematical. Relevant insight cannot be gained since the model has no physical link to the system [11].

Unsteady models based on Fourier series are not considered to be appropriate for this study due to the low level of understanding offered by this model structure.

2-2-2 Quasi-steady models

The most widely used approach in modelling flapping flight is the quasi-steady model. These models can capture time-resolved forces and are based on aerodynamic principles.

The approach assumes that the instantaneous aerodynamic forces acting on the flapping wing are equal to those acting on a steady wing with the same instantaneous velocity and AoA [2]. This implies that variation in the forces are time dependent only because of the changing kinematics and not due to time dependence of the fluid flow [1]. Most quasi-steady models apply blade element theory, computing the forces acting on each blade element of the wing individually and integrating over the wing span to obtain the total forces [6].

At the moment, quasi-steady models do not capture wing-wake interaction due to its inherent time-variancy [27]. The Wagner effect is also commonly not included in the quasi-steady models found in literature because of its limited effect at the Reynolds numbers at which insects and flapping-wing MAVs operate [1, 24]. These two phenomena are thus not discussed here.

This section discusses the implementation of the aerodynamic mechanisms, discussed in Section 2-1, into quasi-steady models.

Translational forces (Leading Edge Vortex)

The translational forces acting on a flapping wing have been thoroughly studied in insect flight, see for example Dickinson et al. [3] and Sane and Dickinson [4]. In most quasi-steady models the translational contribution is modelled by Equation (2-2) ([6], using a slightly different notation for consistency in this thesis),

$$\begin{aligned} F_{L_t} &= \int_0^R \frac{1}{2}\rho c(r) V^2 C_{L_t}(\alpha)\mathrm{d}r \\ F_{D_t} &= \int_0^R \frac{1}{2}\rho c(r) V^2 C_{D_t}(\alpha)\mathrm{d}r \end{aligned} \tag{2-2}$$

in which R denotes the wing span of a single wing, ρ the density of the medium, V the magnitude of the velocity of the local blade element, $c(r)$ the chord length of the blade element at span-wise position r and C_{L_t} and C_{D_t} are the non-dimensional translational lift and drag coefficients, respectively. α denotes the AoA of the respective blade element.

A widely adopted empirical relationship for the translational lift and drag coefficients, as a function of wing AoA, was found by Dickinson et al. [3], see Equation (2-3).

$$\begin{aligned} C_{L_t} &= 0.225 + 1.58\sin\left(2.13\alpha - 7.20\right) \\ C_{D_t} &= 1.92 - 1.55\cos\left(2.04\alpha - 9.82\right) \end{aligned} \tag{2-3}$$

Berman and Wang apply a slightly simpler relation for the lift coefficient, see Equation (2-4) [25],

$$C_{L_t} = C_T \sin 2\alpha \tag{2-4}$$

where C_T is the slope to be determined experimentally. The relationship in Equation (2-4) has also been applied to model the dynamics of the DelFly II [31, 24].

Rotational circulation (Kramer effect)

The formulation of the rotational circulation in quasi-steady models is similar to that of the translational force component. The rotational force acting on the wing can be modelled using Equation (2-5), using the notation from Armanini et al. [24],

$$F_R = \frac{1}{2}\rho C_R c^2(r)\dot{\theta}_w V \tag{2-5}$$

with $\dot{\theta}_w$ the pitch rate of the blade element and C_R the rotational lift coefficient. The most widely adopted formulation for the rotational lift coefficient is the one proposed by Sane and Dickinson [4], Equation (2-6).

$$C_R = \pi(0.75 - x_0) \tag{2-6}$$

x_0 denotes the chord-wise position of the axis of rotation of the wing. The slope π is a theoretical value which does not always hold in practice. The slope is often generalised to a parameter, C_r, which is estimated based on experimental measurements for a specific wing geometery and kinematic pattern [31, 24].

Added mass

The added mass inertia is difficult to model since it is a function of acceleration of the fluid relative to the wing, the rotational acceleration due to wing rotation and also contains cross-terms due to translational velocity [1]. Most quasi-steady models implement added mass using a time-invariant coefficient; time-variancy is implicit variation in wing acceleration [1]. Armanini et al. use a thin plate approximation for the wings, yielding Equation (2-7) [24],

$$\mathrm{d}\boldsymbol{F}_a = -\begin{bmatrix} \frac{1}{4}\pi\rho b^2 a_{x,w} \\ \frac{1}{4}\pi\rho c_{eff}^2(r) a_{z,w} \end{bmatrix} \mathrm{d}r \tag{2-7}$$

where b denotes the thickness of the wing and c_{eff} is the peeled chord length of the wing, taking into account wing flexibility [24]. Apart from the inclusion of wing flexibility, Berman and Wang [25] and Sane and Dickinson [4] use similar added mass terms in their quasi-steady models.

Viscous effects

Viscous effects are not specifically mentioned in Section 2-1 but are discussed here since some quasi-steady aerodynamic models in the literature incorporate the term. In these models the viscous effects are often modelled as a drag force, essentially replacing the drag term in Equation (2-3). Caetano et al. formulate the viscous term as in Equation (2-8) [31],

$$\boldsymbol{F}^v = \int_0^R \frac{1}{2}\rho c(r)\left[C_D(0)\cos^2\alpha + C_D(\pi/2)\sin^2\alpha\right]|V|\begin{bmatrix} v_{x_w} \\ v_{z_w} \end{bmatrix}\mathrm{d}r \tag{2-8}$$

with $C_D(0)$ and $C_D(\pi/2)$ the drag coefficients at 0 deg and 90 deg AoA, respectively. This approach to add viscosity was first proposed by Berman and Wang [25], and is also adopted by Armanini et al. [24] to their quasi-steady model of the DelFly II.

Clap-and-fling

Clap-and-fling is not commonly included in quasi-steady models found in literature [5]. Armanini et al. do include it in their quasi-steady model applied to the DelFly II, since clap-and-fling is significant in this particular FWMAV [24].

Armanini et al. formulate the hypothesis that, in case of flexible wings such as those of DelFly II, clap-and-fling is dominated by translation and rotation of the wings about the leading edge. The mechanism is also rephrased as clap-and-peel since the flexible wings do not fling apart over the full chord length at once, as is the case with rigid wings, but rather peel apart gradually.

The clap-and-peel mechanism is modelled by adapting the equations for translational and rotational circulation (Equation (2-2) and Equation (2-5)) to a piece-wise function, see Equation (2-9) [24],

$$\Gamma = \begin{cases} \frac{1}{2}C_L c(r)|V| + \frac{1}{2}C_F c^2(r)\dot{\theta}_{fling} & \text{if} \quad t^* \geq 0 \quad \text{and} \quad \dot{\theta}_{fling} \geq 0 \\ \frac{1}{2}C_L c(r)|V| + \frac{1}{2}C_R c^2(r)\dot{\theta}_w & \text{otherwise} \end{cases} \tag{2-9}$$

with C_F the fling coefficient which is estimated through free-flight data. $t^* = t\ /T$ is the dimensionless time within a flapping cycle (with flapping period T. $\dot{\theta}_{fling} = -\dot{\theta}_w$ is the fling rate; it is modelled as the negative of the wing pitch rate. Equation (2-9) essentially replaces the standard rotational circulation in the part of the flapping cycle during which the wings are peeling apart. When the peeling phase is over ($\dot{\theta}_{fling} = 0$), the second part of Equation (2-9) holds and the normal rotational circulation coefficient is valid.

2-2-3 Linearised time-invariant models

The time-averaged dynamics of the DelFly II have been successfully approximated using linearised models similar to those used for fixed-wing aircraft [16, 18, 20]. Such models are easy to use and can be estimated well from free-flight data. Linearised models provide an easy tool for simulation, to analyse stability characteristics of a certain platform and to use for the design of control algorithms. A disadvantage of the Linear Time-Invariant (LTI) models used in the literature is that the parameters have less physical connection to the system than those of the quasi-steady model. This makes interpretation of a change in model parameters slightly more difficult.

The approach was also used by Grauer et al. to model the aerodynamics of their ornithopter, see Figure 1-2b [15]. They use step-wise regression to determine an appropriate model structure for the longitudinal aerodynamics leading to a model structure based on the velocity of the ornithopter, its pitching rate and on its wing velocity (i.e. flapping frequency). Such a simple model structure is also typically encountered in fixed-wing aircraft models; for details please refer to Grauer et al. [32].

Caetano et al. have been the first to attempt system identification of the DelFly II using a linearised model. Two model structures are applied: a full model which represents the full 6 Degrees of Freedom (DOF) forces and moments as a linear function of the states and a reduced model structure which contains only states that are measurable on-board. The

resulting models approximate the forces in a flapping cycle quite well but still yielded unstable simulation results [16].

Good results for the DelFly II, also in simulation, have been found by Armanini et al. by using a time-varying model. This model consists of two parts: an LTI part and an unsteady (Fourier series) part. The different data sets are generated by filtering the data with different cut-off frequencies to separate low-frequency and high-frequency content. This model assumes time scale separation to hold, i.e. that no coupling exists between the time-resolved and the time-averaged dynamics if the flapping frequency is high enough [20].

The LTI models used by Armanini et al. are decoupled for the longitudinal and lateral dynamics and contain frequently used flight dynamics states, see Equation (2-10) for the longitudinal model [20]. The lateral model is similar.

$$\begin{bmatrix} \Delta\dot{q} \\ \Delta\dot{u} \\ \Delta\dot{w} \\ \Delta\dot{\theta} \end{bmatrix} = \begin{bmatrix} \frac{M_q}{I_{yy}} & \frac{M_u}{I_{yy}} & \frac{M_w}{I_{yy}} & 0 \\ \frac{X_q}{m} - w_0 & \frac{X_u}{m} & \frac{X_w}{m} & -g\cos\theta_0 \\ \frac{Z_q}{m} + u_0 & \frac{Z_u}{m} & \frac{Z_w}{m} & -g\sin\theta_0 \\ 1 & 0 & 0 & 0 \end{bmatrix} \begin{bmatrix} \Delta q \\ \Delta u \\ \Delta w \\ \Delta\theta \end{bmatrix} + \begin{bmatrix} \frac{M_{\delta_e}}{I_{yy}} \\ \frac{X_{\delta_e}}{m} \\ \frac{Z_{\delta_e}}{m} \\ 0 \end{bmatrix} \Delta\delta_e \tag{2-10}$$

Using this model with its identified parameters shows quite good agreement with the time-averaged content of the flight-test data. Linear addition of a Fourier series model of the form of Equation (2-1) allows the model to also capture the time-resolved content of the measured data quite well [20].

The parameters of the LTI model in Equation (2-10) can be interpreted physically to some extent. Changes in pitch moment damping for example, seen in M_q, can be linked to physical changes of the system [20].

The linearised model structure has also been applied with no prior assumptions on the parameters, fitting the models based solely on input-output relations, creating fully black-box LTI models. The drawback being that physical phenomena might be captured by other parameters than expected since the model parameters contain no direct physical link to the system [18].

2-2-4 Actuator disk models

Actuator disk theory is commonly used to predict the forces and power requirements of helicopters. The theory has also been applied to predict lift forces for animals. Sane developed a model based on rotor theory to estimate induced flow over the body of insects [28]. More recently Shkarayev and Silin applied actuator disk theory to predict the thrust forces on model bird wings [33]. Muijres et al. use time-resolved Particle Image Velocimetry (PIV) measurements to estimate the induced velocity in the wake of the wings of two species of bats and use this as input to their modified actuator disk model [29].

Figure 2-5 illustrates the actuator disk model applied to bird flight. If the induced velocity is assumed constant over the actuator disk area and thrust is assumed small, then Equation (2-11) holds [6].

$$F \approx L = -2\rho A_d w^2 \tag{2-11}$$

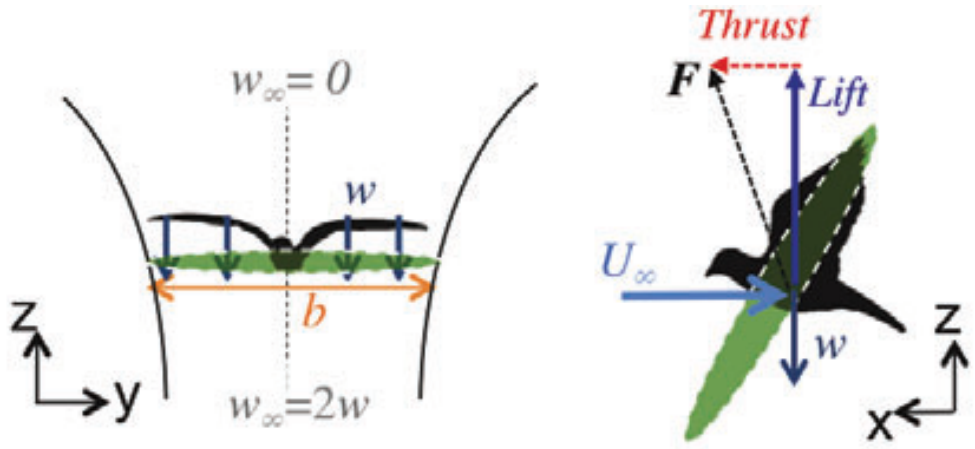

Figure 2-5: Actuator disk model estimates lift based on the mass flux through the stroke plane area A_d, represented by the green shaded area. U_∞ is the free-stream velocity and w the velocity induced by the flapping wings. Figure taken from Chin and Lentink [6].

This model is much simpler than the quasi-steady models based on aerodynamic principles; it is however subject to some limitations. Thrust cannot be predicted using Equation (2-11). Also, using this actuator disk model it is not possible to estimate the force development within a single flap cycle [29].

Muijres et al. modified the actuator disk model in their study to work with a span-wise varying induced velocity. Their model uses an area for the actuator disk which is based on the wake area generated by the wings. The wake area is estimated using PIV measurements. Using their modified actuator disk model they are able to estimate the variation in lift coefficient within a flap cycle [29].

In a dynamics and control framework the actuator disk model presented here is considered to be oversimplified. To predict dynamic behaviour thrust should also be estimated. It is also quite difficult to extend the actuator disk model to explicitly account for a tail, preventing a proper study of tail effects. Actuator disk models are thus not further considered in this study.

2-3 Including a tail

FWMAVs have a tail for passive stability and to make use of conventional control surfaces for easy controls. This is a feat also encountered in nature; birds manipulate the morphology of their tail during flight for control purposes [34]. However, the aerodynamic effects of birds' or bats' tails have not yet been studied thoroughly (refer back to Figure 1-1 for an overview) [6]. Current tail models for FWMAVs are usually platform specific and simplified, ignoring the effect of the flapping wings [17].

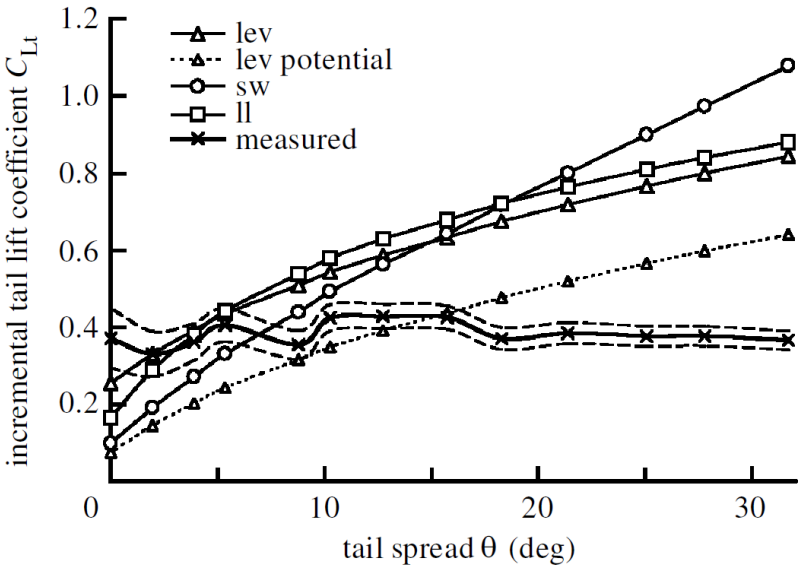

Figure 2-6: Measured and predicted incremental lift coefficients for varying tail spread angle θ for a starling body. $\alpha = 15\,\text{deg}$ for the tail, $V_\infty = 4.9ms^{-1}$. Dashed lines indicate standard deviation of the measured C_{L_t}. *lev* denotes leading edge vortex model (which contains a potential lift and a vortex lift component), *sw* denotes the slender wing (lifting surface) model and *ll* denotes the lifting line model. Figure taken from Maybury et al. [35].

2-3-1 Bird tail aerodynamics

Thomas developed a model of the forces produced by birds' tails using slender lifting surface theory. He arrives at the relationships in Equation (2-12) for the lift and induced drag generated by a bird tail, respectively. His model assumes an elliptical load distribution along the span of the tail surface [34].

$$\begin{aligned} C_l &= \left(\frac{\pi}{2}\right) AR\alpha \\ C_{d_i} &= \frac{C_l^2}{\pi AR} = C_l\left(\frac{\alpha}{2}\right) \end{aligned} \tag{2-12}$$

The study by Thomas focuses primarily on relatively fast forward flight ($\approx 5.0ms^{-1}$) and his model is tailored to flight at relatively low angles of attack. In this regime the freestream velocity is dominant over the flow induced by the flapping wings which leads to fairly constant flow conditions over the tail [34]. It is unlikely that such an assumption is valid for the Delfly II which is usually flown at velocities in the range of $0.5 - 2.0ms^{-1}$ and high angles of attack α, though velocities as high as $8.0ms^{-1}$ can be achieved [11, 31].

Maybury et al. test several models of bird tail aerodynamics, including the model by Thomas [34], using wind tunnel measurements performed on a frozen European starling. Their study indicates that the available models all substantially overestimate the lift generated by the tail. Figure 2-6 illustrates the results, plotting the lift coefficient for varying tail spread angle: a morphological parameter which birds adapt in-flight for control purposes [35].

Figure 2-6 shows that all three methods overestimate the tail lift, especially at higher tail spread angles. Note that the study by Maybury et al. is performed without the wings

flapping and thus considers gliding flight. They conclude that it is not possible to derive a simple prediction of the lift coefficient of a birds' tail based on tail geometry. They also conclude that the tail and body should not be considered in isolation since the interaction between the two plays a large role in the generation of forces and moments [35].

2-3-2 FWMAV tail models

Grauer et al. tested the tail of their ornithopter in a wind tunnel in order to create an aerodynamic model of the tail specifically. They model the tail aerodynamics using a polynomial model based on AoA and sideslip angle (β). The resulting model structure is given in Equation (2-13); a similar model is used for the drag. Grauer et al. assume steady flow over the tail surface and thus ignore the effects of the flapping wings on the forces and moments generated by the tail [32, 17].

$$C_L = C_{L_0} + C_{L_\alpha}\alpha + C_{L_{\alpha\beta}}\alpha\beta + C_{L_{\alpha^3}}\alpha^3 + C_{L_{\alpha^2\beta^2}}\alpha^2\beta^2 \tag{2-13}$$

Currently the tail of the DelFly II has not been modelled explicitly. In the quasi-steady model by Armanini et al. wind tunnel measurements are conducted without the tail attached, focusing on modelling the flapping wings [24]. In the time-varying and black-box models by Armanini et al. ([18, 20]) the tail is captured implicitly.

A 2D numerical study has been performed for a wing-tail configuration based on the DelFly II with two flapping wings upstream of a stationary tail by Tay et al. The study shows that placing a tail in the wake of a flapping wing configuration can actually increase the lift, thrust and propulsive efficiency of the total system. Unfortunately 3D effects are not taken into account in this study. Also, the simulations are performed with a zero degree pitch angle with respect to the free-stream velocity [36]. During slow forward flight the DelFly may actually fly at pitch angles larger than 80 degrees [24]. Because this yields completely different flow conditions at the tail it is difficult to use the results of Tay et al. in this study.

2-3-3 Challenges in modelling the DelFly II tail

Percin et al. performed an aerodynamics study on the DelFly II, visualising the vorticity in the wake of the flapping wings by means of PIV measurements. This study shows that vorticity shed from the flapping wing influences the flow over the tail surface considerably, as might be expected [37]. Figure 2-7 shows some of the results by Percin which give a qualitative indication of the complexity of the flow over the tail. These results confirm that the interaction between the flapping wings and the tail cannot be omitted when studying the effect of the horizontal stabiliser on the dynamics of the DelFly II. However, it is very difficult to accurately model this highly unsteady interaction.

Koopmans et al. studied how to manipulate the location of the aerodynamic center and CG of the DelFly II to achieve passive stability over a large velocity range. In this study they note that achieving electronic stabilisation is challenging since the effectiveness of the tail varies greatly with changing flight conditions. During their work they found that, depending on the conditions, the elevator effectiveness may vary with an order of magnitude or even

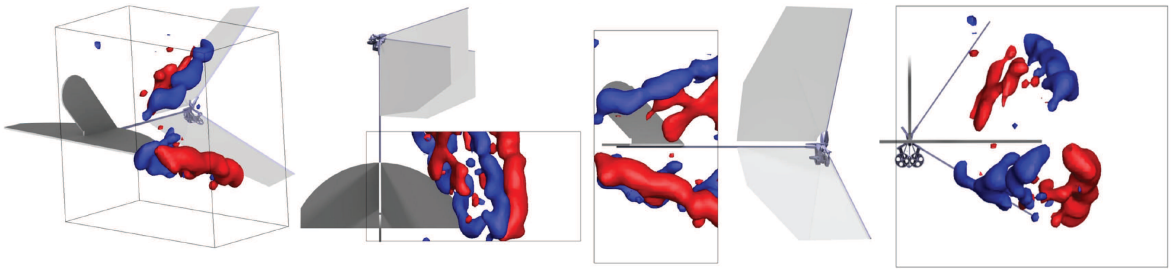

Figure 2-7: Vorticity mapping of the DelFly II. PIV results from wind tunnel experiments. Blue is clockwise vorticity, red is counter-clockwise. Figure adapted from Percin [38].

change sign during flight. It is almost impossible to capture the elevator effectiveness in a single time-invariant parameter which is valid over a large range of flight conditions [39].

Finally, the DelFly II in slow forward flight flies at very high angles of attack. This means the tail is under stall conditions when not considering the effects of the flapping wings [39]. The fact that the control surfaces are actually effective implies that the effective AoA at the tail is considerably lower due to the unsteady airflow generated by the flapping wings. However, this also implies that the local AoA at the tail is time-varying during a flapping cycle making it very challenging to model.

2-4 System identification of FWMAVs

Since some insects have lengths of only a couple of millimeters, performing in vivo measurements is often impossible. The mechanisms involved with force generation in flapping flight, in particular the wing-tail interactions, are also extremely complex; developing accurate theoretical models is extremely difficult [34, 35]. For these reasons system identification plays a major role in the development of FWMAVs and the understanding of insect flight.

According to Ljung system identification consists of three basic entities: (1) the data; (2) a set of candidate models and (3) a rule to assess the quality of each candidate model [19]. Models commonly used in literature have been discussed in Section 2-2. This section focuses on acquisition of system identification data in literature.

One of the first applications of system identification to flapping flight is found in a study by Dickinson et al. [3]. They developed empirical lift and drag equations for insect wings by doing force measurements on a dynamically scaled robotic wing, resulting in Equation (2-3). Somewhat later Sane and Dickinson expanded this empirical model with the inclusion of wing rotation, again using a robotic wing for their measurements [4].

Measurements performed on such robotic wings provide valuable insights into the aerodynamics of flapping flight. At some point, however, researchers desired more realistic experiments. In this light robotic flappers became more and more interesting. These flapping robots can provide in-flight aerodynamic measurements [7]. Currently it is common to test such full-scale FWMAVs in the wind tunnel, and even in free-flight, to directly measure forces and moments and estimate the parameters of any desired aerodynamic model; see for example Caetano et al. [31] or Grauer et al. [15].

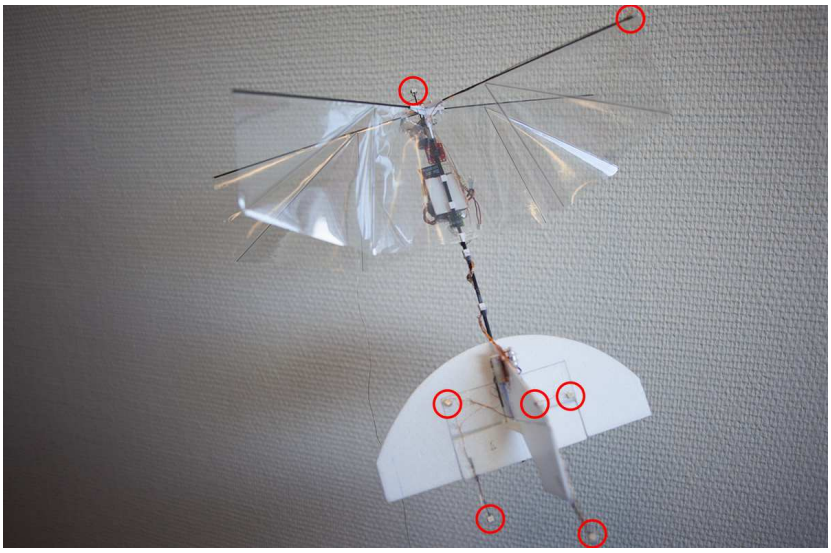

Figure 2-8: DelFly II used for system identification experiments. Red circles indicate LED marker positions.

Wind tunnel testing also lends itself perfectly for acquiring PIV data to analyse the flow structure in the wake of the flapping wings. PIV techniques have been succesfully used to obtain 3D temporal evolutions of the flow in the wake of the DelFly II by Percin et al. [37]. Refer back to Figure 2-7 for a qualitative example. A drawback of wind tunnel testing is that the MAV is clamped which introduces vibrations that influence the force measurements [40].

This is not the case in free-flight testing; these tests provide the most insight into the dynamic behaviour of a FWMAV. Many studies make use of optical tracking systems, e.g., OptiTrack, to estimate position and attitude [16, 41]. The OptiTrack system at the TU Delft consists of 24 infrared cameras which can track both active and passive markers at millimeter precision. The OptiTrack system is installed in the CyberZoo flight arena, a $10 \times 10 \times 7m$ volume dedicated to testing of robotic systems.

Placing markers on strategic positions on the DelFly II allows the estimation of position, attitude and even control surface deflections of the ornithopter to millimeter accuracy. Figure 2-8 shows the DelFly II indicating the marker locations that are currently used during system identification experiments. A drawback of this optical tracking system is its relatively low data acquisition frequency, usually 120-200Hz, which makes it difficult to study time-resolved force evolutions [24].

Recently the DelFly has been equipped with a miniature autopilot containing an IMU to measure accelerations and body rates directly with data rates up to 1024Hz [18, 24]. Data fusion between the on-board sensors and the OptiTrack system significantly increases the temporal resolution and accuracy of the state estimation [42].

The on-board autopilot also allows pre-programmed system identification manoeuvres, e.g., step or doublet inputs, to facilitate consistent model identification [20, 42]. To the best of the author's knowledge the DelFly is currently the only flapping-wing MAV on which on-board sensing and optical tracking data is fused and on which pre-programmed autopilot manoeuvres have been used to perform free-flight identification experiments.

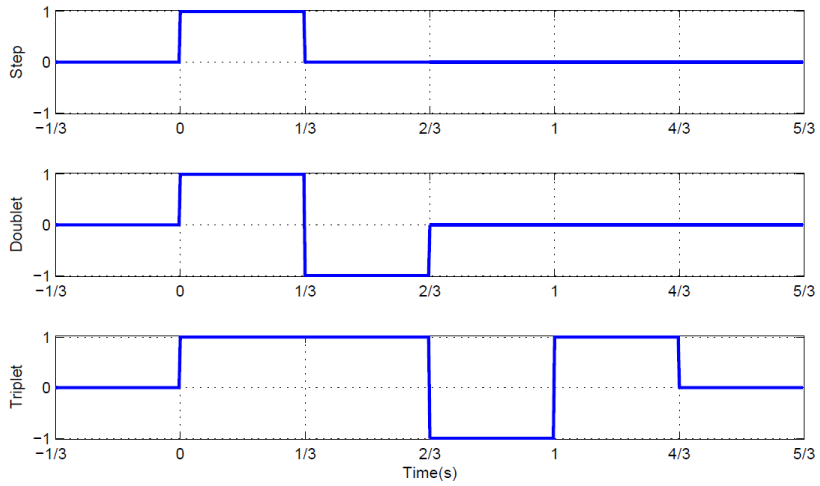

Figure 2-9: Manoeuvre input forms; step, doublet and triplet inputs used for system identification of the DelFly II. Figure taken from [43].

Input design is an important aspect of system identification. The dynamics of a system should be sufficiently excited in order to allow for a reliable estimate of the model parameters [19]. In the DelFly II many of the free-flight test data is used to fit LTI models of the dynamics. In that sense the input should be designed such that the system is not taken too far from its steady state to avoid violating the assumption of linearity. Example input signals that are used in system identification work on the DelFly II are shown in Figure 2-9.

The doublet input is the most used since it is a symmetric input about the steady-state condition and thus does not take the system too far from its initial state; this avoids violating the linearity assumption. For more remarks regarding input design for model identification of the DelFly II, refer to Armanini et al. [42].

Parameter estimation for the DelFly II is currently performed with a Maximum Likelihood Estimator (MLE), using Ordinary Least Squares (OLS) estimation to provide a first guess of the parameters. The MLE does not always converge to the global minimum of the cost function but has been found to give more consistent results in the case of a succesful estimation process [18]. Grauer et al. also use a maximum likelihood based estimation in their work [17].

To validate a model the estimated model is used to predict the output to input signals generated in validation experiments. This is a very strong form of validation since the data is generated with the actual platform. The correlation of the measured output with the model-predicted output is a good metric to evaluate the fitness of the model. An often used quantification of the correlation is Pearsons' Correlation Coefficient (PCC), see Equation (2-14) [44, 18, 24],

$$PCC = \frac{\text{cov}\left(X_{model}, \hat{X}\right)}{\sigma\left(X_{model}\right)\sigma\left(\hat{X}\right)} \tag{2-14}$$

where X_{model} is any output predicted by the model to be validated and $\hat{X}$ is the estimated or measured output. A correlation coefficient of 0 means two signals are completely uncorrelated whereas a value of 1 indicates identical signals.

2-5 Synthesis

From this literature review a clear gap in current FWMAV models is found. Tail contributions are only modelled implicitly. Dedicated tail models are platform specific and ignore the interaction with the flapping wings. The current lack of understanding of the tail effect hampers the development of smaller FWMAV platforms with higher manoeuvrability.

Improving the understanding of the effect of the tail calls for models which include the tail explicitly. Ultimately these models might help the development of tailless FWMAV platforms by extrapolation to a tailless case, providing baseline models for tailless platforms that can be used to design control algorithms.

System identification provides a solution to model wing-tail interactions without a priori knowledge of the underlying physics. The interactions can be investigated by creating full-scale robotic flappers featuring different tail geometries and gathering data both in wind tunnels and in free-flight.

The model structures can be chosen such that the resulting models are easy to use, provide physical insight into the effect of the tail and allow for an assessment of the stability characteristics of the system. As such this study should help to bridge the gap in understanding of tail effects in flapping flight.

Chapter 3

Modelling the tail of the DelFly II

This chapter describes the modelling approach proposed for this thesis. Section 3-1 provides an analysis of the forces and moments and of stability criteria. Section 3-2 discusses the modelling approaches suggested.

3-1 Analysis of forces and moments

Figure 3-1 shows a schematic FBD of the DelFly II in slow, forward flight illustrating the forces and moments involved; it illustrates the forces generated by the main wing (F_w) and the horizontal stabiliser (F_h) as well as the aerodynamic moment M_a.

The DelFly features a dihedral angle in the flapping wing configuration which places the aerodynamic center of the main wing slightly above the fuselage line. The CG is located slightly below the fuselage due to the placement of the autopilot and the battery. This explains the location of the forces as given in Figure 3-1 [39].

The forces are decomposed into body-fixed coordinates. Note that the x_b and z_b-axis have been interchanged from normal convention. This is in line with other work done on the DelFly in order to avoid singularity issues due to the typically high pitch angles θ of the DelFly [42]. Figure 3-1 also shows the unconventional definition of the pitch angle used in this study. m denotes the mass of the DelFly. g is the standard gravitational acceleration.

3-1-1 Force and moment balance

Consider the DelFly in non-accelerating, slow forward flight. Using the notation of Figure 3-1 the force and moment balance is denoted in Equation (3-1).

$$\begin{aligned} \sum F_{x_b} &= -\left(F_{w_x} + F_{h_x}\right) + W \sin\theta \\ \sum F_{z_b} &= F_{w_z} - F_{h_z} - W \cos\theta \\ \sum M_{cg} &= F_{w_x}\left(z_{cg} - z_w\right) + F_{w_z}\left(x_{cg} + x_w\right) - F_{h_x}\left(z_{cg} - z_h\right) + F_{h_z} x_{cg} + M_a \end{aligned} \tag{3-1}$$

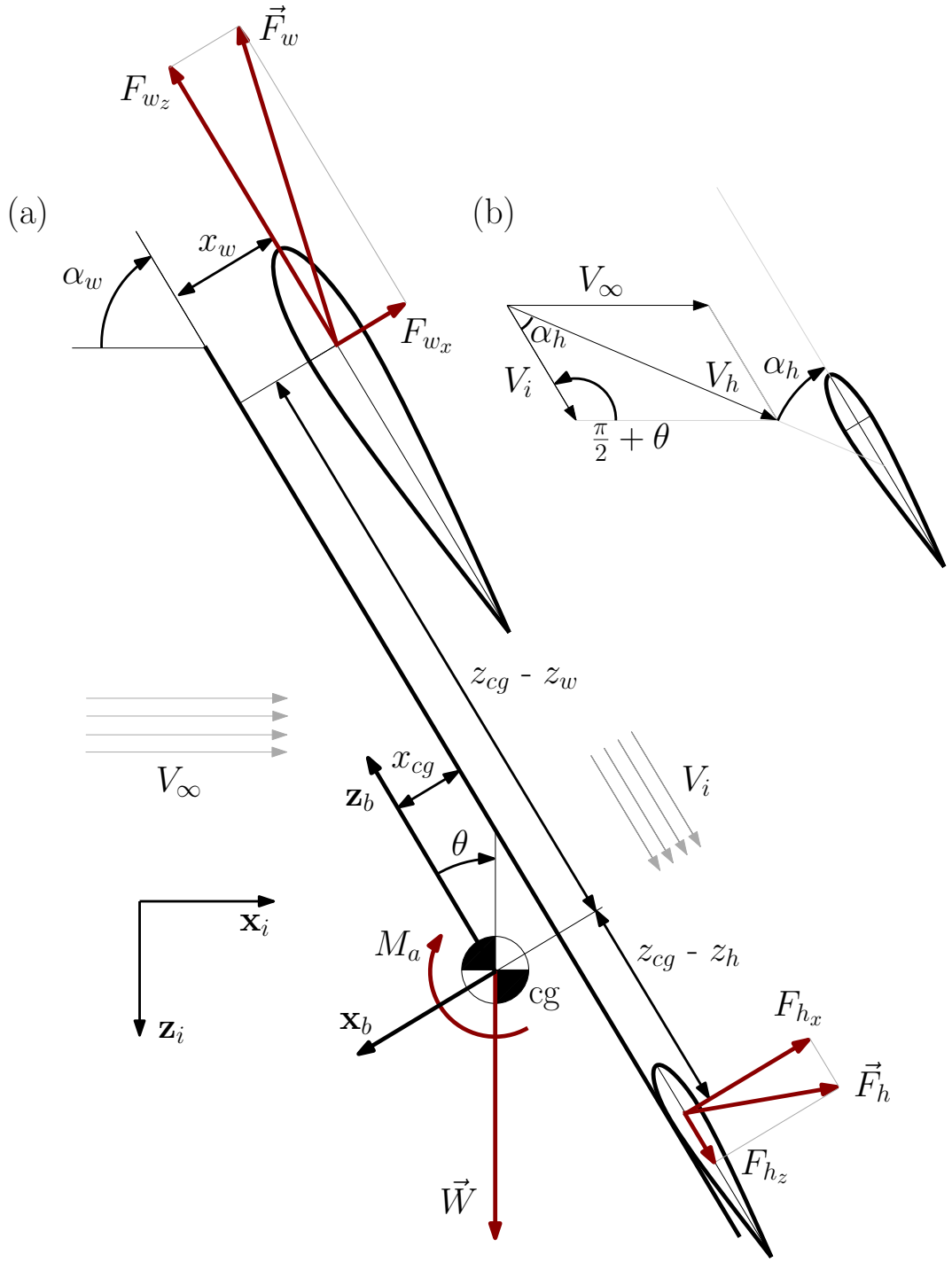

Figure 3-1: (a) - Free body diagram of the DelFly II in slow forward flight; **(b)** - Detailed view of the assumed flow conditions at the horizontal stabiliser; figure not to scale. Figure adapted from Koopmans et al. [39].

These results show that the horizontal stabiliser significantly contributes to the moment about the pitch axis. This is in line with practical experience; it is known that the tail provides most of the pitch damping during flight. The used modelling approaches should allow a study of the development of F_h with changing geometry and position of the tail.

3-1-2 Longitudinal stability

The DelFly configuration is considered to be statically stable in pitch if a disturbance in angle of attack, or pitch angle θ, leads to a change in forces and moments which counteracts the change in AoA and restores the system to its original state.

In case of steady flight the total moment $M_{cg} = 0$. If the contribution of the forces parallel to the body z_b axis are assumed to be small Equation (3-1) simplifies to Equation (3-2).

$$M_a = -F_{w_x}(z_{cg} - z_w) + F_{h_x}(z_{cg} - z_h) \tag{3-2}$$

In dimensionless form the change in moment as a result of a change in angle of attack can be denoted as Equation (3-3) [39],

$$C_{M_\alpha} = -C_{w_{x_\alpha}} \frac{(z_{cg} - z_w)}{\bar{c}} + C_{h_{x_\alpha}} \frac{(z_{cg} - z_h)}{\bar{c}} \tag{3-3}$$

with $\bar{c}$ the mean aerodynamic chord of the main wing. The platform is stable if a positive (pitch up) change in AoA leads to a pitch down (negative) moment, e.g. $C_{M_\alpha} < 0$. The location of the center of gravity is a key factor in the longitudinal stability of the platform, as is clear from Equation (3-3), determining in which flight regime the DelFly is passively stable [39].

To know if a particular concept will be stable requires knowledge on the stability derivatives $C_{w_{x_\alpha}}$ and $C_{h_{x_\alpha}}$ and on the exact CG location. Estimating the force derivatives is not easy; the flow conditions over the tail depend on many variables and tail effectiveness will vary greatly depending on the flight condition. In descending flight, for example, the velocity of the free-flow will counteract the velocity induced by the flapping wings which leads to a less effective tail surface [39].

3-2 Modelling approaches

In this section two modelling approaches are proposed in order to study the effect of tail geometry and position on the dynamics of the DelFly II. In the first approach gray-box LTI models are used, providing easy assessment of dynamic stability at the cost of less physical insight. In the second approach current quasi-steady models are extended with a term dedicated to the force generated by the tail. This method should be more general than the LTI approach but is more complicated to use since a good model structure for this approach has not yet been established.

3-2-1 Linear Time-Invariant modelling

The tail effect on the time-averaged dynamics of the DelFly can be studied well by fitting LTI models to each individual configuration. Trends in the model parameters can provide insight into the dynamic effects of the tail and can also provide inspiration for alternative model structures which are more physical in nature.

The linearised gray-box model by Armanini et al., see Equation (2-10), is proposed. This approach has proven successful in estimating the time-averaged dynamics of the DelFly II [20]. It is proposed to extend the model with an additional input variable: flapping frequency δ_f. This results in the model structure shown in Equation (3-4).

$$\begin{bmatrix} \Delta\dot{q} \\ \Delta\dot{u} \\ \Delta\dot{w} \\ \Delta\dot{\theta} \end{bmatrix} = \begin{bmatrix} \frac{M_q}{I_{yy}} & \frac{M_u}{I_{yy}} & \frac{M_w}{I_{yy}} & 0 \\ \frac{X_q}{m} - w_0 & \frac{X_u}{m} & \frac{X_w}{m} & -g\cos\theta_0 \\ \frac{Z_q}{m} + u_0 & \frac{Z_u}{m} & \frac{Z_w}{m} & -g\sin\theta_0 \\ 1 & 0 & 0 & 0 \end{bmatrix} \begin{bmatrix} \Delta q \\ \Delta u \\ \Delta w \\ \Delta\theta \end{bmatrix} + \begin{bmatrix} \frac{M_{\delta_e}}{I_{yy}} & \frac{M_{\delta_f}}{I_{yy}} \\ \frac{X_{\delta_e}}{m} & \frac{X_{\delta_f}}{m} \\ \frac{Z_{\delta_e}}{m} & \frac{Z_{\delta_f}}{m} \\ 0 & 0 \end{bmatrix} \begin{bmatrix} \Delta\delta_e \\ \Delta\delta_f \end{bmatrix} \tag{3-4}$$

Fitting LTI models for different horizontal stabilisers might reveal trends in the model parameters which can offer insight into the effect of the tail on the overall dynamics. A model parameter such as M_q, for example, yields information on the degree of pitch moment damping of the system.

The advantage of LTI models is that they are relatively easy to identify and provide easy assessment of dynamic stability characteristics through the eigenvalues of the system matrix. LTI models also lend themselves well for designing model-based control algorithms.

A drawback of these models is that their validity is limited to the flight condition about which the linearisation is made. Thus multiple models are needed to cover the full range of the DelFly's flight envelope. Studies by Armanini et al. have shown however that the variation in the parameters of the LTI models are small when looking at the slow forward flight range of the DelFly II [18]. In the range of velocities of $0.5 - 1.1ms^{-1}$ the dynamic response to elevator input is relatively similar. But since the considered scales are extremely small, even small differences may have a large impact on the behaviour of the system [42].

This result implies that if the LTI models are fitted about similar steady-state conditions it may be assumed, with reasonable confidence, that variations in the model parameters are caused by the different tail configurations. It may then be possible to derive relations for the model parameters, e.g., X_u or M_q, as a function of the geometrical parameters of the tail.

3-2-2 Quasi-steady modelling

The second approach proposed here is to extend existing quasi-steady models with an explicit term for the force generated by the tail, see Figure 3-1 for an overview. This approach has a direct physical link to the system and contains model parameters explicitly dedicated to the tail force F_h.

The quasi-steady model developed by Armanini et al. for the DelFly II is proposed due to the inclusion of clap-and-fling which significantly improves the accuracy of the model [24].

The quasi-steady model can be denoted by the following equations [11].

$$\mathrm{d}F_{x_w} = \left[\left(\frac{c(r)}{\bar{c}R}M_{wing} + m_{22}\right) v_{z_w}\dot{\theta} - \rho\Gamma v_{z_w} - m_{11}a_{x_w}\right]\mathrm{d}r - \mathrm{d}F_x^v \tag{3-5}$$

$$\mathrm{d}F_{z_w} = \left[-\left(\frac{c(r)}{\bar{c}R}M_{wing} + m_{11}\right) v_{x_w}\dot{\theta} + \rho\Gamma v_{x_w} - m_{22}a_{z_w}\right]\mathrm{d}r - \mathrm{d}F_z^v \tag{3-6}$$

$$\Gamma = \frac{1}{2}C_T c(r)|V|\sin 2\alpha + \frac{1}{2}C_R c^2(r)\dot{\theta} \tag{3-7}$$

$$\boldsymbol{F}^v = \frac{1}{2}\rho c(r)\left[C_{D_0}\cos\alpha^2 + C_{D_{\pi/2}}\sin\alpha^2\right]|V|\left(v_{x_w}, v_{z_w}\right)\mathrm{d}r \tag{3-8}$$

$$m_{11} = \frac{1}{4}\pi\rho b^2 \qquad m_{22} = \frac{1}{4}\pi\rho c^2(r) \tag{3-9}$$

$$v_{x_w} = r_i\dot{\zeta}\cos\theta_w \qquad v_{z_w} = -r_i\dot{\zeta}\sin\theta_w - \mathrm{d}c\dot{\theta_w} \tag{3-10}$$

For a detailed disussion of the model components, refer to Section 2-2. Equation (3-5) and Equation (3-6) denote the force on a single blade element, with M_{wing} the mass of a single wing. Integrating over the blade elements yields the total force acting on a wing. Clap-and-fling can be included by replacing Equation (3-7), which is the expression for circulation Γ, with Equation (2-9).

The viscous force in Equation (3-8) is a function of the drag coefficients at zero degree wing AoA (C_{D_0}) and 90 degree wing AoA $\left(C_{D_{\pi/2}}\right)$. These coefficients are estimated experimentally. Equation (3-10) denotes the velocity of the wings based on flapping rate and radial position of the blade element [24, 11].

The forces generated by the tail can be represented by Equation (3-11),

$$\begin{aligned} F_{h_x} &= \frac{1}{2}\rho V_h^2 S_h C_{h_x} \\ F_{h_z} &= \frac{1}{2}\rho V_h^2 S_h C_{h_z} \end{aligned} \tag{3-11}$$

where C_{h_x} and C_{h_z} are the tail force coefficients.

Determining suitable model structures for these force coefficients is one of the key challenges of this work. Variables that are expected to influence the tail force coefficients are the effective AoA α_h and the flapping frequency δ_f, since this influences the induced velocity and flow characteristics at the tail).

The total aerodynamic force acting on the system can now be denoted as the sum of the wing and, tail contributions, see Equation (3-12).

$$\begin{aligned} F_x &= \int_0^R \mathrm{d}F_{x_w}\mathrm{d}r + F_{x_h} \\ F_z &= \int_0^R \mathrm{d}F_{z_w}\mathrm{d}r + F_{z_h} \end{aligned} \tag{3-12}$$

It was found from literature that currently no satisfactory theoretical models exist to estimate the tail force coefficients C_{h_x} or C_{h_z}. Relations for the coefficients should thus be established by gathering experimental data and systematically experimenting with different model structures. It is desirable to include geometrical properties of the tail, such as AR, in the model structure. This would help the practical application of these models as a design tool.

Flow conditions at the tail

To apply the proposed extension of the quasi-steady model it is required to make an estimation of the flow conditions at the tail. It is known that vorticity shed by the flapping wings passes over the tail surface and influences the characteristics of the flow [37]. However, the actual effect of this unsteady airflow for the DelFly II is complicated and has not been studied in great detail yet [7]. A simplified approach is suggested here.

The velocity induced by the flapping wings, denoted V_i, can be estimated by means of actuator disk theory. If a simplified approach is used, as discussed in Section 2-2-4, and the lift force is assumed known the induced velocity generated by the wings can be computed using Equation (3-13).

$$V_i^2 = -\frac{L}{2\rho A_d} \tag{3-13}$$

The lift force L could, as a simple first approach, be approximated by the time-averaged magnitude of F_w.

The actuator disk area A_d is taken as a circle with diameter b_w, the span width of the flapping wings [6]. The magnitude and inflow angle of the free-stream at the tail is then estimated by vector summation of the two velocities, see Figure 3-1 (b). A similar approach to estimate flow conditions at the tail is used by Thomas in his aerodynamic model of birds' tails [34].

Summing the two velocities shows that the inflow velocity at the tail is likely quite different from the free-flow, V_∞, leading to a reduced effective AoA at the horizontal stabiliser. This could explain why the tail surface still generates a stabilising force even when translating at very high pitch angles, at which normal thin airfoils are well beyond their stall point [21].

From Figure 3-1 (b), the effective angle of attack at the tail can be computed from Equation (3-14).

$$\alpha_h = \frac{\pi}{2} - \theta - \text{atan}\left(-\frac{V_{h_{x_i}}}{V_{h_{z_i}}}\right) \tag{3-14}$$

Where $V_{h_{x_i}}$ and $V_{h_{z_i}}$ denote the x_i- and z_i-components of V_h in the inertial reference frame, respectively.

Chapter 4

Research methodology

This chapter presents the methodology used in this study. In order to identify models using the model structures previously discussed in Chapter 3, data needs to be acquired with different tail configurations. The platform facilitating easy testing of multiple configurations is discussed in detail in Section 4-1. Section 4-2 continues with descriptions on the planned experiments to acquire the relevant data. Then, some notes on the model identification process are given in Section 4-3. Finally, Section 4-4 presents some notes on the expected findings of the experiments.

4-1 Test platform

The platform to be used in this study is the DelFly; development of this FWMAV started in 2005 at the TU Delft. The research focuses on fully functional platforms capable of controlled flight in order to experimentally test new technologies, such as methods of autonomous flight, and increase understanding of flapping wing aerodynamics through experiments. Most DelFly configurations carry at least one on-board camera giving them some autonomous capabilities [7].

The specific FWMAV used in this study is the DelFly II. This version does not feature a camera but instead is equipped with a Lisa/S autopilot which has on-board sensing capabilities. The on-board sensors, 3-axis accelerometers and 3-axis gyroscopes, gather data to be used for system identification purposes. Figure 4-1a shows the DelFly II used in this study with the standard tail configuration.

This particular DelFly is modified in order to facilitate easy modification of the horizontal tail geometry and position. The mass is approximately 23 grams, depending on the tail configuration. This is relatively heavy due to the Lisa/S autopilot containing the on-board sensors which are needed to obtain high quality data for system identification.

This section describes the modifications made to the standard DelFly II design in order to efficiently test multiple configurations.

(a) Standard DelFly II tail **(b)** High aspect ratio tail **(c)** Base tail

Figure 4-1: Illustrating the modular tail design. Two completely different planforms fitted to the same base tail and a picture showing only the base tail.

4-1-1 Modular tail design

The tail is designed as a module which can be detached in its entirety from the rest of the DelFly in order to ease testing of multiple configurations. This is achieved by splitting the fuselage into segments.

The aft fuselage section is attached to the base tail. The base tail contains a horizontal base piece, the vertical tail and both the control surfaces, elevator and rudder. The tail surfaces are constructed out of depron foam which is easy to cut into any desired shape and is fairly durable in the event of a crash. An additional piece of foam can be slid onto the base tail in order to change the shape and size of the horizontal stabiliser.

The linear servos that actuate the rudder and elevator are connected to the vertical tail piece of the base tail. This avoids the need to remove the servos when the geometry or position of the tail is changed. With this design the geometry of the horizontal planform can be changed solely by replacing a piece of depron. Figure 4-1 illustrates different planforms attached to the base tail.

Figure 4-1b shows an extremely high aspect ratio tail design which is a potential configuration to be used for system identification. Figure 4-1c illustrates just the base tail. The base tail is the smallest possible configuration that can be tested with the current design. Qualitative testing established that this small base tail leads to a system which is unstable in pitch.

4-1-2 Varying tail position

Since the position of the tail is known to change pitch and yaw damping it is interesting to model this effect. To change the position of the tail the separate fuselage segments are used. The tail can be put very close to the main wing by connecting the main fuselage segment, containg the wings and electronics, directly to the tail segment. In case larger separation is desired an intermediate segment of any desired length can be added. The method of attachment of the separate fuselage segments is illustrated in Figure 4-2.

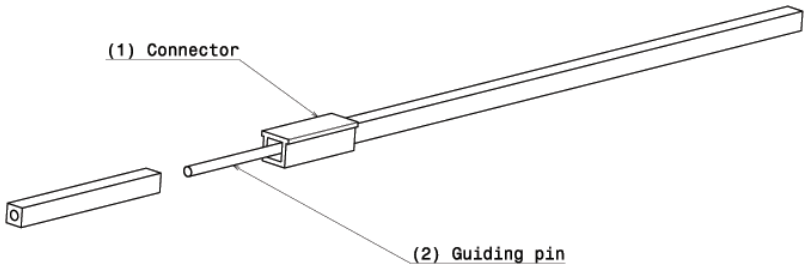

Figure 4-2: Illustration of the connection between fuselage segments.

The connection consists of two basic elements. The connector (1) is glued to one end of a fuselage segment. The inner cross-section of the connector fits exactly over the fuselage. The fuselage segment to be connected, on the left-hand side in Figure 4-2, is inserted into the connector. This prevents rotation of the fuselage segments. The guiding pin (2) fits exactly into the hollow cross-section of the fuselage and helps to align the two segments. The guiding pin is also glued to the fuselage segment.

Finally some hot glue is applied around the connector to make the connection more robust. This type of glue can be reheated and easily removed to interchange the fuselage segments.

4-1-3 Variable parameters

This section discusses the physical parameters of the DelFly that can be changed during experiments. The general shape of the horizontal stabiliser planform is fixed; the focus lies on the more generic geometric parameters (AR and surface area S). The variable parameters are illustrated in the schematic in Figure 4-3.

A total of six parameters are used to study the effect of the geometry and position of the horizontal stabiliser on the dynamics of the DelFly. Four of the six parameters serve to define the planform of the horizontal stabiliser. Table 4-1 gives these four parameters along with an expected range of values. The general shape of the planform will be fixed as in Figure 4-3 because it is easy to cut this shape without requiring templates.

The ellipsoidal tail used in the standard DelFly II tail, see Figure 4-1a, requires a template to cut the foam in the correct radius. Multiple templates would be required if the radius of the ellipsoid changes; this considerably increases the effort needed for the production of multiple tails. The effect of changing the shape of the leading edge should be taken into account when analysing the results.

The two remaining parameters determine the longitudinal position of the tail, x_h, and the longitudinal position of the Lisa/S-battery assembly, x_e. Table 4-1 also specifies expected ranges for these parameters. Adjusting the position of the battery and electronics gives additional control over the location of the CG of the complete system. The CG location can be kept more or less the same for different tail configurations to ensure a comparison of the tail effects instead of the effect of changing the CG position.

The parameter ranges mentioned in Table 4-1 are based on practical limitations and engineering judgment. During the remainder of this thesis these ranges will be experimentally determined and refined by manual controlled flight using widely different configurations.

Parameter description	Symbol	Expected range (mm)
Leading edge span	$b_{h_{LE}}$	$60 - 100$
Horizontal tail span	b_h	$100 - 250$
Root chord	c_r	$55 - 80$
Tip chord	c_t	$20 - 40$
Tail position	x_h	$6 - 90$
Electronics position	x_e	$40 - 60$

Table 4-1: Description of the variable parameters in the platform used to study tail effects on the dynamics.

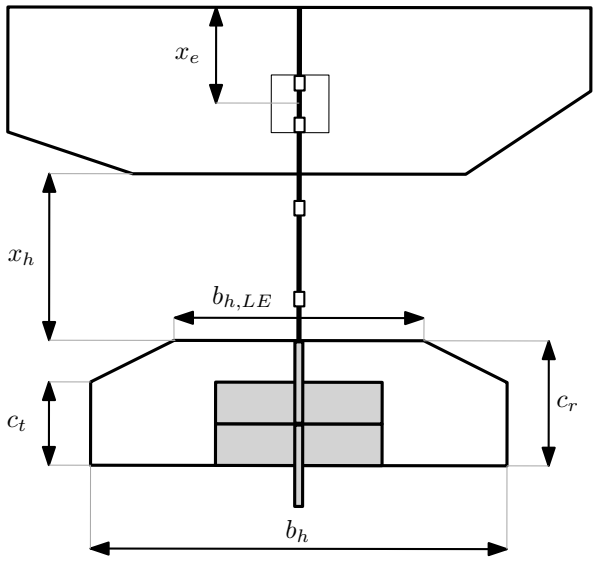

Figure 4-3: Schematic illustrating the variable parameters in the DelFly.

Boundaries will be determined for all design parameters based on the handling qualities of the platform. This results in the design space from which a number of configurations shall be selected for model identification.

For model identification a minimum of three configurations for each of the parameters to be studied is recommended to be able to identify possible trends in dynamic behaviour. Thus for AR, surface area and longitudinal position of the horizontal tail a minimum of nine configurations is required. These configurations should cover a wide range of the design space such that the likelihood of discovering trends increases.

It is recommended to choose one additional configuration per parameter to validate if the identified models can also be generalised to other tail configurations.

4-2 Experiments

This section describes the proposed experiments to acquire all the necessary data to perform model identification of the DelFly for different tail configurations.

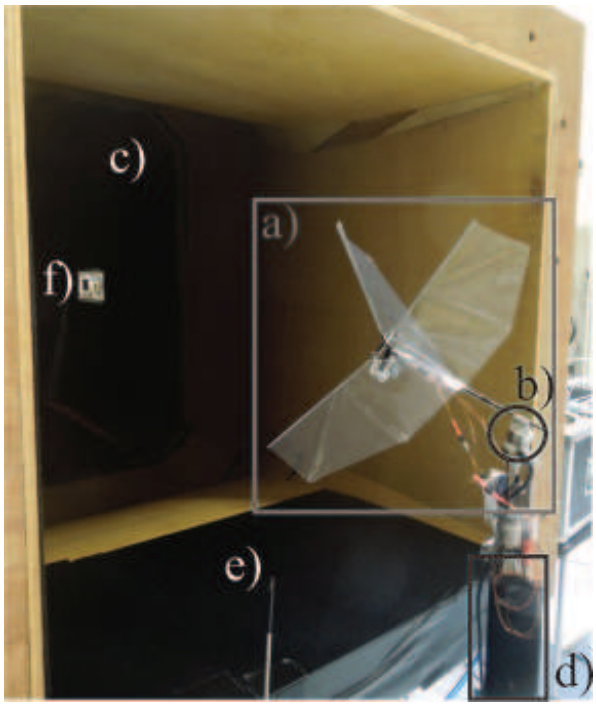

Figure 4-4: Photograph of the wind tunnel set-up: **(a)** ornithopter; **(b)** ATI Nano-17 force transducer; **(c)** open section wind tunnel; **(d)** actuated strut; **(e)** hot-wire anemometer; **(f)** thermocouple. Picture taken from Armanini et al. [24]

4-2-1 Wind tunnel

Wind tunnel measurements are useful to obtain accurate force and moment measurements at any desired flight condition. During wind tunnel tests is it also possible to remove the tail completely in order to measure the forces and moments generated by the wing alone. Performing experiments both with and without tail allows the contribution of the tail, F_h, to be isolated from the wing contribution F_w.

Wind tunnel tests shall be performed in the W-tunnel at the TU Delft Faculty of Aerospace Engineering. This is a low-speed, low-turbulence ($\approx 1\%$) wind tunnel. The DelFly is placed in a $0.6 \times 0.6m$ test section which is large enough to minimise boundary effects from the test section [31]. A photograph of the test setup is seen in Figure 4-4.

Forces and moments are measured with a high accuracy ATI Nano-17 Titanium force transducer with a 0.149gram-force resolution. This is the same sensor used in previous wind tunnel experiments conducted for the DelFly II [31, 24]. A hot-wire anemometer measures the exact flow conditions inside the test section.

The main advantage of the wind tunnel experiment is that accurate force and moment measurements can be obtained both with and without tail. This allows the tail contribution to be isolated and enables estimation of the tail force coefficients, C_{h_x} and C_{h_z}, in the quasi-steady model. During free-flight only the total force acting on the system can be estimated making those experiments unsuited to estimate the tail force.

It is proposed to add an additional hot-wire anemometer to measure flow conditions just

upstream of the tail. It is known from studies by Percin et al. [37] and Muijres et al. [29] that the induced velocity generated by flapping wings is not constant in span-wise direction. Adding a hot-wire anemometer right in front of the leading edge of the tail and moving it to several, different span-wise positions allows for an estimation of the distribution of the induced velocity. This serves to verify the proposed induced velocity estimate and to obtain an idea of the span-wise variations in flow conditions over the tail.

Finally it is proposed to perform a qualitative analysis of the flow conditions at the tail by introducing smoke into the free-stream and capturing high speed camera images. This provides insight into the flow conditions at the tail and may help the interpretation of force and moment measurements resulting from different configurations.

4-2-2 Free-flight testing

To study the dynamic stability and behaviour of the DelFly II it is necessary to excite the system. In the current wind tunnel set-up this is impossible due to the DelFly being clamped to the force balance. Free-flight inside the wind tunnel is possible but complicates model identification due to the need for active stabilisation. Thus free-flight experiments shall be performed at the TU Delft CyberZoo: a $10 \times 10 \times 7m$ flight arena equipped with an optical tracking system. The current state-of-the-art of performing free-flight experiments with FWMAVs has been discussed in Section 2-4.

System identification testing during free-flight of an ornithopter is the most realistic experiment that can be performed. However on-board sensors and optical tracking technology have only recently evolved to a level which allows for high quality state estimations during free-flight. These technologies will be used in this study to extend the current models of the DelFly II.

In free-flight only the total forces and moments acting on the body can be estimated. This means the tail contribution to the dynamics can not be explicitly isolated from that of the flapping wings. The data acquired during free-flight is therefore only suited to fit the proposed LTI model structure.

During the experiments the dynamics shall be consistently excited using pre-programmed manoeuvres, most likely a doublet input form, see Figure 2-9 for an example. The proposed model structure contains two input variables: elevator deflection δ_e and flapping frequency δ_f. Both input variables have to be excited independently during the experiments to ensure a good estimation process.

Figure 4-5 shows a flow diagram with the steps involved in performing free-flight experiments. An experiment starts with preparation of a specific configuration, given a tail geometry and position. The CG position of the configuration should be checked and noted. This is done by means of an Excel worksheet containing positions and masses of all parts in the DelFly, see Appendix A for an example of the calculation sheet.

For consistency of the experiments it is attempted to keep the CG position more or less constant even when changing the tail configuration. This can be achieved by adjusting the position of the autopilot and battery assembly, refer back to Figure 4-3 for details.

The concept of the base tail has resulted in a smaller surface area of the elevator. Qualitative testing suggests that the smaller elevator is still sufficient for proper excitation of the longi-

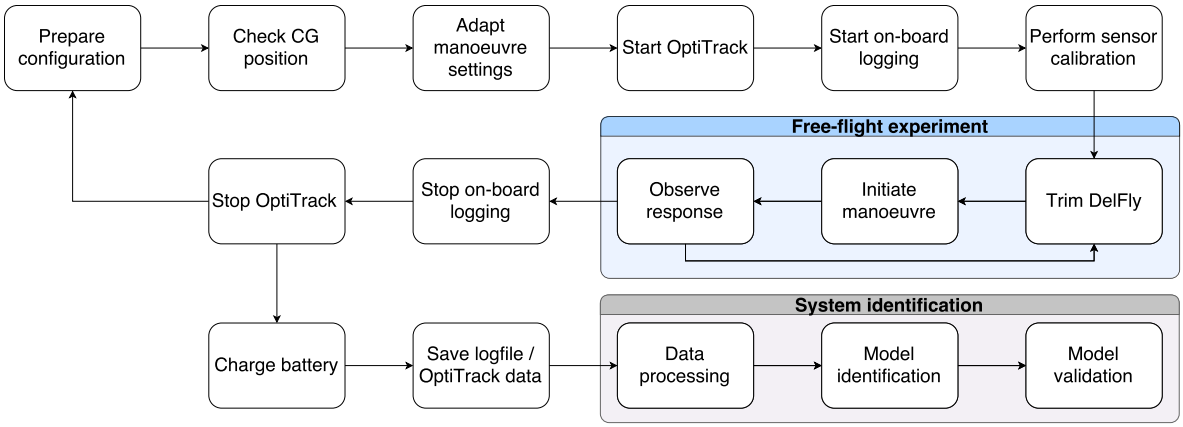

Figure 4-5: Flow diagram of the actions involved with free-flight experiments.

tudinal dynamics; this should however be supported by quantitative data. It is likely that different configurations require different elevator deflections for sufficient excitation. It might be necessary to adapt the manoeuvre deflection or duration depending on the configuration. The need for this should be determined from the observed response to the manoeuvres during free-flight.

Sensor calibration is performed in order to estimate the alignment of the IMU with respect to the body-fixed coordinate system. To perform calibration the DelFly is placed in the center of the CyberZoo and statically moved to different attitudes whilst logging data such that the OptiTrack data and IMU data can be compared. It is recommended to perform calibration before the start of every individual experiment because the system is very sensitive to changes in configuration. After calibration the actual free-flight experiment according to the steps in Figure 4-5 can start.

Data logging is started after the configuration and all the systems have been prepared. From Figure 4-5, OptiTrack logging is started first. Starting OptiTrack first is important because activating the on-board logging also switches on two of the seven LED markers on the DelFly, being the marker on top of the vertical tail and the marker on top of the rudder. This allows synchronisation between the OptiTrack data and the on-board sensors as the appearance of these two markers will be seen by the OptiTrack system.

The DelFly is flown manually throughout the course of the experiment. Before triggering a manoeuvre it is important to trim the DelFly to a steady-state condition. After initiation the system should be given time to respond to the input without additional inputs. Therefore the autopilot is programmed to keep the rudder input fixed during the duration of a manoeuvre. After the pitch motion has dampened out the DelFly can be steered to a new flight path and the manoeuvre can be repeated.

During each flight several manoeuvres are attempted to obtain sufficiently large data sets for model identification. Enough data has to be available such that part of the data set can be withheld for model validation.

After a number of manoeuvres the DelFly is landed and data logging can be terminated, see Figure 4-5. Afterwards the OptiTrack session can be stopped. It is important to switch off on-board logging first such that switching off of the two LED markers is visible in the

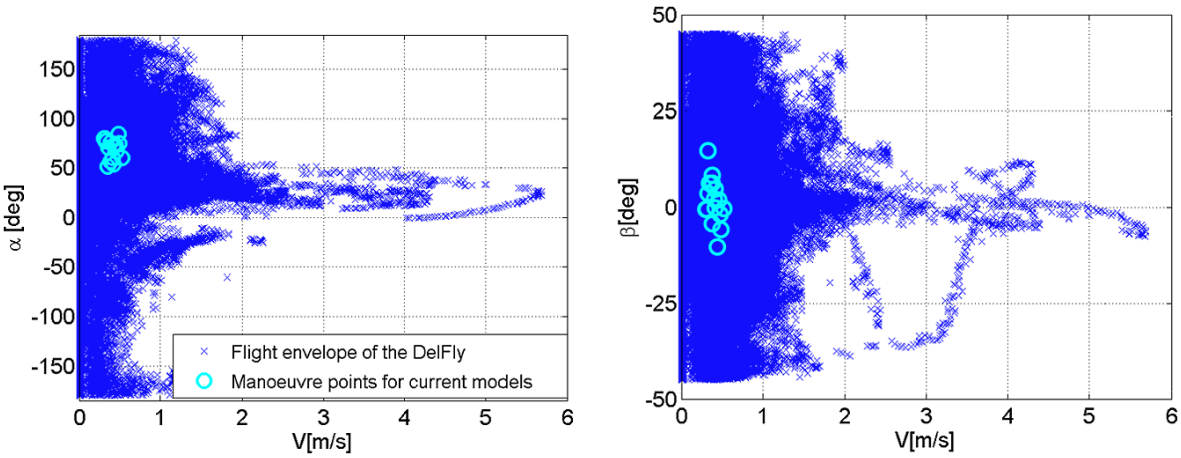

Figure 4-6: Flight envelope of the DelFly II. The manoeuvre points are those used by Armanini et al. in their study to identify a time-varying model of the DelFly II dynamics. Figure taken from that study by Armanini et al. [20].

OptiTrack data for synchronisation. Whilst charging the battery downloading both on-board and OptiTrack data can start. During this time it is also possible to begin preparation of the configuration for the next experiment.

The final steps in Figure 4-5 show the downloaded data being processed and used for model identification and validation. For more notes on this see Section 4-3.

4-2-3 Flight conditions

The flight condition to be used is an important experiment design parameter since the effectiveness of the tail is largely dependent on the flight condition: In hover the only flow passing over the tail is the induced flow generated by the flapping wings whilst in fast forward flight the free-stream velocity becomes dominant. This also makes it difficult to determine a single time-invariant parameter for the effectiveness of the elevator, as was found by Koopmans et al. [39].

The flight envelope of the DelFly II, found through extensive free-flight testing, is shown in Figure 4-6. The left-hand side figure shows velocity and angle of attack; in the right hand figure velocity and sideslip angle are plotted.

This study focuses on the same slow forward-flight regime indicated by the manoeuvre points in Figure 4-6. Previous system identification work has been performed in this regime meaning that flight data and baseline models using the standard DelFly II tail configuration are already available [16, 31, 20, 11]. The limited dimensions of the TU Delft CyberZoo make it impossible to perform the system identification manoeuvres at much higher velocities since the motion would not have enough time to dampen out before a steering action is required.

Qualitative testing has shown that the steady-state flight condition, with $\delta_e = 0$, changes per tail configuration. Currently the spread in steady-state conditions for different configurations has not been quantified. In the case of a large variance in flight conditions it may be unfair to directly compare the models for different tail configurations.

To cope with this it is possible to trim the DelFly to a different flight condition by setting δ_e to a non-zero value. Depending on the spread in flight conditions between configurations it may be possible to trim all configurations to the same flight condition. This would yield the most controlled comparison between different models. Using the elevator for trimming does however limit the range of deflections available for the excitation of the system.

4-3 Model identification

This section discusses the intended approach to perform model identification. The facets of state estimation, parameter estimation and finally model validation are briefly discussed and some important notes are given.

4-3-1 State estimation

State estimation is the first step towards system identification. High quality data ensures a better identification process. As discussed in Chapter 2, system identification of FWMAVs is a very active field of study. Quality of free-flight data has only recently been improved significantly by the development of miniature autopilots containing an IMU. The on-board information, augmented with off-board optical tracking data, leads to high accuracy data with a high temporal resolution [42].

A sensor fusion algorithm, using an Extended Kalman Filter (EKF), has been developed at the TU Delft to use both on-board as off-board data [42]. These algorithms are available for use in this study. This does not, however, guarantee good data sets.

Differences in outside lighting conditions, for example, can have impact on the accuracy of the OptiTrack system. This can be compensated for by changing camera settings but should be carefully taken into account when conducting free-flight experiments. The quality of each individual data set should be assessed before attempting to use it for model identification.

Another issue to take into account is vibrations introduced into the accelerometer and gyroscope data due to the flapping motion of the wings. Currently a piece of foam is used to function as a mechanical low-pass filter. This is shown in the photograph in Figure 4-7. Vibrations are however still noticeable in the data. To gain usable time-averaged data requires some additional filtering which should be done with care in order to avoid loss of information.

4-3-2 Parameter estimation

The proposed model structures have been described in Section 3-2. These dictate the parameters that should be estimated to formulate the models. For DelFly II system identification a hybrid approach of an OLS estimation to find initial parameter values and an iterative MLE search to further minimise the cost function is used [18]. Refer back to Chapter 2 for more details.

This approach to parameter estimation has already been proven with the quasi-steady and LTI modelling approaches intended in this study. It is thus suggested to apply this approach to identify individual models for the different tail configurations. It is expected that trends

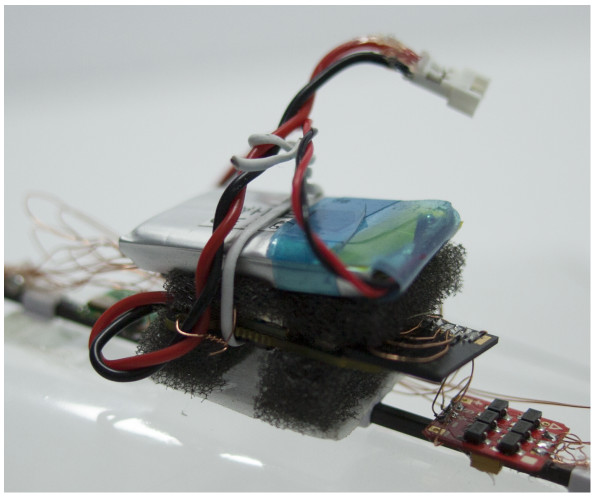

Figure 4-7: Photograph of the main electronics assembly. Picture shows the battery and autopilot with pieces of foam (dark gray) to dampen mechanical vibrations in the system.

between the different model parameters can also be modelled using, for example, OLS estimation. Since no theoretical models are available yet it is proposed to use the experimental data to find suitable model structures to represent potential trends.

A note should be given on the model structure of the tail force component in the quasi-steady model approach, F_h. Since literature again does not provide much theoretical basis to start from a suitable model structure should be determined from the data. This includes determining which variables influence the force generated by the tail. To achieve this an application of, for example, stepwise regression might be considered. Stepwise regression is a technique to systematically add or eliminate variables in the identification process based on some criterion [45]. Such a method is preferred over a trial and error approach to establish which variables influence the force generated by the tail.

4-3-3 Model validation

The final step in the system identification process is to validate the models that have been identified. This includes evaluating the predictive power of the model and assessing if the chosen model structure is suitable. In practice some criterion should be formulated in order to evaluate if a found model is "good enough" [19].

Assessing the model structure will be particularly important for the quasi-steady model approach due to a lack of a priori knowledge in this field. Therefore, validation of this model is very important. Systematic variation of the model structure, using stepwise regression for example, and evaluation of all resulting models should result in a correct model definition.

For the LTI models validation is currently achieved by holding back part of the free-flight data sets solely for validation purposes. Identification is performed with, for example, only half of the performed manoeuvres. The found models are then used to simulate the remainder of the manoeuvres in the data set, comparing the model-predicted output to the measured and estimated states. This method has been applied in DelFly system identification work (see Chapter 2), quantifying the quality of the prediction using the PCC. For the LTI models

and the quasi-steady model including clap-and-fling, correlations larger than 90% have been achieved [20, 24].

Using separate identification and validation sets and assessing correlation coefficients is also applicable in this study. Additionally it is desired to determine trends in behaviour and perhaps identify more general models which, based on the tail geometry, can predict the dynamics of the system. To validate if these models can be used to predict the dynamics of general tail geometries it is required to test additional tail configurations which have not been used to identify the trends in behaviour.

During validation the purpose of the models should always be kept in mind [19]. For this study the aim of the models is to obtain more insight into the effect of the tail on the dynamics of the DelFly. There is also a desire to use the identified models for the design of control laws which can stabilise inherently unstable configurations, leading to increased manoeuvrability of the platform.

4-4 Experiment hypotheses

This section discusses hypotheses which have been formulated to express the expected effects of changing tail geometry on the dynamics of the DelFly. Experiments should be conducted such that these expectations may be proved or disproved.

Based on the force and moment balance presented in Section 3-1 and the condition for longitudinal stability given in Equation (3-3) (i.e. $C_{M_\alpha} < 0$) some hypotheses are formulated. The hypotheses are listed below.

- Increasing the separation between the main wing and the horizontal stabiliser increases the damping capabilities of the tail due to an increase in moment arm of the tail force;
- Increasing the surface area of the horizontal tail will increase the magnitude of the tail force and thus increases pitch damping;
- Increasing the longitudinal separation decreases the relative effect of the flapping wings on the tail surface and thus decreases the effectiveness of the tail;

Testing these hypotheses against experimental results will provide additional insight into the effect of the tail on the dynamics of the DelFly II.

The first two hypotheses are rather straightforward. Since the tail force is assumed to scale linearly with surface area, see Equation (3-11), the magnitude should increase with increasing surface area. The same holds for a larger moment arm about the CG, increasing $z_{cg} - z_h$ in Equation (3-1), resulting from a larger separation between tail and flapping wings. These changes are expected to increase the stabilising moment generated by the tail and thus make the platform more stable.

The final hypothesis is more difficult to prove. Logically it can be expected that the induced velocity decreases in magnitude when measured farther away from the wing thus decreasing the velocity at the tail, V_h. The magnitude of the tail force F_h scales quadratically, see Equation (3-11). It is however currently unknown what the relative contribution of the induced flow is to the force generation of the tail, as compared to the contribution of free-flight velocity.

Chapter 5

Conclusions & Recommendations

A gap has been defined in current models of FWMAVs. Tail effects are mostly omitted or captured only implicitly. Explicit tail models are fitted to specific FWMAVs and oversimplified, ignoring the interactions with the flapping wings and offering little general insight.

The limited understanding of the effect of the tail hampers the development of smaller flapping-wing robots with higher manoeuvrability. There is thus a need for better models of FWMAVs which explicitly include the effect of the tail and take into account the total system including flapping wings.

A methodology has been proposed to bridge this gap in knowledge by applying system identification techniques on a fully functional FWMAV, the DelFly II. By performing experiments with different tail configurations more insight should be gained into the effect of the horizontal tail on the dynamics of this flapping-wing platform.

The scope of the study will primarily be limited to the effect of the horizontal stabiliser on the longitudinal dynamics. The main parameters that will be studied are: (1) tail aspect ratio; (2) tail surface area and (3) longitudinal position of the tail. Two modelling approaches have been proposed:

LTI model The first approach is to identify decoupled, longitudinal, time-averaged LTI models for each individual configuration. The effect of the tail can be studied by evaluating the changes in the model parameters. This approach is simple to use and provides an easy method of assessing the dynamic stability of the configuration. The model structure is well suited for control system design. The drawback of this model structure is that the parameters are only partly physical in nature and are not explicitly coupled to the tail design.

Quasi-steady model In the second approach quasi-steady models are extended with an explicit tail force component. Wind tunnel experiments should provide the data required to evaluate this force for different configurations and flight conditions. The advantage of this approach is its general nature and the fact that it provides a complete physical model of the system in which the tail is explicitly captured, thus providing the most insight

into the effect of the tail. The drawback is that these models are more complicated than LTI models.

The platform developed to conduct the experiments required in this study has also been presented. This newly developed DelFly allows fast changes in tail configuration for efficient testing of multiple geometries.

The literature review showed that currently no satisfactory theoretical models predicting tail lift and drag are available. A model structure for the tail force in the extended quasi-steady model thus has to be determined experimentally. It is recommended to apply techniques such as stepwise regression to systematically test and evaluate multiple model structures. Ideally the model parameters for the quasi-steady tail force are physical in nature such that they provide meaningful insights.

It is expected that the proposed research will contribute to a better understanding of the tail on the dynamics of the DelFly II in particular and FWMAVs in general by acquiring data with different tail configurations and modelling trends in behaviour due to the changes in tail geometry. Effort should be put into obtaining good identification and validation data sets to realise this objective. It is therefore recommended to take extreme care in the preparation and execution of the experiments.

Ideally this work results in models that can be generalised to any tail geometry. Linear parameter-varying models, using geometrical parameters such as tail aspect ratio as scheduling parameters, might be a solution here. This method has only recently come to attention in the context of flapping-wing MAV modelling and thus it is recommended to explore the possibilities of this approach during the remainder of this thesis.

Appendix A

Mass calculation spreadsheet

This appendix shows an example of the Excel calculation sheet used to estimate mass, position of the center of gravity and inertia properties for the DelFly used in this study. The user can input any desired component, with a given mass, and select the number of components used.

The position of the component should also be specified, with respect to a fixed reference point. In this case, the reference point is taken to be at the leading edge, in the center of the flapping mechanism. For this calculation sheet, the z-axis is parallel to the fuselage, positive direction pointing forward. The x-axis is positive pointing down towards the motor. y-axis is positive to the left.

Type	Part name	m [gr]	Remark	#	Measured positions [mm] x	y_left	y_right	z	m_total [gr]	Static moment w.r.t. origin [g.mm] Sx	Sy	Sz	Inertia w.r.t. CG [g.mm2] Ixx	Iyy	Izz	Ixy	Iyz	Ixz
Injection molded standard parts	Gearbox frame	0,849		1	10	0,000	0,000	-8,000	0,849	8,490	0,000	-6,792	3593,633	3607,332	13,699	0,000	0,000	221,877
	Wing hinge	0,224		2	0	0,000	0,000	0,000	0,448	0,000	0,000	0,000	2391,308	2407,345	16,037	0,000	0,000	-195,832
	Wing holder	0,044		1	0	0,000	0,000	-85,000	0,044	0,000	0,000	-3,740	6,273	7,848	1,575	0,000	0,000	3,143
	Push rod	0,062		2	10	10,000	-10,000	1,000	0,124	1,240	0,000	0,124	692,523	682,123	14,401	0,000	0,000	36,889
	Spur gear 48t / 9t	0,170		1	26	0,000	0,000	-4,000	0,170	4,420	0,000	-0,680	878,889	810,774	68,115	0,000	0,000	235,002
	Custom gear	0,200		2	20,5	7,000	-7,000	0,000	0,400	8,200	0,000	0,000	2219,392	2154,696	103,896	0,000	0,000	424,241
	Pinion 9t	0,022		1	18	0,000	0,000	-4,500	0,022	0,396	0,000	-0,099	106,587	103,410	3,177	0,000	0,000	18,125
	Glasses	0,100	approx.	1	20,5	0,000	0,000	-2,000	0,100	2,050	0,000	-0,200	504,950	526,024	21,074	0,000	0,000	103,157
Brushless motor	Motor rotor	0,870		1	18	0,000	0,000	-17,000	0,870	15,660	0,000	-14,790	2734,154	2859,787	125,633	0,000	0,000	586,089
	Motor stator 28 windings	0,500	approx.	1	18	0,000	0,000	-17,000	0,500	9,000	0,000	-8,500	1571,353	1643,556	72,203	0,000	0,000	336,833
	Bearings	0,030		2	10	0,000	0,000	-17,000	0,060	0,600	0,000	-1,020	188,562	189,530	0,968	0,000	0,000	13,511
Rivets	Rivet 0.78mm	0,030		5	20,5	0,000	0,000	-4,000	0,150	3,075	0,000	-0,600	715,389	747,000	31,611	0,000	0,000	150,380
	Rivet 1.00mm	0,102		1	0	0,000	0,000	-2,000	0,102	0,000	0,000	-0,204	515,049	518,700	3,651	0,000	0,000	-43,366
Wings	Wing 28cm (excl. LE)	1,000		2	-7	67,000	-67,000	-40,000	2,000	-14,000	0,000	-80,000	11163,906	2523,028	9315,122	0,000	0,000	-858,439
	LE. D-profile	0,162		2	-7	70,000	-70,000	0,000	0,324	-2,268	0,000	0,000	3317,028	1784,042	1642,214	0,000	0,000	-307,328
Fuselage	Fuselage front section	0,393	est.	1	0	0,000	0,000	-45,000	0,393	0,000	0,000	-17,680	309,346	323,411	14,065	0,000	0,000	-65,961
	Fuselage mid section	0,306	est.	1	0	0,000	0,000	-125,000	0,306	0,000	0,000	-38,198	824,398	835,337	10,939	0,000	0,000	94,964
	Fuselage tail-section	0,306	est.	1	0	0,000	0,000	-195,000	0,306	0,000	0,000	-59,589	4543,847	4554,786	10,939	0,000	0,000	222,948
	Guiding pin front-middle	0,040	approx.	1	0	0,000	0,000	-95,000	0,040	0,000	0,000	-3,800	19,255	20,687	1,432	0,000	0,000	5,251
	Guiding pin middle-tail	0,026	approx.	1	0	0,000	0,000	-170,000	0,026	0,000	0,000	-4,420	244,332	245,263	0,931	0,000	0,000	15,080
	Fuselage holder front-middle	0,036	approx.	1	0	0,000	0,000	-95,000	0,036	0,000	0,000	-3,420	17,329	18,618	1,289	0,000	0,000	4,726
	Fuselage holder middle-tail	0,036	approx.	1	0	0,000	0,000	-170,000	0,036	0,000	0,000	-6,120	338,306	339,595	1,289	0,000	0,000	20,880
Servo assembly	Linear servo	1,200	TBD	2	-10	4,000	-4,000	-195,000	2,400	-24,000	0,000	-468,000	35724,965	36299,668	651,503	0,000	0,000	4677,557
	Pushrod hook	0,015	TBD	4	-12,5	9,000	-9,000	-165,000	0,060	-0,750	0,000	-9,900	512,040	527,677	25,358	0,000	0,000	101,960
	Pushrod, 1mm hollow	0,024	TBD	2	-12,5	9,000	-9,000	-165,000	0,048	-0,600	0,000	-7,920	409,632	422,142	20,286	0,000	0,000	81,568
Battery	180 mAh Hyperion	5,510		1					5,510	93,670	0,000	-286,520	2581,528	2668,870	806,510	0,000	0,000	1278,398
	Cable	0,500	approx.	1	17	5,000	-5,000	-52,000	0,500	0,000	0,000	0,000	2668,870	2686,769	17,899	0,000	0,000	-218,562
Electronics	Lisa/S with Superbit RF	2,800		1	10	5,000	-5,000	-52,000	2,800	28,000	0,000	-145,600	1311,847	1287,027	115,179	0,000	0,000	236,867
	ESC MX-3A	0,380		1	2	0,000	0,000	-28,000	0,380	0,760	0,000	-10,640	771,548	777,577	6,029	0,000	0,000	-68,202
	Receiver	0,270	TBD	1	2	0,000	0,000	-73,000	0,270	0,540	0,000	-19,710	0,001	4,285	4,284	0,000	0,000	-0,064
	SD - card	0,250	approx.	1	27	0,000	0,000	-37,000	0,250	6,750	0,000	-9,250	325,078	435,506	110,427	0,000	0,000	189,466
Others	Lisa/S holding sliders	0,036	approx.	2	0	0,000	0,000	-52,000	0,072	0,000	0,000	-3,744	31,933	34,511	2,577	0,000	0,000	-9,072
	Lisa/S support depron	0,052	approx.	1	2	5,000	-5,000	-52,000	0,052	0,104	0,000	-2,707	24,394	23,919	2,128	0,000	0,000	-4,368
	Lisa/S support foam	0,016	approx.	2	4,5	5,000	-5,000	-52,000	0,032	0,144	0,000	-1,664	14,993	14,263	0,870	0,000	0,000	-0,999
	Battery support foam	0,034	approx.	1	13	5,000	-5,000	-52,000	0,034	0,442	0,000	-1,768	15,930	16,754	2,524	0,000	0,000	5,024
	OptiTrack LEDs	0,020	TBD	7	0	0,000	0,000	0,000	0,140	0,000	0,000	0,000	747,284	752,295	5,012	0,000	0,000	-61,197
	Resistor	0,090	TBD	0	0	0,000	0,000	0,000	0,000	0,000	0,000	0,000	0,000	0,000	0,000	0,000	0,000	0,000
	Servo connector	0,400	TBD	0	2	0,000	0,000	-120,000	0,000	0,000	0,000	0,000	0,000	0,000	0,000	0,000	0,000	0,000
	Battery tie strap	0,100	TBD	1	15	0,000	0,000	-52,000	0,100	1,500	0,000	-5,200	44,352	52,482	8,130	0,000	0,000	18,989
Tail	Vertical tail base piece	0,172	est.	1	-25,18	0,000	0,000	-213,450	0,172	-4,326	0,000	-36,675	3386,472	3553,333	166,861	0,000	0,000	751,712
	Rudder	0,198	est.	1	-38,79	0,000	0,000	-248,420	0,198	-7,675	0,000	-49,151	6084,231	6480,854	396,623	0,000	0,000	1553,431
	Horizontal tail base piece	0,200	est.	1	-2	20,000	-20,000	-218,000	0,200	-0,400	0,000	-43,586	4280,164	4212,932	92,716	0,000	0,000	231,341
	Elevator	0,200	est.	1	-2	20,000	-20,000	-242,000	0,200	-0,400	0,000	-48,385	5786,309	5719,077	92,716	0,000	0,000	269,647
	Test tail piece	0,831	variable	1	-2	48,743	-48,743	-210,011	0,831	-1,663	0,000	-174,582	17566,616	15644,536	2028,037	0,000	0,000	908,855
				Total sum					21,554	128,960	0,000	-1574,730	119048,009	109097,024	16023,930	0,000	0,000	10964,521

	Mass	CG position [mm]			Inertia [kg.m2]					
		x	y	z	Ixx	Iyy	Izz	Ixy	Iyz	Ixz
Estimated	21,554	5,983	0,000	-73,060	1,19E-04	1,09E-04	1,60E-05	0	0	1,10E-05
Measured mass	23,520	5,983	0,000	-73,060	1,34E-04	1,23E-04	1,80E-05	0	0	1,23E-05

Bibliography

[1] Sane, S. P., "The aerodynamics of insect flight," *Journal of Experimental Biology*, Vol. 206, December 2003, pp. 4191–4208.

[2] Ellington, C., "The Aerodynamics of Hovering Insect Flight. I. The Quasi-Steady Analysis," *Philosophical Transactions of the Royal Society of London, Series B: Biological Sciences*, Vol. 305, 1984, pp. 1–15.

[3] Dickinson, M., Lehmann, F., and Sane, S., "Wing Rotation and the Aerodynamic Basis of Insect Flight," *Science*, Vol. 284, 1999, pp. 1954–1960.

[4] Sane, S. and Dickinson, M., "The aerodynamic effects of wing rotation and a revised quasi-steady model of flapping flight," *Journal of Experimental Biology*, Vol. 205, 2002, pp. 1087–1096.

[5] Taha, H., Hajj, M., and Nayfeh, A., "Flight dynamics and control of flapping-wing MAVs: a review," *Nonlinear Dynamics*, Vol. 70, No. 2, July 2012, pp. 907–939.

[6] Chin, D. and Lentink, D., "Flapping wing aerodynamics: from insect to vertebrates," *Journal of Experimental Biology*, Vol. 219, 2016, pp. 920–932.

[7] de Croon, G., Percin, M., Remes, B., Ruijsink, R., and de Wagter, C., *The DelFly: Design, Aerodynamics, and Artificial Intelligence of a flapping Wing Robot*, Springer, 2016.

[8] Taha, H., Hajj, M., and Beran, P., "State-space representation of the unsteady aerodynamics of flapping flight," *Aerospace Science and Technology*, Vol. 34, February 2014, pp. 1–11.

[9] Ma, K., Chirarattananon, P., Fuller, S., and Wood, R., "Controlled Flight of a Biologically Inspired, Insect-Scale Robot," *Science*, Vol. 340, May 2013, pp. 603–607.

[10] de Croon, G., de Clerq, K., Ruijsink, R., Remes, B., and de Wagter, C., "Design, aerodynamics, and vision-based control of the DelFly," *International Journal of Micro Air Vehicles*, Vol. 1, No. 2, 2009, pp. 71–97.

[11] Armanini, S., Caetano, J., de Visser, C., de Croon, G., and Mulder, M., "Aerodynamic Model Identification of a Clap-and-Fling Flapping-Wing MAV: a Comparison between Quasi-Steady and Black-Box Approaches," *AIAA Atmospheric Flight Mechanics Conference*, San Diego, California, USA, January 2016.

[12] Wood, R., "The First Takeoff of a Biologically Inspired At-Scale Robotic Insect," *IEEE Transactions on Robotics*, Vol. 24, No. 2, 2008, pp. 341–347.

[13] de Croon, G., Groen, M., de Wagter, C., Remes, B., Ruijsink, R., and van Oudheusden, B., "Design, aerodynamics and autonomy of the DelFly," *Bioinspiration & Biomimetics*, Vol. 7, No. 2, 2012, pp. 1–16.

[14] Keennon, M., Klingebiel, K., Won, H., and Andriukov, A., "Development of the Nano Hummingbird: A Tailless Flapping Wing Micro Air Vehicle," *50th AIAA Aerospace Sciences Meeting including the New Horizons Forum and Aerospace Exposition*, Nashville, Tennessee, January 2012.

[15] Grauer, J., Ulrich, E., Hubbard, J., Pines, D., and Humbert, J., "Testing and System Identification of an Ornithopter in Longitudinal Flight," *Journal of Aircraft*, Vol. 48, No. 2, March-April 2011, pp. 660–667.

[16] Caetano, J., de Visser, C., de Croon, G., Remes, B., de Wagter, C., Verboom, J., and Mulder, M., "Linear Aerodynamic Model Identification of a Flapping Wing MAV Based on Flight Test Data," *International Journal of Micro Air Vehicles*, Vol. 5, December 2013, pp. 273–286.

[17] Grauer, J., *Modeling and System Identification of an Ornithopter Flight Dynamics Model*, Ph.D. thesis, University of Maryland, College Park, 2012.

[18] Armanini, S., de Visser, C., and de Croon, G., "Black-box LTI modeling of flapping-wing micro aerial vehicle dynamics," *AIAA Atmospheric Flight Mechanics Conference*, Kissimmee, Florida, January 2015.

[19] Ljung, L., *System Identification: Theory for the User*, Pearson Education (US), 2nd ed., December 1998.

[20] Armanini, S., de Visser, C., de Croon, G., and Mulder, M., "Time-Varying Model Identification of Flapping-Wing Vehicle Dynamics Using Flight Data," *Journal of Guidance, Control, and Dynamics*, Vol. 39, No. 3, March 2016, pp. 526–541.

[21] Anderson, J. D., *Fundamentals of Aerodynamics*, McGraw Hill, 5th SI units ed., 2011.

[22] Dickinson, M. H. and Götz, K., "Unsteady Aerodynamic Performance of Model Wing at Low Reynolds Number," *Journal of Experimental Biology*, Vol. 174, 1993, pp. 45–64.

[23] Percin, M., Hu, Y., van Oudheusden, B., Remes, B., and Scarano, F., "Wing flexibility effects in clap-and-fling," *Proceedings of the International Micro Air Vehicles conference 2011 summer edition*, 2011.

[24] Armanini, S., Caetano, J., de Croon, G., de Visser, C., and Mulder, M., "Quasi-Steady Aerodynamic Model of Clap-and-Fling Flapping MAV and Validation using Free-Flight Data," *Bioinspiration & Biomimetics*, Vol. 11, No. 4, June 2016.

[25] Berman, G. and Wang, Z., "Energy-minimizing kinematics in hovering insect flight," *Journal of Fluid Mechanics*, Vol. 582, 2007, pp. 153–168.

[26] Sane, S. and Dickinson, M., "The Control of Flight Force By A Flapping Wing: Lift and Drag Production," *Journal of Experimental Biology*, Vol. 204, May 2001, pp. 2607–2626.

[27] Birch, J. and Dickinson, M., "The influence of wing-wake interactions on the production of aerodynamic force in flapping flight," *Journal of Experimental Biology*, Vol. 206, March 2003, pp. 2257–2272.

[28] Sane, S., "Induced airflow in flying insects I. A theoretical model of the induced flow," *Journal of Experimental Biology*, Vol. 209, 2005, pp. 32–42.

[29] Muijres, F., Spedding, G., Winter, Y., and Hedenström, A., "Actuator disk model and span efficiency of flapping flight in bats based on time-resolved PIV measurements," *Experiments in Fluids*, Vol. 51, 2011, pp. 511–525.

[30] Sun, M. and Wu, J., "Aerodynamic force generation and power requirements in forward flight in a fruit fly with modeled wing motion," *Journal of Experimental Biology*, Vol. 206, 2003, pp. 3065–3083.

[31] Caetano, J., Armanini, S., de Visser, C., de Croon, G., and Mulder, M., "Data-Informed Quasi-Steady Aerodynamic Model of a Clap-and-Fling Flapping Wing MAV," *International Conference on Intelligent Unmanned Systems*, Bali, Indonesia, August 2015.

[32] Grauer, J., Ulrich, E., Hubbard, J., Pines, D., and Humbert, J., "Model Structure Determination of an Ornithopter Aerodynamics Model from Flight Data," *48th AIAA Aerospace Sciences Meeting Including the New Horizons Forum and Aerospace Exposition*, Orlando, Florida, January 2010.

[33] Shkarayev, S. and Silin, D., "Applications of Actuator Disk Theory to Membrane Flapping Wings," *AIAA Journal*, Vol. 48, No. 10, October 2010, pp. 2227–2234.

[34] Thomas, A., "On the aerodynamics of birds' tails," *Philos. Trans. R. Soc. London, Ser. B*, Vol. 340, 1993, pp. 361–380.

[35] Maybury, W., Rayner, J., and Couldrick, L., "Lift generation by the avian tail," *Philosophical Transactions of the Royal Society of London, Series B: Biological Sciences*, Vol. 268, 2001, pp. 1443–1448.

[36] Tay, W., Bijl, H., and van Oudheusden, B., "Biplane and Tail Effects in Flapping Flight," *42nd AIAA Fluid Dynamics Conference and Exhibit*, New Orleans, June 2012.

[37] Percin, M., Eisma, H., van Oudheusden, B., Remes, B., Ruijsink, R., and de Wagter, C., "Flow visualization in the wake of flapping-wing MAV 'DelFly II' in forward flight," *30th AIAA Applied Aerodynamics Conference*, New Orleans, Louisiana, June 2012.

[38] Percin, M., *Aerodynamic Mechanisms of Flapping Flight*, Ph.D. thesis, Delft University of Technology, 2015.

[39] Koopmans, J., Tijmons, S., de Wagter, C., and de Croon, G., "Passively Stable Flapping Flight From Hover to Fast Forward Through Shift in Wing Position," *International Journal of Micro Air Vehicles*, Vol. 7, No. 4, 2015, pp. 407–418.

[40] Caetano, J., Percin, M., de Visser, C., van Oudheusden, B., de Croon, G., de Wagter, C., Remes, B., and Mulder, M., "Tethered vs. Free Flight Force Determination of the DelFly II Flapping Wing Micro Air Vehicle," *2014 International Conference on Unmanned Aircraft Systems (ICUAS), Orlando, FL, USA*, May 2014, pp. 942–948.

[41] Caetano, J., de Visser, C., Remes, B., de Wagter, C., and Mulder, M., "Modeling a Flapping Wing MAV: Flight Path Reconstruction of the Delfly II," *AIAA Modeling and Simulation Technologies (MST) Conference, Boston, MA.*, 2013.

[42] Armanini, S., Karásek, M., de Visser, C., de Croon, G., and Mulder, M., "Flight testing and preliminary analysis for global system identification of ornithopter dynamics using on-board and off-board data," *AIAA Atmospheric Flight Mechanics Conference*, Grapevine, Texas, January 2017.

[43] Caetano, J., de Visser, C., Remes, B., de Wagter, C., van Kampen, E.-J., and Mulder, M., "Controlled Flight Maneuvers of a Flapping Wing Micro Air Vehicle: a Step Towards the Delfly II Identification," *2013 AIAA Atmospheric Flight Mechanics Conference*, 2013.

[44] Caetano, J., *Model Identification of a Flapping Wing Micro Aerial Vehicle*, Ph.D. thesis, Delft University of Technology, 2016.

[45] Hocking, R., "A Biometrics Invited Paper. The Analysis and Selection of Variables in Linear Regression," *Biometrics*, Vol. 32, No. 1, March 1976, pp. 1–49.

Part III

Additional material

Introduction

These appendices serve as a reference for anyone interested in continuing the work done in this thesis. It includes time response and modelling results for all configurations, for completeness, as well as the results of some supporting experiments that were conducted. Appendix B shows the time responses for all configurations, with overlays of all the manoeuvres that were conducted during an experiment and the computed average response. Appendix C shows the model eigenvalues for all configurations, which can give an indication of the level of confidence that can be put into the models of a particular configuration. Appendix D builds on this by providing the estimated model parameters and their standard deviations for all configurations. Appendix E shows the wind tunnel force balance results for all the configurations that were tested.

Appendix F shows some supporting experiments indicating that changing the leading edge shape from elliptical to straight does not have a significant effect on the results presented in this thesis. Appendix G presents the results of experiments which show that the effect of changing the tail geometry is more significant than the effects of varying flight conditions between configurations. Finally, Appendix H shows results which prove that CG shifts caused by changing the tail surface area do not influence the dynamic behaviour as significantly as changes in the tail geometry. These supporting experiments suggest that the differences in dynamic behaviour observed in the main scientific paper of this thesis can all be attributed to changes in the tail geometry and are not caused by any side effects.

Appendix B

Time response overlays

This appendix shows an overview of the manoeuvre overlays for all configurations and the measured average responses, for reference.

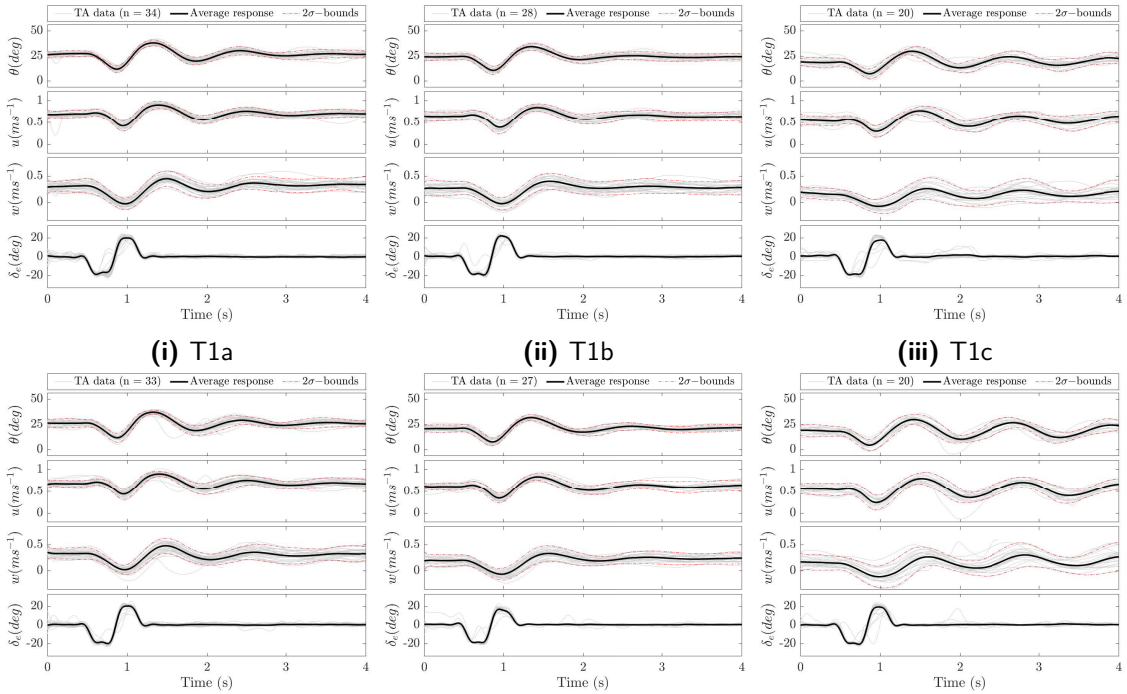

(i) T1a **(ii)** T1b **(iii)** T1c

(iv) T2a **(v)** T2b **(vi)** T2c

Figure B-1: Overlays of time responses for all manoeuvres in an experiment.

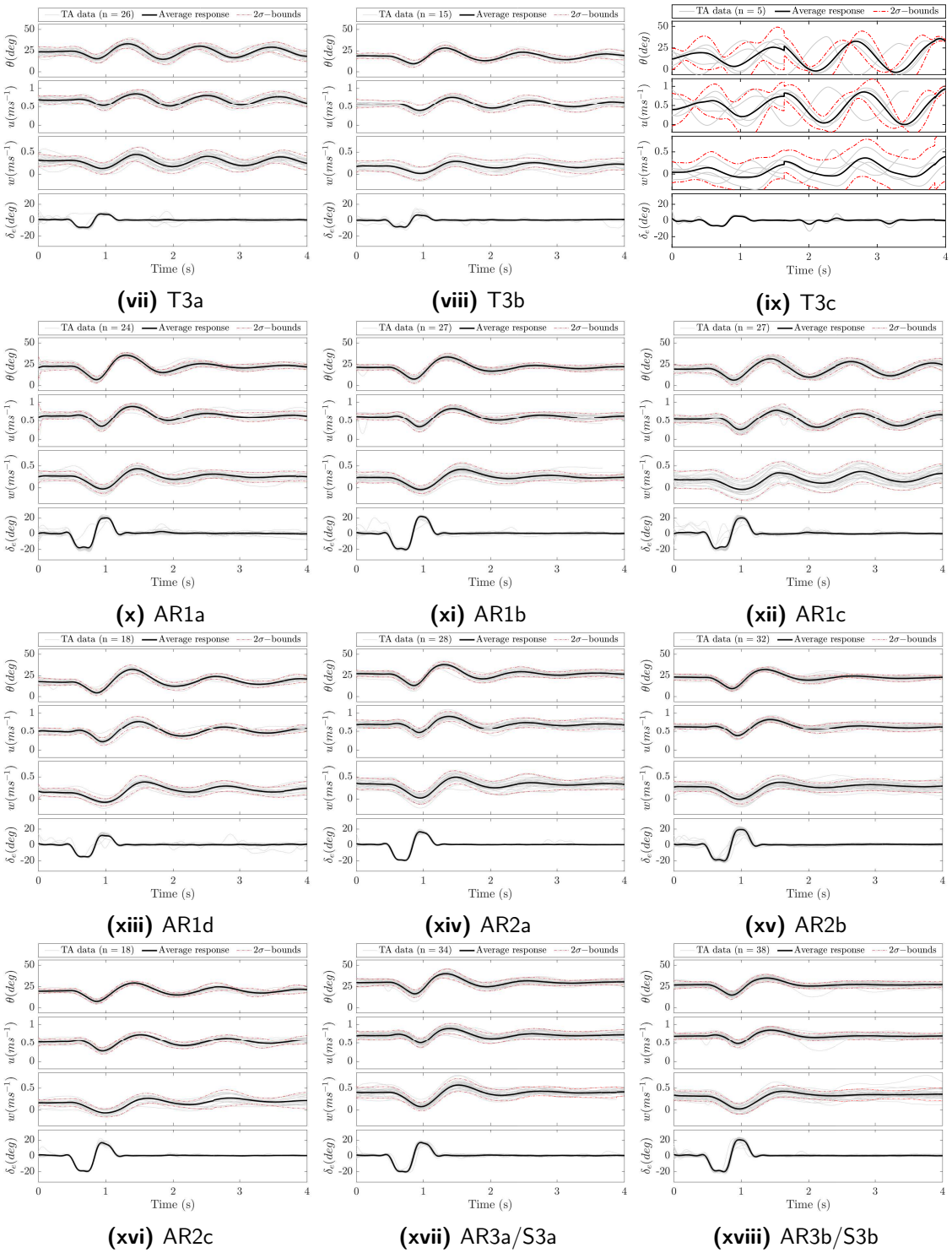

Figure B-1 (cont.): Overlays of time responses for all manoeuvres in an experiment.

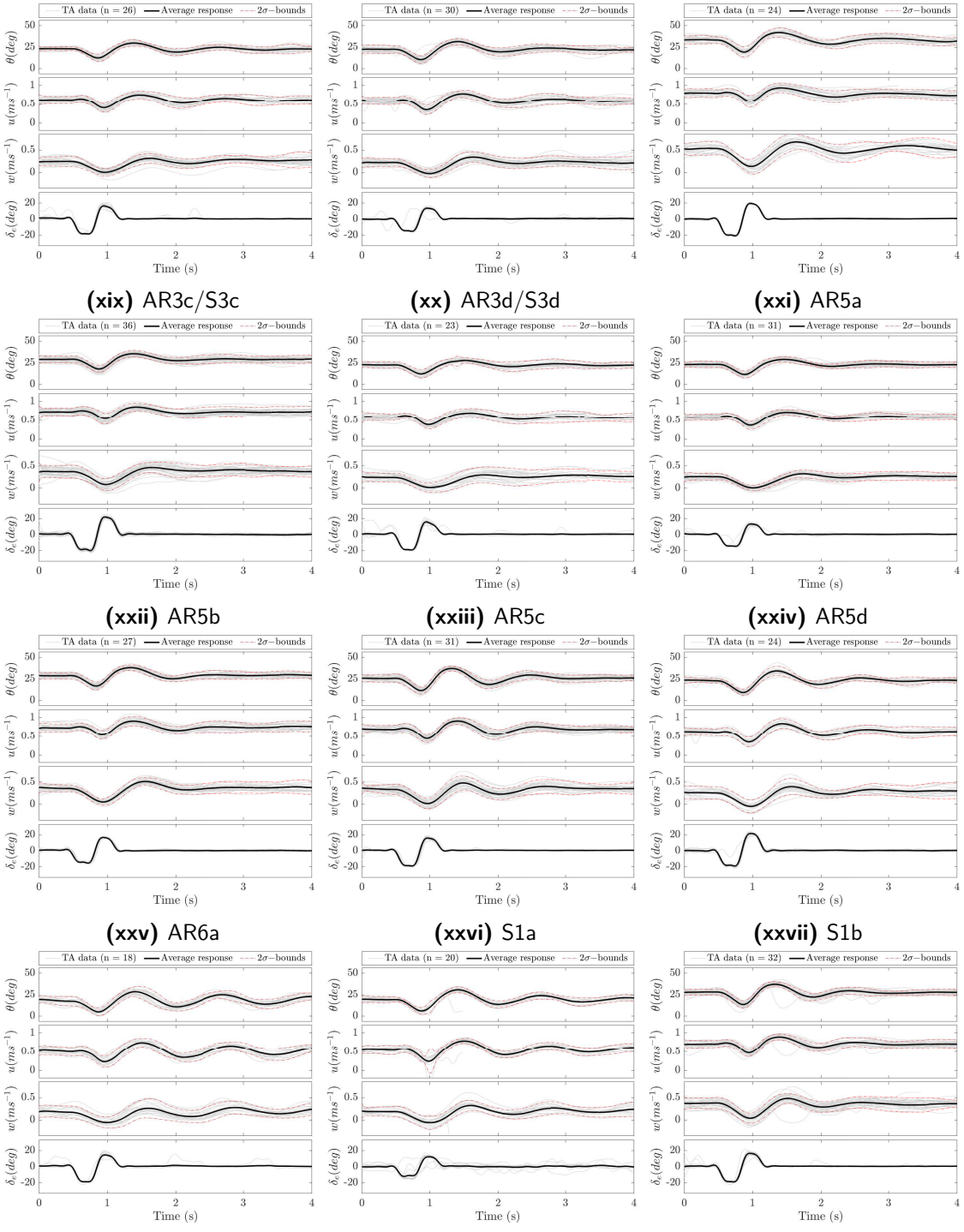

(xix) AR3c/S3c **(xx)** AR3d/S3d **(xxi)** AR5a

(xxii) AR5b **(xxiii)** AR5c **(xxiv)** AR5d

(xxv) AR6a **(xxvi)** S1a **(xxvii)** S1b

(xxviii) S1c **(xxix)** S1d **(xxx)** S2a

Figure B-1 (cont.): Overlays of time responses for all manoeuvres in an experiment.

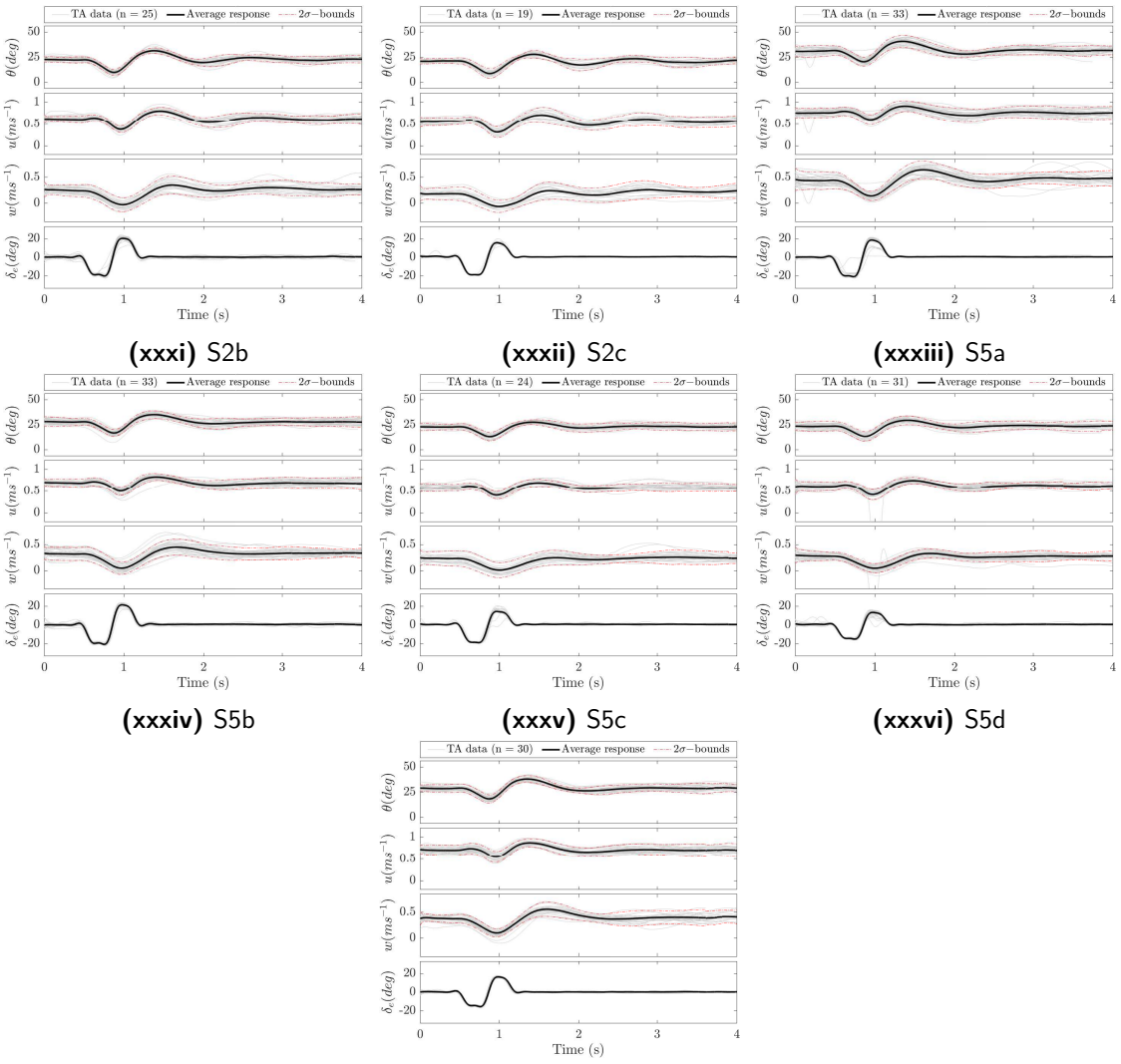

(xxxi) S2b

(xxxii) S2c

(xxxiii) S5a

(xxxiv) S5b

(xxxv) S5c

(xxxvi) S5d

(xxxvii) S6a

Figure B-1 (cont.): Overlays of time responses for all manoeuvres in an experiment.

Appendix C

Model eigenvalues

Figure C-1 offers pole plots of the model eigenvalues for all configurations. This can be used as an indication of the measure of confidence that can be put into the models for a particular configuration.

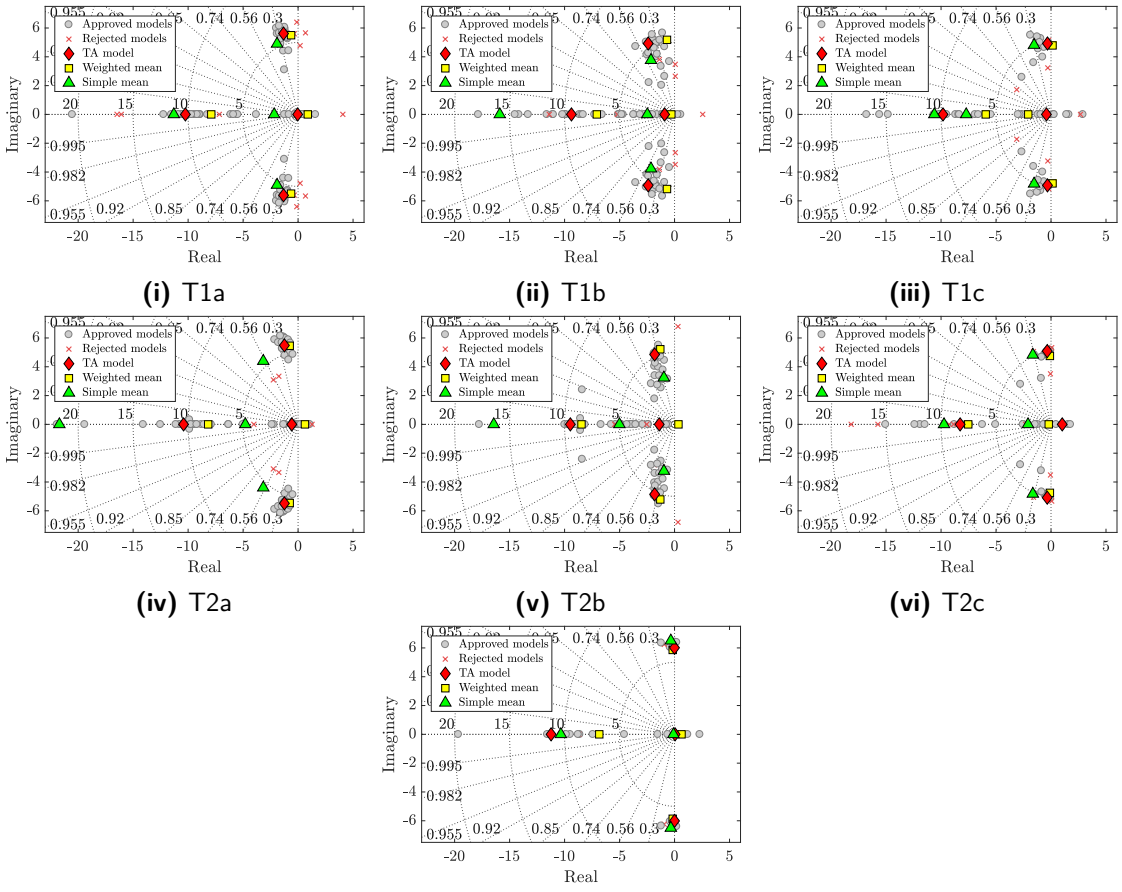

(i) T1a **(ii)** T1b **(iii)** T1c

(iv) T2a **(v)** T2b **(vi)** T2c

(vii) T3a

Figure C-1: Model eigenvalues for all individual models and estimated averaged models.

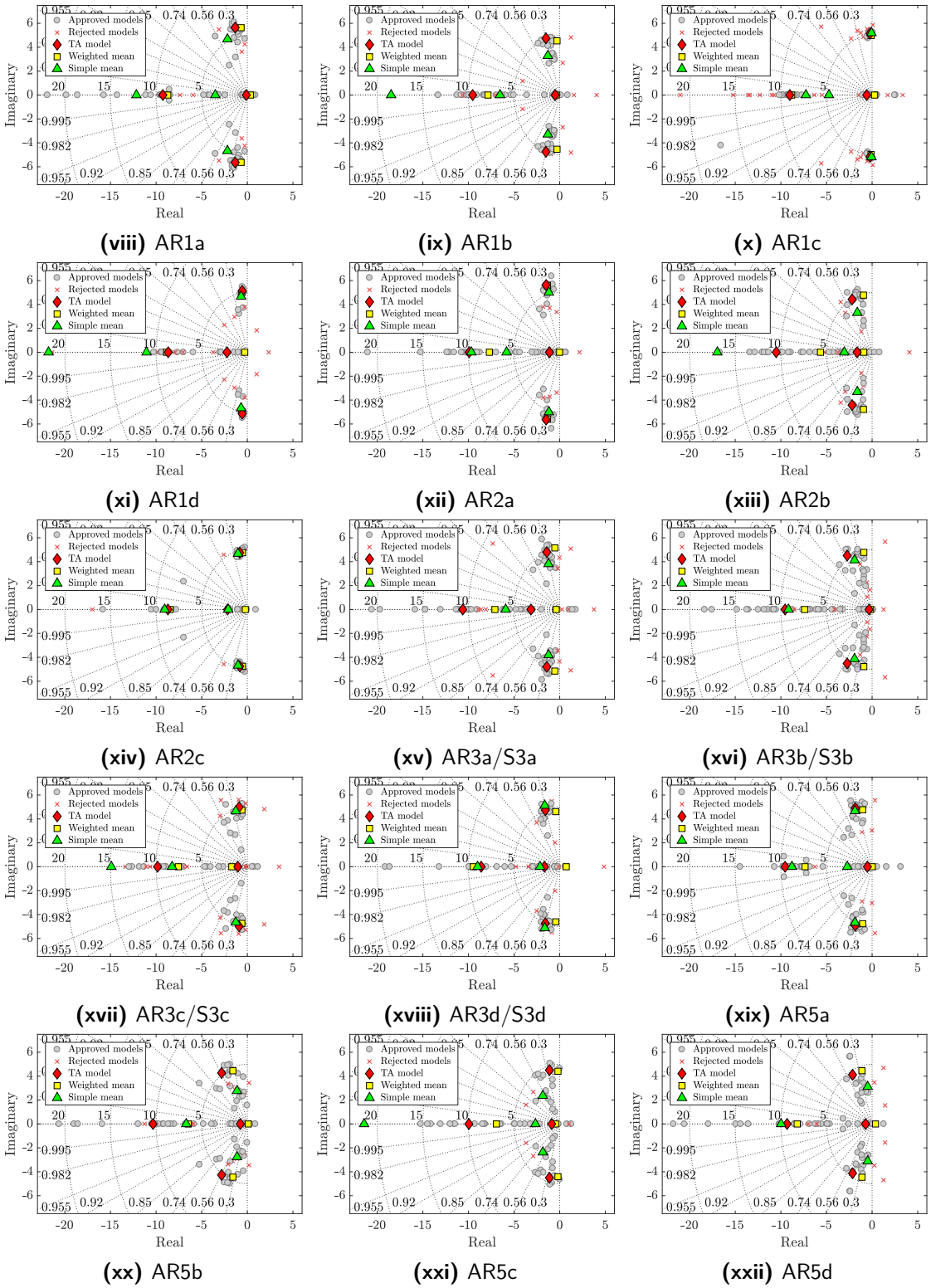

(viii) AR1a **(ix)** AR1b **(x)** AR1c

(xi) AR1d **(xii)** AR2a **(xiii)** AR2b

(xiv) AR2c **(xv)** AR3a/S3a **(xvi)** AR3b/S3b

(xvii) AR3c/S3c **(xviii)** AR3d/S3d **(xix)** AR5a

(xx) AR5b **(xxi)** AR5c **(xxii)** AR5d

Figure C-1 (cont.): Model eigenvalues for all individual models and estimated averaged models.

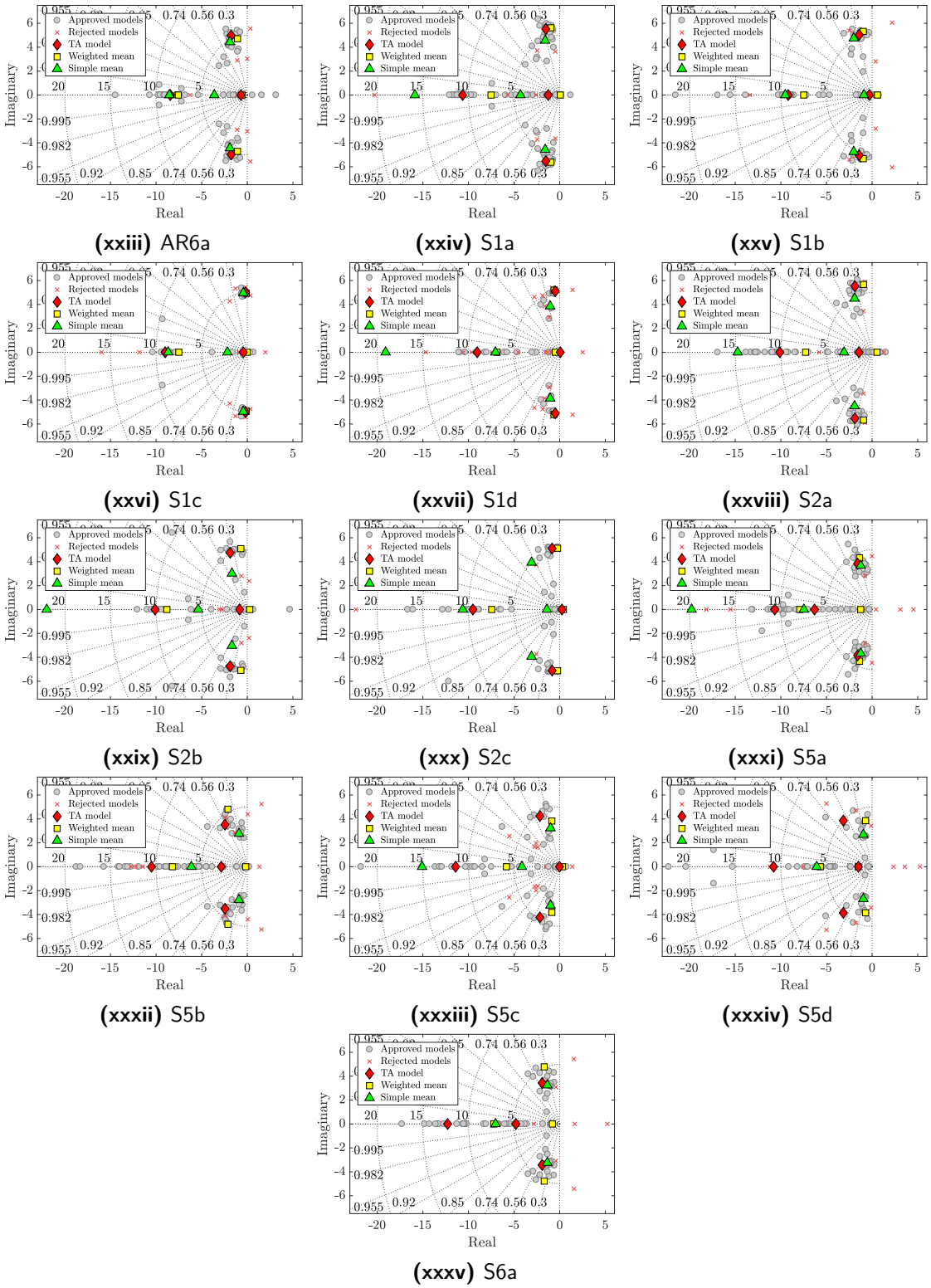

(xxiii) AR6a **(xxiv)** S1a **(xxv)** S1b

(xxvi) S1c **(xxvii)** S1d **(xxviii)** S2a

(xxix) S2b **(xxx)** S2c **(xxxi)** S5a

(xxxii) S5b **(xxxiii)** S5c **(xxxiv)** S5d

(xxxv) S6a

Figure C-1 (cont.): Model eigenvalues for all individual models and estimated averaged models.

Appendix D

Model parameters

Table D-1 and Table D-2 give a complete overview of the stability and control derivatives estimated for all configurations. Estimated standard deviations normalised by the parameter values are also given, which gives an indication on how well a particular parameter is estimated.

Table D-1: Parameter estimates ($\hat{\theta}$) and estimated standard deviations ($\hat{\sigma}$) as a function of S.

	S1a		S2a		S3a		S5a		S6a	
	$\hat{\theta}$	$100\lvert\hat{\sigma}/\hat{\theta}\rvert$	$\hat{\theta}$	$100\lvert\hat{\sigma}/\hat{\theta}\rvert$	$\hat{\theta}$	$100\lvert\hat{\sigma}/\hat{\theta}\rvert$	$\hat{\theta}$	$100\lvert\hat{\sigma}/\hat{\theta}\rvert$	$\hat{\theta}$	$100\lvert\hat{\sigma}/\hat{\theta}\rvert$
M_q	-4.35e-04	0.38	-4.28e-04	0.57	-5.02e-04	0.43	-5.65e-04	0.43	-7.45e-04	0.55
M_u	-1.39e-03	0.76	-1.61e-03	0.89	-9.02e-04	0.80	-9.61e-04	0.94	-1.32e-03	0.87
M_w	-9.25e-04	1.22	-6.38e-04	2.36	-1.32e-03	0.68	-1.07e-03	0.65	-1.25e-03	0.79
M_{δ_e}	1.52e-03	0.43	1.43e-03	0.70	1.61e-03	0.53	1.57e-03	0.45	2.41e-03	0.66
X_q	1.93e-02	0.62	2.40e-02	0.81	2.13e-02	0.67	3.06e-02	0.67	2.96e-02	1.00
X_u	-1.16e-01	0.45	-1.31e-01	0.64	-1.34e-01	0.44	-1.85e-01	0.37	-1.64e-01	0.49
X_w	-3.11e-02	1.68	-1.26e-02	6.16	-2.65e-02	2.47	-1.51e-02	3.49	-2.73e-02	2.31
X_{δ_e}	-5.94e-02	0.83	-5.60e-02	1.35	-4.52e-02	1.13	-7.74e-02	0.81	-9.35e-02	1.10
Z_q	2.84e-04	75.97	1.69e-04	146.48	5.09e-04	35.54	-3.03e-03	11.66	-1.92e-03	12.75
Z_u	1.30e-02	5.65	1.57e-02	5.95	8.59e-03	7.87	2.95e-02	2.67	2.06e-02	3.13
Z_w	-6.88e-03	8.54	-1.15e-02	6.44	-1.14e-02	5.65	-2.64e-02	2.73	-1.40e-02	3.40
Z_{δ_e}	-2.11e-03	38.40	-1.79e-03	48.83	-1.23e-02	4.66	4.15e-03	25.18	6.12e-03	12.68
	S1b		S2b		S3b		S5b		S6b	
M_q	-4.41e-04	0.48	-6.46e-04	0.57	-7.30e-04	0.49	-9.03e-04	0.54	-	-
M_u	-1.90e-03	0.45	-1.79e-03	0.64	-2.06e-03	0.67	-1.70e-03	0.66	-	-
M_w	-3.76e-05	23.30	-7.91e-04	2.05	-6.59e-04	1.56	-1.27e-03	0.82	-	-
M_{δ_e}	1.69e-03	0.47	1.81e-03	0.63	1.80e-03	0.57	2.20e-03	0.62	-	-
X_q	1.89e-02	0.77	1.85e-02	1.05	2.93e-02	0.47	3.15e-02	0.50	-	-
X_u	-1.30e-01	0.56	-1.26e-01	0.45	-1.34e-01	0.34	-1.43e-01	0.23	-	-
X_w	-1.13e-02	6.06	-4.13e-02	1.57	-2.12e-02	1.56	-3.06e-02	0.98	-	-
X_{δ_e}	-3.41e-02	1.64	-4.56e-02	1.22	-6.89e-02	0.57	-7.15e-02	0.57	-	-
Z_q	-1.26e-03	19.63	1.79e-03	24.20	1.36e-03	29.17	-2.22e-03	11.04	-	-
Z_u	1.84e-02	4.56	1.78e-02	5.96	-7.86e-04	123.50	1.58e-02	3.67	-	-
Z_w	-1.07e-02	4.16	-9.43e-03	8.10	2.05e-03	23.80	-1.79e-02	2.71	-	-
Z_{δ_e}	1.12e-02	8.01	-2.04e-02	5.87	7.13e-03	14.03	9.99e-04	60.73	-	-
	S1c		S2c		S3c		S5c		S6c	
M_q	-6.36e-04	5.32	-6.86e-04	0.72	-7.12e-04	0.64	-1.36e-03	0.52	-	-
M_u	-1.93e-03	4.80	-3.13e-03	0.55	-3.26e-03	0.55	-2.94e-03	0.65	-	-
M_w	-1.93e-03	13.28	-2.34e-04	9.13	-1.97e-04	6.62	-1.83e-03	0.92	-	-
M_{δ_e}	2.15e-03	1.16	1.84e-03	1.19	2.07e-03	0.62	2.92e-03	0.59	-	-
X_q	1.03e-02	6.02	1.25e-02	1.25	1.39e-02	1.27	1.39e-02	2.73	-	-
X_u	-1.18e-01	3.89	-1.22e-01	0.58	-1.36e-01	0.74	-1.34e-01	0.66	-	-
X_w	-3.02e-02	9.78	-1.70e-02	5.05	-1.05e-02	8.23	-4.50e-02	1.43	-	-
X_{δ_e}	-2.18e-02	5.99	-3.03e-02	2.18	-1.29e-02	3.83	-3.96e-02	2.19	-	-
Z_q	-4.08e-04	31.89	-8.88e-05	492.99	-8.84e-03	4.34	8.89e-03	6.19	-	-
Z_u	1.58e-02	13.76	2.14e-03	69.16	1.41e-02	9.97	-3.27e-03	32.01	-	-
Z_w	-2.52e-02	181.79	3.11e-03	21.46	-2.58e-02	2.86	1.26e-02	5.52	-	-
Z_{δ_e}	-8.27e-03	6.23	-1.75e-03	68.92	5.33e-02	2.00	-1.44e-02	7.92	-	-
	S1d		S2d		S3d		S5d		S6d	
M_q	-4.84e-04	0.59	-	-	-6.76e-04	0.84	-1.26e-03	0.97	-	-
M_u	-2.08e-03	0.71	-	-	-2.46e-03	0.77	-3.15e-03	1.21	-	-
M_w	-9.14e-04	3.03	-	-	-4.10e-04	5.64	-5.96e-04	6.30	-	-
M_{δ_e}	1.78e-03	0.73	-	-	2.67e-03	0.86	3.86e-03	1.13	-	-
X_q	1.32e-02	1.15	-	-	2.49e-02	1.17	3.04e-02	0.94	-	-
X_u	-1.32e-01	0.60	-	-	-1.43e-01	0.81	-1.38e-01	0.54	-	-
X_w	-8.21e-03	16.16	-	-	1.76e-02	7.29	-8.49e-03	7.88	-	-
X_{δ_e}	-3.30e-02	1.98	-	-	-5.86e-02	1.97	-9.65e-02	1.00	-	-
Z_q	2.54e-03	6.98	-	-	-1.12e-03	23.26	-3.23e-03	17.73	-	-
Z_u	-2.14e-03	35.36	-	-	2.12e-02	4.18	2.36e-02	5.89	-	-
Z_w	1.85e-02	5.07	-	-	-1.74e-02	5.14	-2.46e-02	4.52	-	-
Z_{δ_e}	-8.68e-03	7.93	-	-	-2.03e-03	48.36	-1.27e-03	143.48	-	-

Table D-2: Parameter estimates($\hat{\theta}$) and estimated standard deviations ($\hat{\sigma}$) as a function of AR.

	AR1a		AR2a		AR3a		AR5a		AR6a	
	$\hat{\theta}$	$100\lvert\hat{\sigma}/\hat{\theta}\rvert$	$\hat{\theta}$	$100\lvert\hat{\sigma}/\hat{\theta}\rvert$	$\hat{\theta}$	$100\lvert\hat{\sigma}/\hat{\theta}\rvert$	$\hat{\theta}$	$100\lvert\hat{\sigma}/\hat{\theta}\rvert$	$\hat{\theta}$	$100\lvert\hat{\sigma}/\hat{\theta}\rvert$
M_q	-3.28e-04	0.26	-4.13e-04	0.44	-5.02e-04	0.43	-3.87e-04	3.51	-4.11e-04	2.90
M_u	-1.41e-03	0.48	-1.43e-03	0.52	-9.02e-04	0.80	-1.13e-03	3.20	-9.08e-04	3.27
M_w	-4.31e-04	2.20	-7.27e-04	1.04	-1.32e-03	0.68	-5.29e-04	3.64	-7.40e-04	3.42
M_{δ_e}	1.25e-03	0.36	1.49e-03	0.49	1.61e-03	0.53	1.41e-03	1.33	1.45e-03	1.20
X_q	1.98e-02	0.47	2.09e-02	0.80	2.13e-02	0.67	2.93e-02	1.68	2.98e-02	1.70
X_u	-1.14e-01	0.35	-1.03e-01	0.72	-1.34e-01	0.44	-1.56e-01	1.58	-1.56e-01	1.57
X_w	-3.30e-02	1.20	-4.76e-02	1.40	-2.65e-02	2.47	-1.11e-02	51.29	-1.11e-02	50.39
X_{δ_e}	-5.09e-02	0.77	-4.87e-02	1.42	-4.52e-02	1.13	-8.35e-02	2.23	-8.25e-02	2.34
Z_q	1.18e-03	10.56	-1.81e-03	6.13	5.09e-04	35.54	7.02e-03	64.31	5.52e-03	65.63
Z_u	3.78e-04	127.11	2.01e-02	2.54	8.59e-03	7.87	3.67e-02	8.37	2.93e-02	17.88
Z_w	-2.08e-03	20.02	-2.10e-02	2.09	-1.14e-02	5.65	-1.76e-02	25.83	-1.60e-02	22.89
Z_{δ_e}	-7.59e-03	6.02	9.22e-03	3.80	-1.23e-02	4.66	-4.61e-02	16.43	-3.37e-02	50.62
	AR1b		AR2b		AR3b		AR5b		AR6b	
M_q	-4.52e-04	0.58	-7.78e-04	0.50	-7.30e-04	0.49	-7.88e-04	0.47	-	-
M_u	-1.86e-03	0.60	-1.86e-03	0.66	-2.06e-03	0.67	-2.00e-03	0.53	-	-
M_w	-5.52e-05	26.18	-1.10e-03	1.46	-6.59e-04	1.56	-5.93e-04	1.20	-	-
X_q	1.98e-02	0.92	2.60e-02	0.50	2.93e-02	0.47	2.72e-02	0.63	-	-
X_u	-1.58e-01	0.66	-1.28e-01	0.26	-1.34e-01	0.34	-1.38e-01	0.30	-	-
X_w	1.72e-02	7.14	-2.02e-02	2.05	-2.12e-02	1.56	-4.03e-02	0.54	-	-
X_{δ_e}	-2.86e-02	2.21	-6.38e-02	0.65	-6.89e-02	0.57	-6.22e-02	0.69	-	-
Z_q	4.50e-03	2.66	-2.28e-03	13.13	1.36e-03	29.17	-1.30e-03	19.41	-	-
Z_u	1.34e-02	4.47	1.24e-02	5.61	-7.86e-04	123.50	2.50e-02	2.96	-	-
Z_w	-2.97e-03	19.34	-1.34e-02	4.78	2.05e-03	23.80	-1.39e-02	2.50	-	-
Z_{δ_e}	-1.63e-02	2.50	1.77e-04	494.09	7.13e-03	14.03	8.73e-03	6.93	-	-
	AR1c		AR2c		AR3c		AR5c		AR6c	
M_q	-4.80e-04	0.94	-6.92e-04	0.60	-7.12e-04	0.64	-8.42e-04	0.66	-	-
M_u	-3.38e-03	0.96	-2.21e-03	1.02	-3.26e-03	0.55	-2.66e-03	0.49	-	-
M_w	5.99e-04	9.84	-1.15e-03	3.39	-1.97e-04	6.62	-4.40e-04	1.93	-	-
M_{δ_e}	1.95e-03	0.53	2.20e-03	0.61	2.07e-03	0.62	2.10e-03	0.72	-	-
X_q	5.00e-03	5.60	1.46e-02	1.25	1.39e-02	1.27	1.13e-02	1.40	-	-
X_u	-9.20e-02	2.26	-1.28e-01	0.70	-1.36e-01	0.74	-1.28e-01	0.60	-	-
X_w	-7.46e-02	5.07	-1.92e-02	7.80	-1.05e-02	8.23	-2.54e-02	2.78	-	-
X_{δ_e}	1.80e-03	29.96	-3.32e-02	1.64	-1.29e-02	3.83	-3.32e-02	1.19	-	-
Z_q	-2.89e-03	12.31	6.80e-05	420.70	-8.84e-03	4.34	-3.40e-03	8.40	-	-
Z_u	3.06e-02	5.86	2.42e-02	4.57	1.41e-02	9.97	2.66e-02	3.33	-	-
Z_w	-5.00e-02	4.68	-3.15e-02	4.95	-2.58e-02	2.86	-2.01e-02	2.62	-	-
Z_{δ_e}	-7.37e-04	219.05	-1.07e-02	8.12	5.33e-02	2.00	1.77e-02	4.12	-	-
	AR1d		AR2d		AR3d		AR5d		AR6d	
M_q	-4.54e-04	0.25	-	-	-6.76e-04	0.84	-8.44e-04	0.68	-	-
M_u	-2.16e-03	0.24	-	-	-2.46e-03	0.77	-2.08e-03	0.57	-	-
M_w	-3.99e-04	2.20	-	-	-4.10e-04	5.64	-6.63e-04	1.64	-	-
M_{δ_e}	2.10e-03	0.27	-	-	2.67e-03	0.86	2.94e-03	0.78	-	-
X_q	1.57e-02	0.36	-	-	2.49e-02	1.17	2.30e-02	0.54	-	-
X_u	-1.44e-01	0.27	-	-	-1.43e-01	0.81	-1.36e-01	0.34	-	-
X_w	1.15e-02	4.83	-	-	1.76e-02	7.29	-3.03e-02	1.49	-	-
X_{δ_e}	-2.10e-02	1.47	-	-	-5.86e-02	1.97	-7.41e-02	0.66	-	-
Z_q	6.14e-03	0.48	-	-	-1.12e-03	23.26	6.43e-05	295.69	-	-
Z_u	1.39e-02	1.41	-	-	2.12e-02	4.18	9.58e-03	6.27	-	-
Z_w	6.83e-03	4.05	-	-	-1.74e-02	5.14	-1.02e-02	4.31	-	-
Z_{δ_e}	-2.94e-02	0.67	-	-	-2.03e-03	48.36	3.52e-03	17.57	-	-

Appendix E

Wind tunnel results

The results for all wind tunnel experiments are shown in this appendix. Force balance measurements for steady-state conditions with and without tail are given, as a function of tail geometry, in Figure E-1. It is difficult to determine clear trends in these figures. Therefore, estimating the force generated by the tail as a function of its geometry was not possible at the moment.

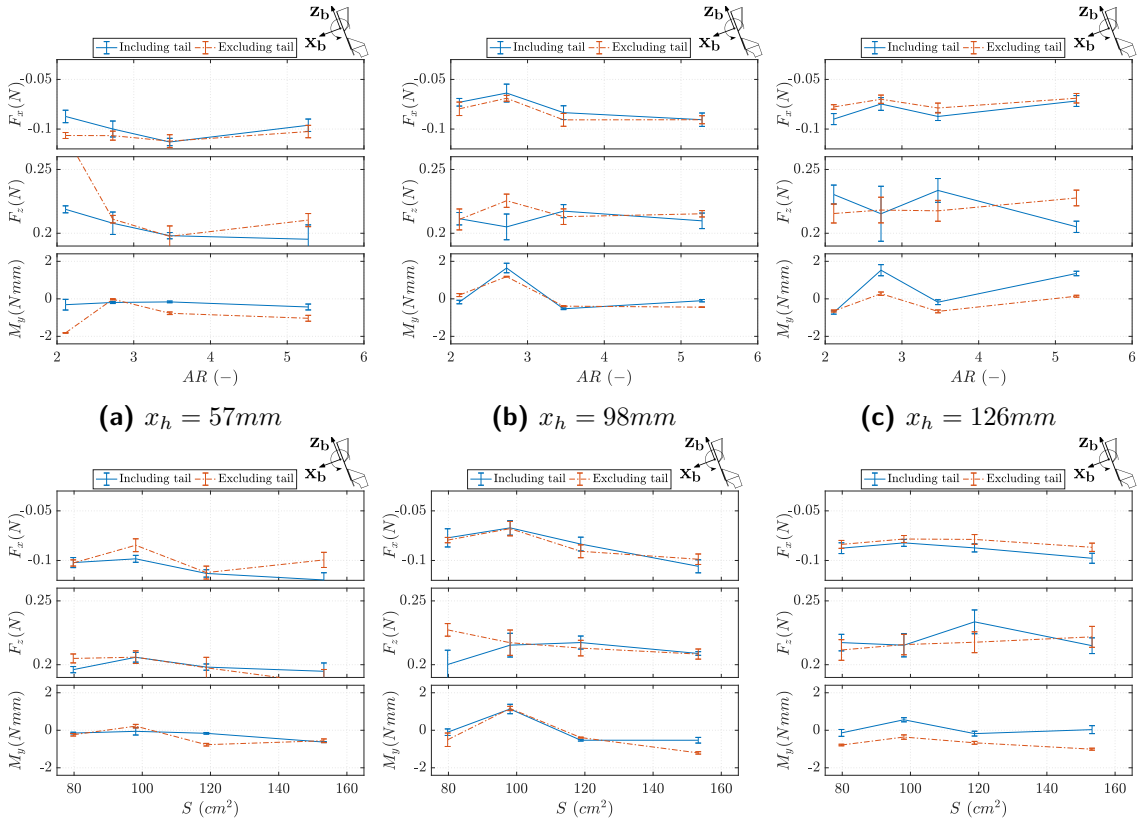

(a) $x_h = 57mm$ **(b)** $x_h = 98mm$ **(c)** $x_h = 126mm$

(d) $x_h = 57mm$ **(e)** $x_h = 98mm$ **(f)** $x_h = 126mm$

Figure E-1: Force balance results as a function of tail geometry.

Appendix F

Effect of leading edge shape

The standard DelFly II tail features an elliptical leading edge. As this would require multiple templates to cut out ellipses with different radii, the decision was made to switch to straight leading edges for this study. An additional tail configuration, T1, was made to study the effect of this change in geometrical shape on the dynamic behaviour of the platform. Configuration T1 has the same aspect ratio and surface area as the standard DelFly tail, T2.

Figure F-1 shows the average time response results for three different fuselage lengths. It is quite clear that the responses are practically identical, confirming that it is valid to change the shape of the leading edge for easier production of multiple tail configurations. For $x_h = 126mm$ some differences are seen, but this is most likely caused by less consistent experiments, see the overlays in Appendix B.

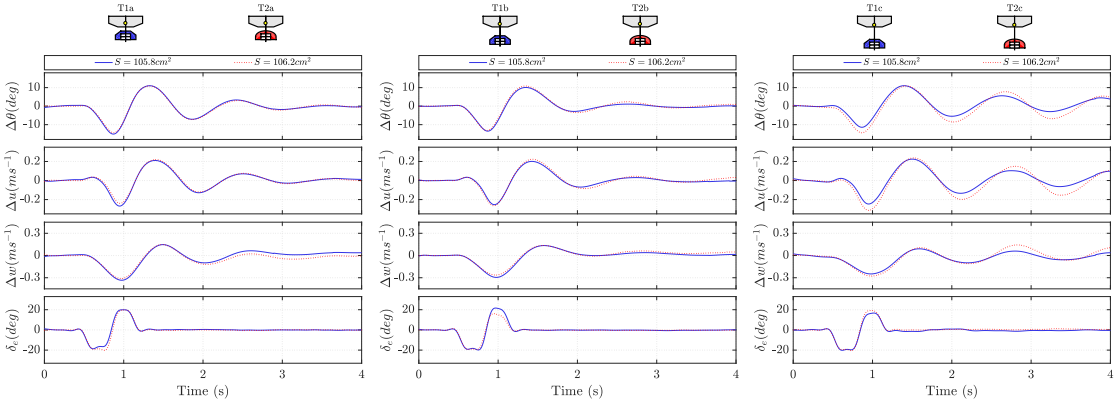

(a) $x_h = 57mm$ **(b)** $x_h = 98mm$ **(c)** $x_h = 126mm$

Figure F-1: Results of changing the leading edge shape on average time response.

Appendix G

Effect of flight conditions

Experiments were conducted to confirm that the dynamic response actually differs because of a change in tail geometry instead of due to the changes in steady-state flight condition. To study this, two configurations were trimmed to a different flight condition using the elevator. Configurations AR1a and AR5a were chosen for this, since these configurations showed a particularly large difference in flight condition.

Table G-1 gives an overview of the flight conditions and the results of trimming. Configuration AR5a was trimmed to match the flight condition of configuration AR1a. Then, AR1a was trimmed to match the flight condition of AR2a. Figure G-1 shows the time response results. Figure G-1a in particular shows very clearly that the difference in average response between AR1a and AR5a remains the same even when AR5a is trimmed to a different flight condition. Also, the response of configuration AR5a is very similar in both flight conditions. To lesser extent, due to a smaller difference in the tail geometries, Figure G-1b shows the same result.

Table G-1: Steady-state conditions for the configurations used to test the influence of flight condition. AR1a has been trimmed to match AR2a, AR5a has been trimmed to match AR1a. Values in brackets represent the measured standard deviation.

Conf.	$\theta_0(deg)$		$V_0(ms^{-1})$		$\delta_{f,0}(Hz)$		$\delta_{e,0}(deg)$		Trim value
AR1a	22.36	(2.13)	0.70	(0.06)	13.36	(0.19)	5.26	(2.03)	0%
AR1a	25.65	(1.40)	0.77	(0.04)	13.40	(0.28)	-21.49	(4.16)	+20%
AR2a	26.50	(2.08)	0.79	(0.06)	12.83	(0.29)	-6.32	(1.35)	0%
AR5a	33.55	(2.30)	0.96	(0.05)	12.35	(0.33)	-5.54	(1.25)	0%
AR5a	22.13	(2.02)	0.68	(0.05)	13.61	(0.18)	35.60	(3.44)	−15%

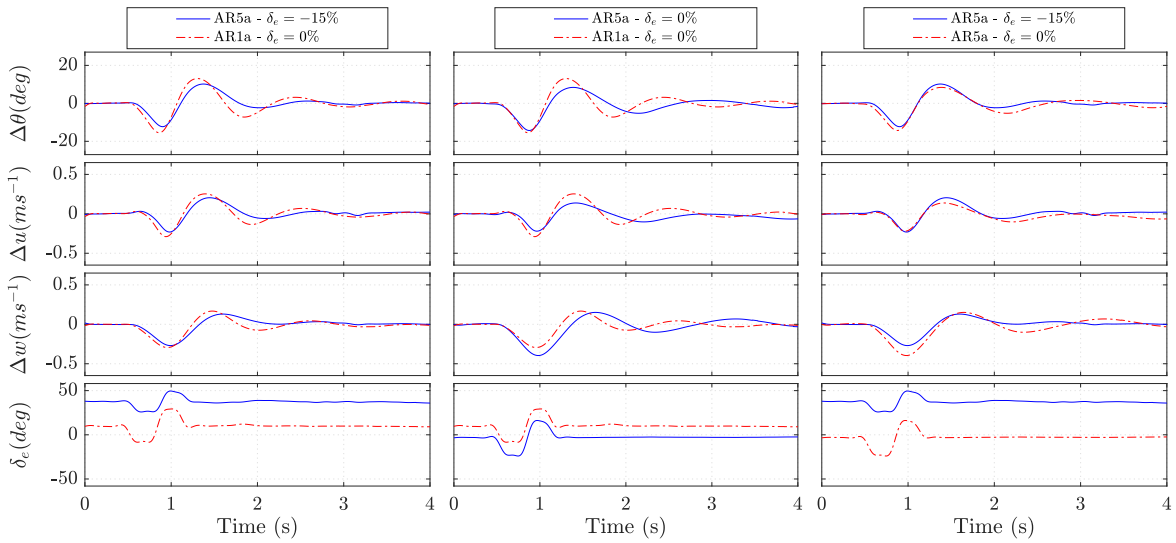

(a) AR5a trimmed to match flight condition of AR1a

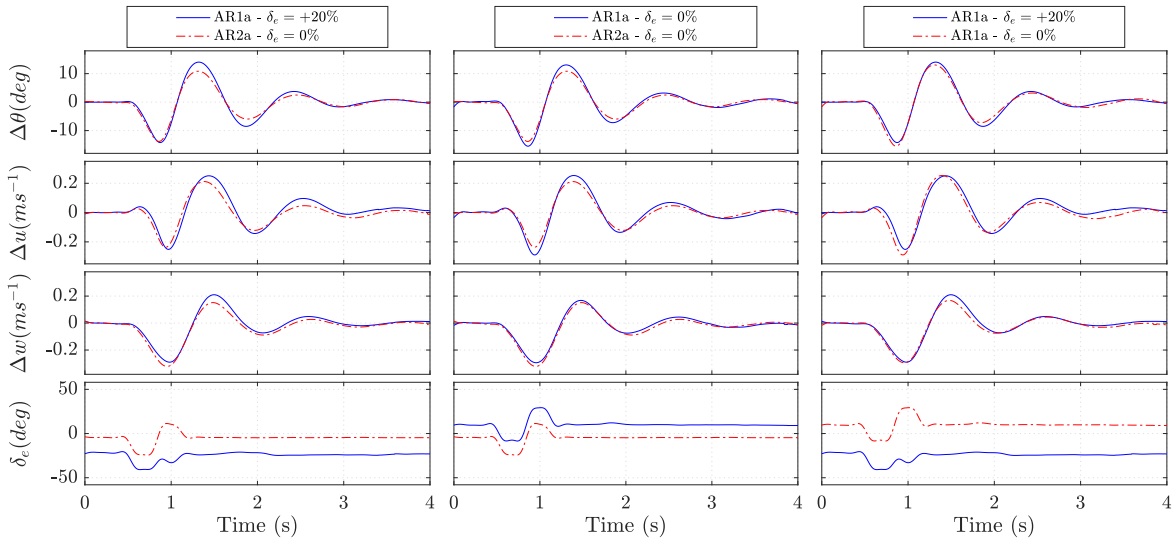

(b) AR1a trimmed to match flight condition of AR2a

Figure G-1: Average time responses for configurations when trimmed to a different flight condition.

Appendix H

Center of gravity effects

The center of gravity of the DelFly shifts due to changes in tail geometry. Especially surface area has an effect on this. The shift in center of gravity between configuration S1 and S5 is estimated to be $2.85mm$ when $x_h = 57mm$ and $4.73mm$ when $x_h = 126mm$. Such a shift in center of gravity may have some effect on the dynamic behaviour and the steady-state conditions of a particular configuration. In that case, differences observed during the experiments may actually be caused by this shift in CG instead of due to a change in tail geometry. Experiments were performed to investigate these effects, using configurations S1a and S5a. The electronics and battery assembly were moved from the most forward ($x_e \approx 42mm$) to the most aft ($x_e \approx 54mm$) positions and the system identification experiments were repeated. During all of the other system identification experiments, $x_e \approx 52mm$ was used.

Figure H-1 shows the average time responses, for different estimated longitudinal positions of the CG. The total CG shift that could be achieved by shifting the electronics is approximately $5mm$ for configuration S1a and $4.8mm$ for configuration S5a. This is in the same order of magnitude as the CG shifts that are expected due to changing between these tail configurations. The results in Figure H-1 confirm that changes in behaviour can be attributed to the change of tail geometry and are not caused by the CG shift. Though there are slight differences in steady-state conditions, these are actually insignificant in light of the measurement accuracy that can be achieved. The dynamic responses are highly similar for all three CG positions.

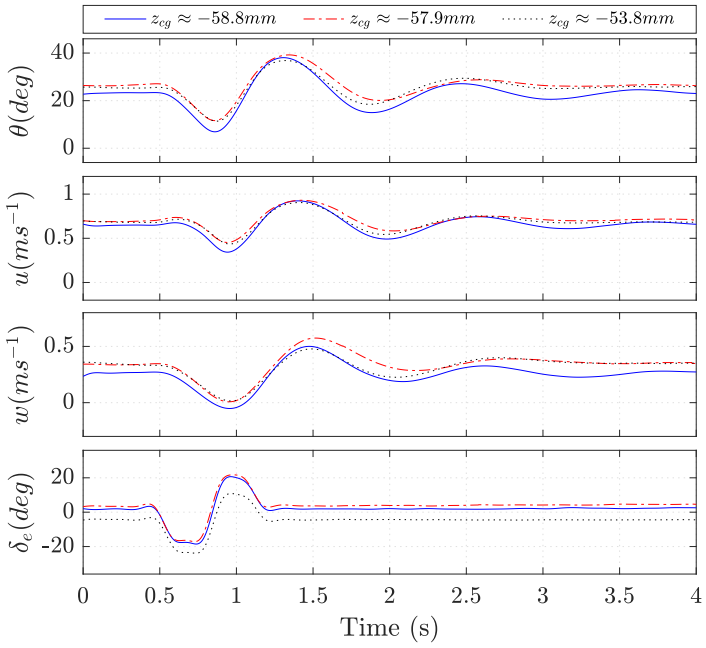

(a) Configuration S1a

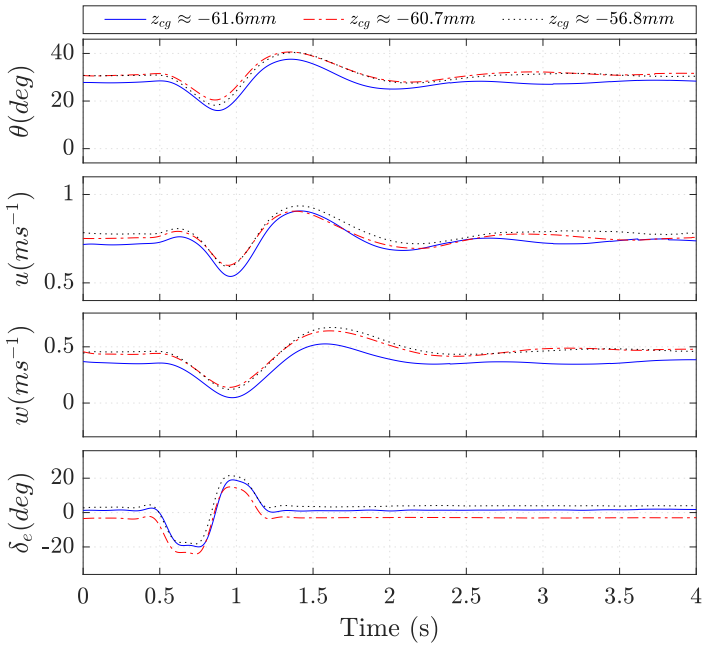

(b) Configuration S5a

Figure H-1: Results of shifting the electronics to investigate the effect of changing the CG position on the average time response and steady-state conditions. $x_e \approx 54, 52, 42mm$ respectively.